A High Resolution Measurement of Temperature Anisotropies in the Cosmic Microwave Background Radiation with the Complete ACBAR Data Set

Thesis by

Christian L Reichardt
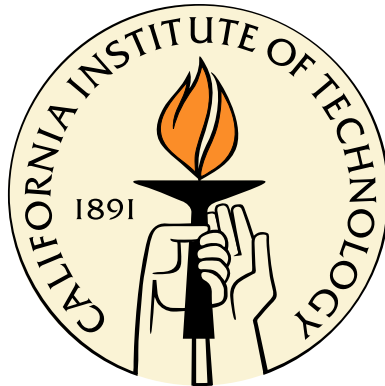
California Institute of Technology

Pasadena, California

2008

(Defended December 19, 2007)

ii

Acknowledgments

I am grateful to Andrew Lange for maintaining a great environment for doing research. Kathy Deniston held the real world at bay with her unflagging organizational support. Getting the power spectrum out would have been a hundred times more difficult with out the ofttimes daily discussions with Chao-lin Kuo. His insightful advice into problems and solutions was invaluable as the analysis progressed.

I am particularly indebted to everyone outside the ACBAR collaboration who contributed to making it a success. The Boomerang's collaboration (and especially Brendan Crill, Bill Jones and Tom Montroy) were outstanding with their willingness to not only share their data but help debug the pipelines. Julian Borrill was always helpful and able to get us more time on the irreplaceable NERSC clusters. Thanks to everyone in the grad office (Bill Jones, Ki Won Yoon, Cynthia Chiang, Ian Sullivan, Justus Brevik and Cynthia Hunt) for making it fun place to work and passing on the wisdom of the ages. Without this wealth of practical knowledge about bolometers and cryogenics, the new focal plane may have never seen first light.

I can't even begin to properly thank Yvette for her support and patience during the long years of grad school.

Thank you to everyone who read this thesis and returned valuable comments to improve it. In particular, Cynthia Chiang proof-read more than any sane person. I was fortunate to receive support from a NSF Graduate Research Fellowship for much of my grad school career.

The ACBAR Collaboration

California Institute of Technology J.A. Brevik, C.L. Kuo, A.E. Lange, C.L. Reichardt, M.C. Runyan

Carnegie Mellon University J.B. Peterson

Case Western Reserve University J.H. Goldstein, J. Ruhl

Jet Propulsion Laboratory J.J. Bock

University of California, Berkeley M.D. Daub, W.L. Holzapfel, M. Lueker

University of Sussex A.N. Romer, L.E. Valkonen

Canadian Institute of Theoretical Astrophysics J.R. Bond, C.R. Contaldi

Cardiff University P.A.R. Ade

Yerkes Observatory M. Newcomb

Joint Astronomy Centre, Hilo HI J.T. Dempsey

Abstract

The Arcminute Cosmology Bolometer Array Receiver (ACBAR) is a 16-element spiderweb bolometer array operating at 150 GHz. Mounted on the 2.1m Viper telescope, ACBAR has dedicated four years to cosmic microwave background (CMB) observations at the South Pole. We describe the focal plane reconstruction and performance of ACBAR for the 2005 austral winter. We present a new CMB temperature anisotropy power spectrum for the complete ACBAR data set. The addition of data from the 2005 observing season expands the data set by 210% and the sky coverage by 490% over the previous ACBAR releases. The expanded data set allows us to derive a new set of band-power measurements with finer ℓ-resolution and dramatically smaller uncertainties. In particular, the band-power uncertainties have been reduced by more than a factor of two on angular scales encompassing the third and fourth acoustic peaks and the damping tail of the CMB power spectrum. The calibration has been significantly improved from 6% to 2.2% in temperature by using a direct comparison between CMB anisotropy maps measured by WMAP3 and ACBAR to transfer the WMAP dipole-based calibration to ACBAR. The resulting power spectrum is consistent with theoretical predications for a spatially flat, dark energy-dominated ΛCDM cosmology.

Contents

List of Figures

List of Tables

Chapter 1

Introduction

Cosmology addresses the ultimate "Where did that come from?" questions. Our knowledge and beliefs about the origins of the universe can shape our views of the world and our place within it. The 20th century has seen a tremendous transformation in the concordance model of cosmology from a static universe to an evolving, expanding universe that 'began' a finite number of years in the past. Current experimental and theoretical studies in cosmology seek to answer questions such as "What is the universe made of?," "What drives its dynamics?," and "How did structure, the stars and galaxies we see, form?"

This chapter is devoted to a short review of cosmology, with particular emphasis on the cosmic microwave background (CMB) temperature anisotropies that are the main focus of this thesis. In Chapter 2, the Arcminute Cosmology Bolometer Array Receiver (ACBAR) experiment is described. The observations and performance of the receiver are discussed in Chapter 3. The analysis is described in detail in Chapter 4. The ACBAR CMB temperature anisotropy power spectrum and its cosmological implications can be found in Chapter 5, while a summary of other science results from ACBAR is laid out in Chapter 6.

1.1 Expanding Universe

Current cosmological models are founded on the Cosmological Principle, which states that the universe is spatially isotropic and homogenous in all its properties to all

observers. This is a natural continuance of the Copernican Principle, which divested the Earth of a special place in the universe. Earlier this century, it was common to uphold the stronger Perfect Cosmological Principle, which adds that there are no special times either. The universe is in a steady-state. In the course of the twentieth century, cosmology underwent a sea change from favoring static to expanding models. In 1929, Hubble published the first observational evidence for an expanding universe, a set of galaxy redshift observations showing a trend for galaxy redshifts to increase with distance in every direction. The further a galaxy is from us, the faster it is moving away from us. A host of observations since then have strengthened the arguments that the universe is growing larger. Steady-state theories have great difficulty explaining the evidence for an expanding universe. We now set forth a basic foundation to describe a non-static universe. This section closely follows the review work by Sanders [67].

The Cosmological Principle is a powerfully simplifying assumption, and the Robertson-Walker metric is the only metric in General Relativity consistent with it.

$$ds^2 = c^2 dt^2 - \frac{a^2(t)dt^2}{[1 - kr^2]} - a^2(t)r^2(d\theta^2 + sin^2(\theta)d\phi^2), \tag{1.1}$$

where r is the radial comoving distance, $a(t)$ is the dimensionless scale factor, and k describes the curvature of the universe. The dynamics of the universe reduce to the evolution of $a(t)$, which can be calculated from the Einstein Field equations:

$$\frac{d^2 a}{dt^2} = -\frac{4\pi G}{3}(\rho + 3p/c^2)a, \tag{1.2}$$

where ρ is the density and p is the pressure. Conservation of energy implies $d(\rho V) = -pdV/c^2$ for a perfect fluid. If the fluid's equation of state is $p = \omega\rho c^2$, then the density will evolve as $\rho \propto a^{-1(1+w))}$. Matter that we understand has $w \geq 0$: $w = 0$ for non-relativistic matter and $w = 1/3$ for photons and relativistic particles. Gravitational self-attraction will gradually slow the universe's expansion for ordinary matter; however, supernovae observations have measured an accelerating expansion. Plugging the equation of state into Eq. 1.2 indicates that a fluid will cause acceleration

if $w < -1/3$. Einstein's cosmological constant has $w = -1$, and pinning down the details of w for the dark energy making up 70% of the universe is an active area of research.

The space-space components combined with the time-time component yield the first-order Friedmann equation:

$$\left(\frac{H}{H_0}\right)^2 - \Omega_k a^{-2} = \sum_i \Omega_i a^{-3(1+w_i)},$$

where $H = \dot{a}/a$ is the Hubble parameter and $\Omega_i = \frac{8\pi G \rho_i}{3H_0^2}$ for the various fluids in the universe. Redshift is often used instead of the scale factor with $a = (1+z)^{-1}$. For a universe composed of non-relativistic matter, radiation, and some sort of dark energy, the Friedmann equation takes the familiar form:

$$\left(\frac{H}{H_0}\right)^2 = \Omega_r a^{-4} + \Omega_m a^{-3} + \Omega_k a^{-2} + \Omega_{DE} a^{-1(1+w)}. \tag{1.3}$$

Each component scales differently with the size of the universe, causing the universe to be dominated by radiation at early times ($a << 1$), become matter-dominated at intermediate times, and potentially expand to scales where dark energy determines the universe's dynamics. For the Einstein's cosmological constant, which has $w = -1$, the last term reduces from $\Omega_{DE} a^{-1(1+w)}$ to Ω_Λ.

Distances on cosmological scales must be clearly defined based on the behavior we expect. The comoving distance between two objects is a distance scale which will remain unchanged as the universe expands. This distance can be calculated by integrating Eq. 1.3 ([31]):

$$D_C = \frac{c}{H_0} \int_0^z \frac{dz'}{(\Omega_r(1+z)^4 + \Omega_m(1+z)^3 + \Omega_k(1+z)^2 + \Omega_\Lambda)^{\frac{1}{2}}}.$$

The angular diameter distance is defined as

$$D_A = \frac{d}{\theta}$$

for an object of size d which subtends the observed angle θ. This is a different distance scale than the luminousity distance defined by

$$D_L = \left(\frac{L}{4\pi F} \right)^{\frac{1}{2}},$$

where L is the luminousity and F is the measured flux. For a flat universe ($\Omega_k = 0$), the angular diameter distance and luminousity distance are related to the comoving distance by:

$$D_A = D_C/(1+z)$$

$$D_L = D_C * (1+z).$$

The angular diameter distance will play a key role in extracting cosmological information from the angular size of the observed CMB anisotropies. All distance scales depend on the expansion history and curvature of the universe and can be used for cosmological tests.

1.2 The Cosmic Microwave Background

1.2.1 Recombination and the Surface of Last Scattering

The cosmic microwave background radiation (CMB) was first predicted by Gamow in 1948 as a natural consequence of the Big Bang theory. The CMB is an afterglow of the hot, early universe. The radiation was unintentionally discovered by Penzias and Wilson in 1965, an achievement which garnered the Nobel prize in 1978. Twenty-seven years and many experiments later, the first anisotropies in the CMB were detected by COBE at the tiny level of one part in 100,000. A second instrument on the same satellite, FIRAS, established that the CMB has a practically perfect blackbody spectrum. Since then, dozens of experiments have made increasingly sensitive measurements of the CMB temperature anisotropies.

Given the high temperatures and densities of the early universe, a wide variety of particles will undergo multiple interactions in the time it takes the universe to double

in size and remain in thermodynamic equilibrium. The rapid reaction rate will tend to thermalize any initial particle distribution and transform it into a Planck distribution. The universe's temperature and density drop as it expands, causing the reaction rates to fall. At some point, the rate will drop to $\ll 1$ in a Hubble time, at which point that reaction has effectively frozen out. The time at which freeze-out occurs depends on the energy scale of the reaction. Nuclear reactions stop at $T \sim 1\ MeV$ since typical nuclear binding energies are on MeV scales. The ionization energy of hydrogen is 13.6 eV; therefore, we expect the free electrons to recombine with protons to form neutral hydrogen when the temperature drops below $T \lesssim 13.6\ eV$. Recombination actually occurs a little later at temperatures of $T \sim 1$ eV due to a huge over-abundance of photons ($\sim 10^9$) per hydrogen atom. As the free electron fraction drops during recombination, the universe quickly becomes optically transparent. The optical depth of the universe to that transition is much less than unity ($\tau \approx 0.07$ [28]). The CMB photons can free-stream from the "surface of last scattering" some 300,000 years after the Big Bang to our experiment today. As a result, the CMB anisotropies observed today give a snapshot of the universe on the surface of last scattering at $z = 1100$.

Such a snapshot has two advantages for studying cosmology. First, the angular size of objects at $z = 1100$ provides a long lever arm on the geometry of the universe. Second, and slightly counter-intuitively, it is far easier to model features in the early universe than in more recent observations of stars and galaxies. Inflation predicts and observations confirm that the early universe is extremely homogenous. The CMB temperature anisotropies are a tiny fraction of the mean background: $\delta T/T \simeq 10^{-5}$. As a result, the early universe can be analyzed in the linear regime without the messy complications of non-linear physics.

1.2.2 Evolution of Perturbations and the Boltzmann Equations

The Boltzmann equations for photons, baryons, and dark matter determine the growth of the perturbations that lead to the CMB temperature anisotropies. The

Boltzmann equations prove easier to solve in the Fourier domain since in the linear approximation each wavenumber $\bar{k}$ will evolve independently. I draw upon the work of [17] to summarize the equations for the dominant components of the universe at recombination: photons, baryons, and cold dark matter. A more complete treatment can be found in most cosmology textbooks. The Boltzmann equations for photons can also be expressed to first order for scalar perturbations as

$$\dot{\tilde{T}} + ik(\hat{k} \cdot \hat{p})\tilde{T} + \dot{\tilde{\Phi}} + ik(\hat{k} \cdot \hat{p})\tilde{\Psi} = -\dot{\tau}\left[\tilde{T}_0 - \tilde{T} + (\hat{k} \cdot \hat{p})\tilde{v}_b\right]$$

where $\tilde{T}$ marks the Fourier transform of the photon temperature, $\hat{p}$ is the photon direction, τ is the optical depth, and v_b is the electron velocity. Φ and Ψ are perturbations to the metric representing curvature perturbations and Newtonian potential perturbations. Variables are marked with a $\dot{\;}$ to denote the derivative with respect to conformal times and a $\tilde{\;}$ to denote the Fourier transform. The derivative of the optical depth can be written as the product of the Thomson cross section and electron density $\dot{\tau} = -n_e \sigma_T a$.

Matter perturbations will have two free parameters, density and velocity. The Boltzmann equations for cold dark matter can be simplified to a pair of equations:

$$\dot{\tilde{\delta}} + ik\tilde{v} + 3\dot{\tilde{\Phi}} = 0$$
$$\dot{\tilde{v}} + \frac{\dot{a}}{a}\tilde{v} + ik\tilde{\Psi} = 0,$$

where δ is the fractional overdensity $\delta\rho/\rho$ and v the velocity of the dark matter. Electrons and protons will remain tightly coupled by Coulomb forces and can be analyzed together as a baryon term. The electrons will also couple to the photons with Thomson scattering. The Boltzmann equations for baryons become

$$\dot{\tilde{\delta}}_b + ik\tilde{v}_b + 3\dot{\tilde{\Phi}} = 0$$
$$\dot{\tilde{v}}_b + \frac{\dot{a}}{a}\tilde{v}_b + ik\tilde{\Psi} = \dot{\tau}\frac{4\rho_\gamma}{3\rho_b}\left[3i\tilde{T}_1 + \tilde{v}_b\right].$$

These equations can be solved numerically to great precision for a given cosmological theory by publically available Boltzmann codes such as CMBFAST[1] [70] and CAMB[2].

1.2.3   CMB Power Spectrum

Power spectra such as the one in Figure 1.1 are the favored tool to bridge the gap between theory and the observed temperature anisotropy maps. The power spectrum of a gaussian random field completely describes the distribution, making the power spectrum a natural meeting point between the observations and theoretical models. The primary CMB anisotropies are expected and observed to be a gaussian random field. Some theories predict a small non-gaussian component which may be detectable by future experiments. Constraints on cosmological parameters can be derived by comparing the experimentally measured band-powers to the predicted power spectra from Boltzmann codes for a multi-dimensional array of cosmological parameters. For historic reasons, CMB temperature anisotropy power spectrum is conventionally parametrized as:

$$D_\ell \equiv \frac{\ell(\ell+1)}{2\pi} C_\ell,$$

where $C_\ell = \frac{1}{2\ell+1} \sum_m a_{\ell m}^* a_{\ell m}$. With this variable substitution, a hypothetical power spectrum with equal amounts of power in each frequency interval would be plotted as a flat line.

1.2.4   Polarization of the CMB

ACBAR and this thesis exclusively focus on measuring the unpolarized CMB temperature anisotropies. This is not the only route to study the CMB anisotropies: the CMB is partially polarized. Quadrupole electron density anisotropies on the surface of last scattering can produce a slight excess of one linear polarization over the second. The polarization of the CMB was first detected by DASI [40] in 2002 and has

---

[1]http://cfa-www.harvard.edu/ mzaldarr/CMBFAST/cmbfast.html
[2]http://camb.info/
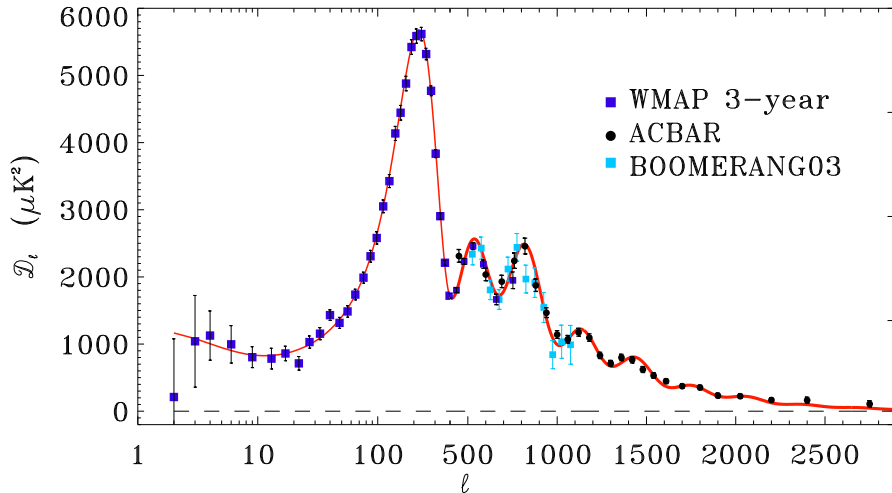
Figure 1.1: Measurements of the CMB temperature anisotropy power spectrum made with the satellite WMAP, the ballon-borne experiment B03, and the ground-based ACBAR experiment. The model line is derived from the best-fit cosmological parameters of WMAP3+ACBAR (see Ch. 5) using CAMB.

been observed since then by multiple experiments including WMAP [54], CBI [60], CAPMAP [1], Boomerang [57], and QUaD [?], . Detecting and measuring the predicted polarization power spectrum provides an independent confirmation of our understanding of the CMB. Polarization measurements can also be combined with the temperature anisotropy measurements to improve constraints on cosmological parameters.

The polarization induced by quadrupole moments can be described by a curl-free, or "E-mode," vector field. At an even lower amplitude, gravitational lensing and gravitational waves will convert a fraction of the E-mode polarization into a vector field with curl or "B-mode" field. Noteworthily, gravitational waves excited by inflation could produce a bump on the B-mode power spectrum below $\ell = 100$. Unfortunately, foregrounds are also polarized and the inflationary B-modes are sufficiently dim to be completely masked by foregrounds in some models. Many current and planned experiments are looking for the B-mode signature of inflation. Detecting the gravitational wave signature of inflation would lead to the first direct probes of inflation.

Chapter 2

The ACBAR Instrument

The Arcminute Cosmology Bolometer Array Receiver (ACBAR) is a multi-frequency millimeter-wave receiver designed to take advantage of the excellent observing conditions at the South Pole to make extremely deep maps of CMB anisotropies [65]. ACBAR is mounted on the Viper telescope, a 2.1m off-axis Gregorian with beam sizes of 5'. The beams are swept across the sky at near-constant elevation by the motion of a flat tertiary mirror.

The receiver contains 16 optically active bolometers cooled to 240 mK by a three-stage He^3-He^3-He^4 sorption refrigerator. The results reported here are derived from the 150 GHz detectors: there were 4 150-GHz bolometers in 2001, 8 in 2002 and 2004, and 16 in 2005. The detectors were background limited at 150 GHz with a sensitivity of approximately 340 $\mu K \sqrt{s}$.

2.1   Retrofitting of the Focal Plane

After the 2002 science observations, we considered focal plane upgrades to improve ACBAR's performance. The Viper telescope would be used by another experiment, SPARO, in 2003 making this a natural break-point. The initial idea was to eliminate the four underperforming 275 GHz detectors and to populate the focal plane with some combination of 150 GHz and 220 GHz detectors for the 2004 season. Three main focal plane configurations were considered: all 150 GHz, equal focal plane sensitivities at 150 GHz and 220 GHz, and all 220 GHz.

The choice was made based on modeling of three potential science objectives: a search for SZ clusters, a confirmation of the recently announced CBI excess power [5, 50, 59], and an improved measurement of the CMB TT power spectrum. The cluster model in [64] was used to predict the expected number of SZ cluster detections. ACBAR's beams are larger than would be optimal for cluster searching. Even for a fairly high $\sigma_8 = 0.9$, only $\sim$5 detectable clusters were predicted in the ACBAR maps. The small sample size made cluster searching risky with very limited cosmological significance. The predicted number of clusters detected varied by less than 40% between the all 150 GHz and mixed focal planes due to a tradeoff between deeper maps and less CMB confusion.

The expected band-power errors of each focal plane configuration were modeled using the Knox formulas [35, 75] for a number of observing strategies. An empirically derived scaling of the area and sensitivity was applied to match the published ACBAR power spectrum errors ([44]; hereafter K02). The modeling did not assume the no-LMT analysis presented in ([42]; K07), and as a result, predicted significantly worse band-power errors than have been achieved in the power spectrum presented in §5. The main advantage of a mixed focal plane would be to discriminate between the primary and SZE power spectrum. The instantaneous NET_{CMB} of the 220 GHz detectors was $640\,\mu K \sqrt{s}$, nearly twice that of the 150 GHz detectors with $NET_{CMB} = 345\,\mu K \sqrt{s}$. The focal plane would need to consist almost entirely of 220 GHz detectors to achieve equal sensitivities at each frequency, which would have steeply reduced the focal plane sensitivity. The mixed focal plane lacked the sensitivity to make a $>3\sigma$ detection of SZE power consistent with the CBI results. We settled on the 16-150 GHz configuration, as the increased sensitivity made it the clear-cut winner for measuring the primary CMB power spectrum. The hardware effort for the focal plane renovation is dicussed later in this chapter.

2.2 Detectors

ACBAR uses sensitive spiderweb bolometers to detect the minute temperature fluctuations in the CMB. Spiderweb bolometers are named for the web-like mesh designed to collect photons while minimizing the absorber mass and cross section to cosmic rays [52]. Figure 2.1 has an image of a bolometer. With less mass in the absorber, a spiderweb bolometer is less sensitive to microphonics. The low thermal mass facilitates fast thermal time constants ($\tau_{ACBAR} < 8$ ms & $\langle \tau_{ACBAR} \rangle \simeq 4$ ms). This is important due to ACBAR's scan speed. The web itself consists of a Si_3N_4 structural mesh over which a thin layer of gold is deposited. In order to maximize the optical efficiency, the mesh is positioned $\lambda/8$ above a conductive backstop, and the thickness of the gold layer is tuned to match the free-space impedance of the cavity. The temperature of the mesh will vary based on the absorbed optical power and is read out via a neutron transmutation doped (NTD) germanium thermistor. At operating temperatures, the resistance of the NTD thermistor scales exponentially with temperature ($R = R_0^{-\sqrt{\frac{\Delta}{T}}}$). These devices were developed by the Micro Devices Laboratory at the Jet Propulsion Laboratory (JPL) for the Planck Satellite. Appendix A has a brief summary of bolometer physics.

The NTD bolometers in ACBAR are quasi-current biased by virtue of being mounted in series with two 30 MΩ load resistors.[1] For comparison, the average resistance of the ACBAR bolometers at operating temperatures is 6.7 MΩ. EMI filters consisting of a 47 nH inductor[2] and a 10 pF capacitive feed-through filter[3] are positioned on each input of the bolometer to provide RF filtering directly at the bolometer. All of these components are surface-mounted to a PCB board (see Figure 2.2), which is silver epoxied[4] directly to the back of the bolometer module. The module connects to the outside electronics through a 5-pin microdot connecter[5], which is

---

[1]Mini-systems, Inc. Attleboro, MA 02703
[2]muRata part #LQP21A47NG14M00, Murata Electronics, Smyrna, GA 30080
[3]muRata part #NFM839R02C100R470T1, Murata Electronics, Smyrna, GA 30080
[4]Epo-Tek H20E, Epoxy Technology, Billerica, MA 01821
[5]Microdot Connector, South Pasadena, CA 91030
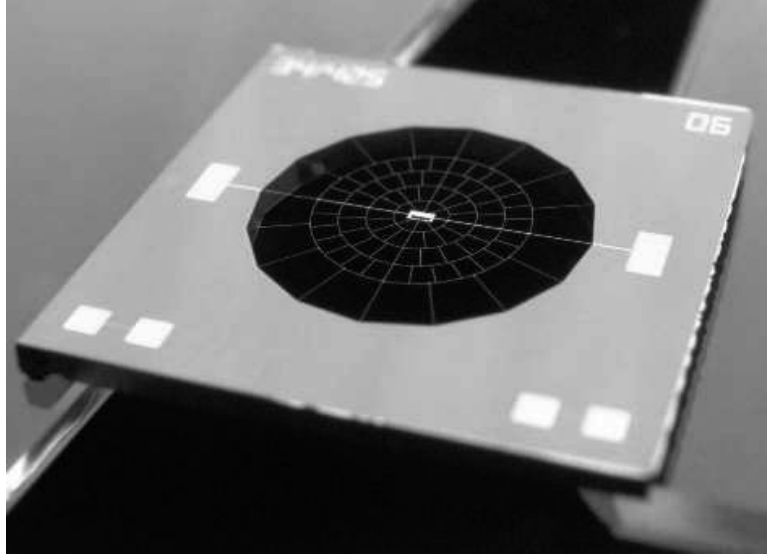
Figure 2.1: Closeup image of a spiderweb bolometer similar to the ones in ACBAR. Clearly visible is the spiderweb absorbing mesh with the NTD thermistor at the center. Photo courtesy of Jamie Bock at the Micro Devices Lab at JPL.

firmly stycasted[6] in place to avoid stressing the solder joints. Before inserting bolometers, the modules were thermal cycled multiple times and the integrity of the circuit double-checked. The bolometers are epoxied[7] in place at a single attachment point (a small "epoxy well" was included in the module design for this purpose) and connected to the feed-through capacitators (and the rest of the circuit) with fine gold wire and dabs of silver epoxy. The assembly is done manually with the aid of a microscope.

The support ring of the bolometers installed in the 2005 had a different shape than its precursors (square vs hexagon). It was an unplanned change discovered when we received the bolometers for mounting in the modules. Initially, we believed that the difference was relatively unimportant and required only a small amount of milling to expand the cavity of the bolometer module. However, several devices later cracked at the epoxy attachment point during thermal cycling. The epoxy well was positioned to be at the corner of a hexagonal device, which is the thickest portion of the support ring. With the new square devices (as in Figure 2.1), the attachment point was at the thinnest portion of the silicon support ring in the middle of one edge.

---

[6]Stycast 2850 FT, Emerson & Cuming, Billerica, MA 01821
[7]Miller-Stephenson Epoxy 907
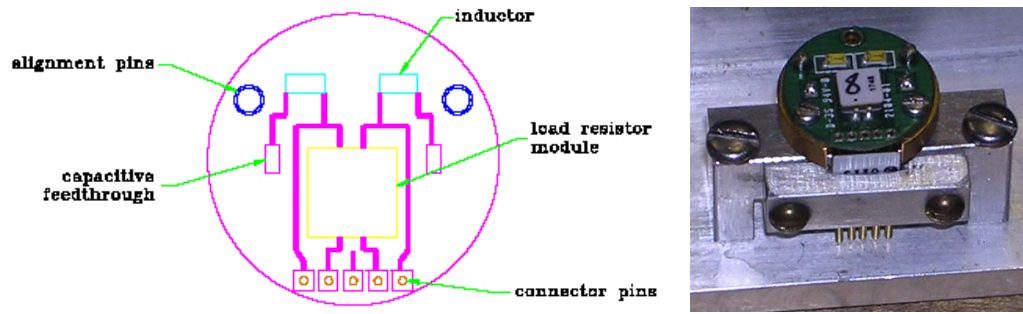
Figure 2.2: On the **left-hand side**, a schematic circuit for the bolometer module provided by R. S. Bhatia. On the **right-hand side**, a photograph of a module during assembly.

Approximately 25% of the new devices showed stress fractures at the epoxy point after multiple thermal cycles, presumably due to differential thermal contraction. No stress fractures were seen on the devices selected to be installed in the ACBAR dewar. In one device, multiple breaks in the support ring meant that the web was supporting the full weight of the bolometer. This device had abnormal noise characteristics which led to the discovery of the stress fractures. Notably, the more minor stress fractures in other devices did not worsen the bolometers' 1/f noise or microphonic response.

Each newly mounted bolometer was submitted to a battery of dark and optical tests. The testing dewar could accomodate two dark detectors blanked off at 270 mK or one optically active, "light" detector. Each dark run targeted three key pieces of information: the detector's resistance as a function of temperature R(T), the bolometer thermal conductance at zero loading G(T), and a characterization of the detector's noise and microphonic properties. Each light run yielded information on a bolometer's optical time constant, thermal model, noise, and microphonic properties. The optical runs also measured the transmission band-pass, optical efficiency, and optical loading for the combined feedhorn, filter, and detector stack. For these tests, the focal plane was temperature-controlled using a PID loop[8] linking a heater resistor to a GRT mounted near the detectors.

In order to determine R(T) for each bolometer, the resistance of the NTD ther-

---

[8]Oxford TS-530 Temperature Controller

mistor on each bolometer is measured at approximately seven temperatures. The electrical power at high bias voltages will heat the bolometer and lower its resistance, leading to a non-linear bias-to-signal relationship. Only the lowest bias points are used to measure the bolometer resistance to avoid the non-linearities at higher voltages. The data are fit to a model for these thermistors of the form $R(T_{bolo}) = R_0 e^{-\sqrt{\Delta/T_{bolo}}}$. Here, R is the measured resistance, R_0 and Δ are the model parameters, and $T_{bolo} = T_{base} + T_{offset}$ allows for a small temperature offset between the bolometer and calibrated GRT on the focal plane. The value of T_{offset} is a free parameter, and is found to be $\lesssim 5$ mK. The value of Δ is expected to be 41.8 K based on the material properties of the thermistor. The measured fits agreed well with 41.8 K, and Δ was fixed to 41.8 K to determine the parameters quoted in Table 2.1. A two-sided load curve is also taken at each temperature point and fit to a thermal model for the bolometer (see Appendix A and Table 2.1). While examined for oddities and other warning signs, the thermal properties inferred from the dark load curve measurements do not enter the CMB analysis.

The noise of each bolometer was measured in five-minute chunks at a number of different bias voltages. The noise measurements were repeated a second time while mechanically vibrating the dewar to excite microphonic lines. A dark bolometer will be more sensitive to microphonics due to its increased impedance, making this a worst case estimate. The test dewar was insufficiently stable to probe the noise over periods longer than 5 minutes. This was not a serious problem. On the telescope, the JFETs and atmospheric noise introduce a 1/f knee at 1-3 Hz which dominates the noise characteristics of the detectors at low frequencies. As with the dark load curves, the dark noise tests were primarily intended for troubleshooting. All but one of the detectors (the one with the severely cracked support ring) had clean noise PSDs. The noise tests were repeated in the light runs with the dewar window capped for a stable optical load, and no detectors were found to have excess noise.

The optical time constant of each bolometer was calculated from the measured detector response to a chopped LN_2 source. The LN_2 source was situated behind a metal sheet with a small aperture. A chopping wheel coated in Eccosorb was

Channel	Type	G_0 (pW/K)	β	R_0 (Ω)
A1	R	-	-	-
A2	D	650.3	1.16	92.2
A3	O	361.2	1.25	75.8
A4	O	303.0	1.31	83.0
A5	O	320.8	1.24	152.0
A6	O	358.0	1.26	89.8
B1	O	342.8	1.10	158.6
B2	O	365.4	1.07	198.4
B3	O	334.0	1.06	187.5
B4	D	412.9	1.25	106.1
B5	R*	-	-	-
B6	O	325.7	1.05	216.4
C1	O	341.1	1.17	81.1
C2	O	356.2	1.30	167.0
C3	O	322.1	1.31	93.0
C4	O	321.7	1.38	90.0
C5	R*	-	-	-
C6	D	325.0	1.33	104.0
D1	R*	-	-	-
D2	D	367.0	1.40	71.0
D3	O	338.6	1.17	82.3
D4	O	351.6	1.12	139.4
D5	O	390.4	1.10	128.3
D6	O	563.1	1.21	93.8

Table 2.1: Measured bolometer parameters under actual observing conditions on the Viper telescope during the 2005 season. Definitions of the parameters can be found in Appendix A. $\Delta = 41.8$ K is assumed for all channels. Channels are labeled according to whether they are connected to a resistor module (R), dark bolometer (D), or optical dolometer (O). Asterisks mark channels with electrical problems in 2005.

positioned in front the aperture, producing a periodic 300K to 77K temperature differential. Eccosorb[9] is a material designed as a microwave absorber which produces a nearly black body spectrum at millimeter wavelengths. An optical encoder measured the frequency of the chopping wheel. The response of the bolometer was measured using a lockin amplifier[10] at logarithmically-spaced frequency intervals to optimally sample the responsivity of a single-pole filter: $S(\omega) = S_0/\sqrt{1 + (\omega\tau)^2}$. The useable frequency range of the experimental setup was approximately from 2 to 100 Hz, which neatly covers the ACBAR signal band from 2 to 15 Hz. The frequency of the chopping wheel became irregular at low speeds, while at high frequencies and speeds, the wheel began to vibrate. The temperature dependence of the bolometer time constants was also investigated in a subset of the detectors. The time constant measurments were repeated at three electrical power loads, $V_{bias} \in \{100, 200, 500\}$ mV, with the optical loading fixed. In these tests, the bolometers sped up by as much as 45% as the electrical bias increased. This contributed to a nagging worry that the bolometers might be too slow with the sharply reduced optical loading on the telescope. Fortunately, this worry proved baseless: there is an inflection point in the time constant temperature-dependance curve. The bolometers were faster under the lower loading conditions on the telescope. The measured optical time constants on the telescope are listed in Table 3.7.

2.3   Dewar Optics: Filters and Feedhorns

Selecting the right frequency bands is a key element in a successful experiment. The frequency bands in ACBAR were selected based on a number of factors: detector technology, desired beam size, atmospheric transmission windows, foreground emission, and the CMB signal. ACBAR's original design included four frequency bands; however, only the 150 GHz channels have been analyzed for CMB science. The 150 GHz transmission window has low astronomical foregrounds and is near the peak

---

[9]Emerson & Cuming Microwave Products, http://www.eccosorb.com
[10]Stanford Research Systems; SR830
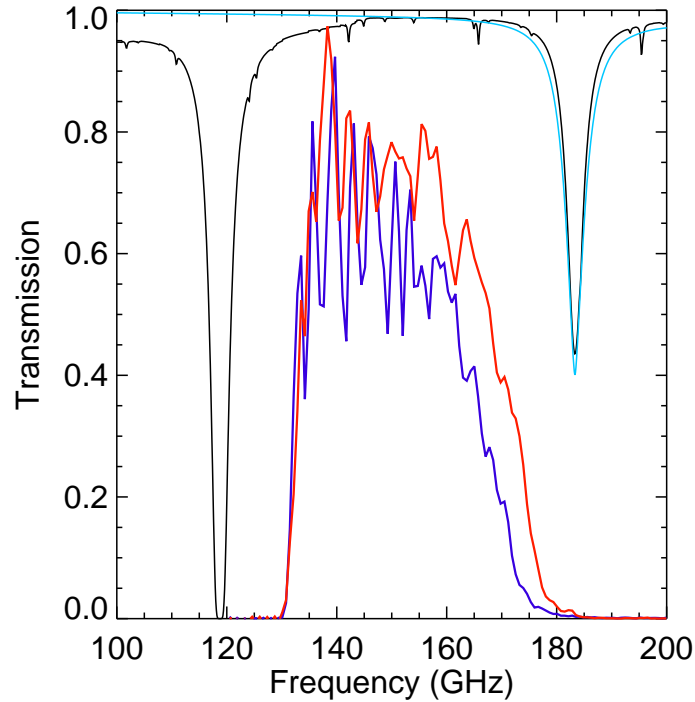
Figure 2.3: The average transmission spectra for the old (blue) and new (red) 2005 ACBAR 150 GHz channels. The new filter stack produced a wider band. The ACBAR band-pass has been plotted over the predicted zenith atmospheric transmission from the AT numerical atmospheric modeling code. The water vapor opacity predicted by the alternative modeling code ATM is shown in turquoise. ACBAR's 150 GHz band is carefully positioned between the oxygen line at 119 GHz and the water line at 183 GHz. The average zenith optical depth across the band is 0.03.

of the CMB black body spectrum. The sensitivity of the higher frequency channels dropped rapidly due to the falling CMB flux and the increasing atmospheric noise, and were removed for the 2005 season to increase the focal plane sensitivity at 150 GHz. As can be seen in Figure 2.3, the ACBAR 150 GHz band takes advantage of an atmospheric transmission window between two large molecular lines: an oxygen line at 119 GHz and a water line at 183 GHz. Hitting either line would dramatically reduce ACBAR's sensitivity.

The frequency band-pass of each ACBAR detector is set by the combination of a waveguide cutoff in the feed horn structure and resonant metal-mesh filters. As seen in Fig. 2.4, the feed horn's diameter narrows to a length of smooth-walled cylindrical

Filter	Temp	2005 new detectors	2005 original detectors	2002/2004 setup
Lense	240 mK	-	-	
Yoshinaga	240 mK	1.6 THz	1.6 THz	Ade # 2 (240 mK)
Pyrex	240 mK	1.2 THz	1.2 THz	Ade # 1 (240 mK)
Ade #2*	240 mK	270 GHz	255 GHz	Yoshinaga (4 K)
Ade #1* (Edge)	240 mK	170 GHz	169 GHz	Pyrex (4 K)
Ade #3*	4 K	173 GHz	234 GHz	
Lense	4 K	-	-	
Waveguide	4 K	131 GHz	131 GHz	
Ade #4	77 K	270 GHz	270 GHz	420 GHz

Table 2.2: The two filter stacks used for ACBARs 150 GHz channels in 2005. Ade refers to the metal-mesh filters. Three new metal-mesh filters were installed with the eight new 150 GHz channels. The eight original detectors continued to use the previous filter stack; however, the ordering was rearranged in an attempt to reduce thermal loading. We did not see a loading change. The filter ordering used in 2002 is listed for comparison; the placement of elements left blank did not change. A new 77K filter was installed for 2005. The previous 77K filter had accommodated all four frequency bands at the cost of slightly worse transmission at 150 GHz. The replacement was a 4' diameter version of the listed, new Ade #2 filter.

waveguide, which produces a reliable high-pass filter. The upper edge is set by metal-mesh resonant (MMR) filters provided by the Astronomy Instrumentation Group at Cardiff University. These filters are constructed of six to ten layers of delicate metal grids manufactured by photolithography which are hot-pressed between sheets of polypropylene for structural support. The filters can be intuitively understood as the optical equivalents of a LC filter. The shaping of the mesh determines the type of coupling, while the inter-mesh spacing introduces phase delays. The length scales can be tuned to achieve the desired frequency cutoff. The filters must be tested cold, as thermal contraction will tend to lower the characteristic frequencies by a few percent. The transmission of these filters opens up at harmonic multiples of the nominal edge frequency. These harmonic leaks are blocked by combining multiple filters with slightly different edges. The transmission of the metal-mesh filters also reopens at wavelengths much smaller than the characteristic length scale of the mesh. ACBAR uses a set of absorptive filters to block potential leaks at frequencies above 40 cm^{-1}.
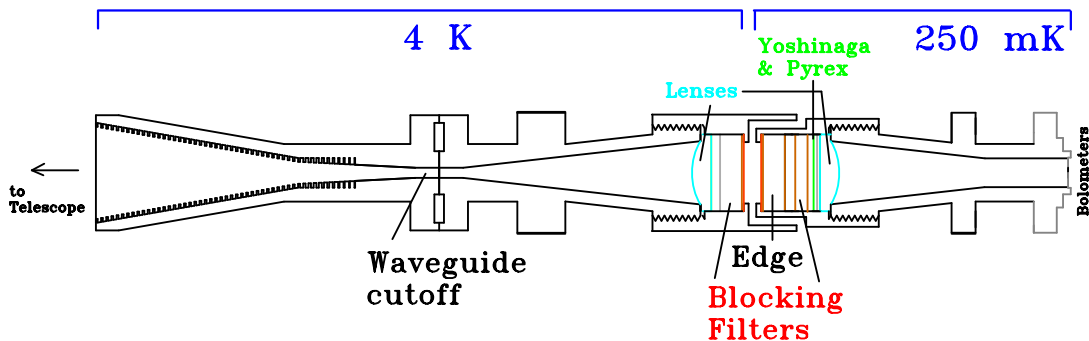
Figure 2.4: A schematic of the ACBAR back-to-back feed horns and filter stack. The lower edge of the ACBAR band-pass is set by the waveguide cutoff. The upper edge is set by the metal-mesh resonant filter marked 'Edge' positioned in the middle of the cavity where the rays are most nearly parallel. Two additional metal-mesh resonant filters are used to eliminate harmonic leaks. Two absorptive filters made of pyrex and Yoshinaga are placed last to catch any high-frequency leaks. The spacing between the filters is set by Eccosorb washers to block light from leaking around the edges of the filters. The filters are heat-sunk through the filter caps. Spring washers are used to maintain pressure.

Nine back-to-back feed horns were built for the 2005 season by Thomas Keating Ltd[11] on the same design as the eight existing 150 GHz feed horns. The feeds are designed to produce single-moded $\sim$5' FWHM gaussian beams on the Viper telescope with a waveguide cutoff of $\sim$131 GHz. The beam is defined by a corrugated scalar feed. For economic reasons, the horn transitions from corrugated to smooth-walled waveguide after the beam defining section. Figure 2.4 has a schematic of the feed horns. More information on the feed design can be found in [65] and [64].

Given the geometry of the feed horns, the trickiest machining is in the throat with the narrow grooves required for the corrugated-to-smooth wall transition. The throat is also the most difficult area to visually inspect on a completed horn. Any problems in the throat are likely to change the waveguide cutoff of the feed horn. To test this, we examined the band-pass of the feed horns at room temperature using a network analyzer at JPL. Custom-made waveguides provided a smooth transition, with an opening angle of $2° - 3°$ from the diameter of the ACBAR feed horn to standard

---

[11]http://www.terahertz.co.uk

waveguide parts. Three cases were tested: only the beam-defining scalar feed, all three horns connected together, and all three horns with coupling lenses designed to improve the coupling in the back-to-back section. We observed the waveguide cutoff clearly in all three cases. We did not observe any effect due to the coupling lenses. This was a fast way to check the feed horn performance, although its effectiveness as a diagnostic is uncertain in the absence of defective horns.

The performance of the filter stack that sets the upper edge of band-pass is critical to ACBAR's success. Hitting the water line at 183 GHz would be catastrophic. Two different filter stacks were used for the 150 GHz channels in the 2005 season. The eight original 150 GHz channels continued to use the original filter stack (hereafter referred to as "old" or "Stack A") with the same metal-mesh resonant filters as in 2002 and 2004. The eight new channels required an entirely new set of filters (hereafter referred to as "new" or "Stack B"), as Cardiff no longer produced the original filters. The fabrication, testing, and optimization of the filters for Stack B are discussed in more detail below. The final layout of the in-dewar optics is outlined in Table 2.2 and shown schematically in Figure 2.4. One metal-mesh filter sets the edge, while two additional metal-mesh filters located at 250 mK and 4 K are included in the filter stack to catch the harmonic leaks of the edge filter. The two absorptive filters are placed last in the optical path to block high-frequency leaks. Locating the absorptive filters at 250 mK effectively eliminates their own thermal emission, one contribution to the detector background loading. This placement also presents two reflective metal-mesh filters as the first objects in the optical path at 250 mK and 4 K. Reflective filters absorb less heat than their absorptive cousins and require less cooling power. This is important since the filters are indifferently heat-sunk with a small amount of Apiezon N thermal grease[12] and light pressure from the aluminum filter caps. Over-tightening the caps could damage the metal-mesh filters. The final filter stack fulfilled all of ACBAR's requirements: high optical efficiency, low background loading, and no detectable out-of-band leaks.

---

[12]Apiezon Products, Manchester M32 0ZD, UK

ACBAR uses two absorptive filters: one pyrex filter[13] and one Yoshinaga filter. The thickness of each one is tuned to $\lambda/(2n)$, where n is the index of refraction to minimize the transmission losses due to reflections. The amorphous structure of pyrex is an effective infrared absorber at wavelengths between $40\ \mathrm{cm}^{-1}$ and $2000\ \mathrm{cm}^{-1}$. The Yoshinaga filter [83] is a mixture of powdered thallium bromide salt suspended in polyethylene merged with black polyethylene that blocks frequencies above $55\ \mathrm{cm}^{-1}$. The Yoshinaga filter is intended to complement the pyrex filter by blocking any leaks above $2000\ \mathrm{cm}^{-1}$. The Yoshinaga filters were punched out of a large, retired filter that had been used as a 77 K blocker in 2001. We saw no evidence that the absorptive filters reduced optical loading with filter stack B. These tests were done in a test dewar before deployment and were not repeated with the actual ACBAR dewar. The absorptive filters had reduced the background in earlier tests with filter stack A. The final version of filter stack B included the absorptive filters on the precept of 'better safe than sorry.'

The lab tests actually used a black polypropylene filter in place of the Yoshinaga filter, as we were unable to find a supplier of Yoshinaga filters due to the toxicity of the Thallium Bromide salt. The black polypropylene replacement filters were manufactured from a mixture of 2% carbon black and 98% optical grade polypropylene by mass. The carbon black is mixed into the melted polypropylene, and the mixture is cooled in sheets of set thicknesses on a hot press. It is important to keep the polypropylene temperature between the melting and boiling point to avoid bubbles. The filters were punched out of the film.

The metal-mesh resonant filters are the trickiest and most complex parts in the ACBAR filtering scheme. This is doubly true since they are designed for parallel waves in free space and ACBAR embeds the filters in a conical waveguide cavity. The exact frequency cutoff can be up to 5% off from the design frequency. Even if the filters were perfect, light might leak around the edges of the filter. Both the individual filters and filter ordering of Stack B went through several iterations before we found a filter stack with a reasonable optical efficiency, no high-frequency leaks, an

[13]Custom Scientific Optics & Filters, Phoenix, Arizona USA
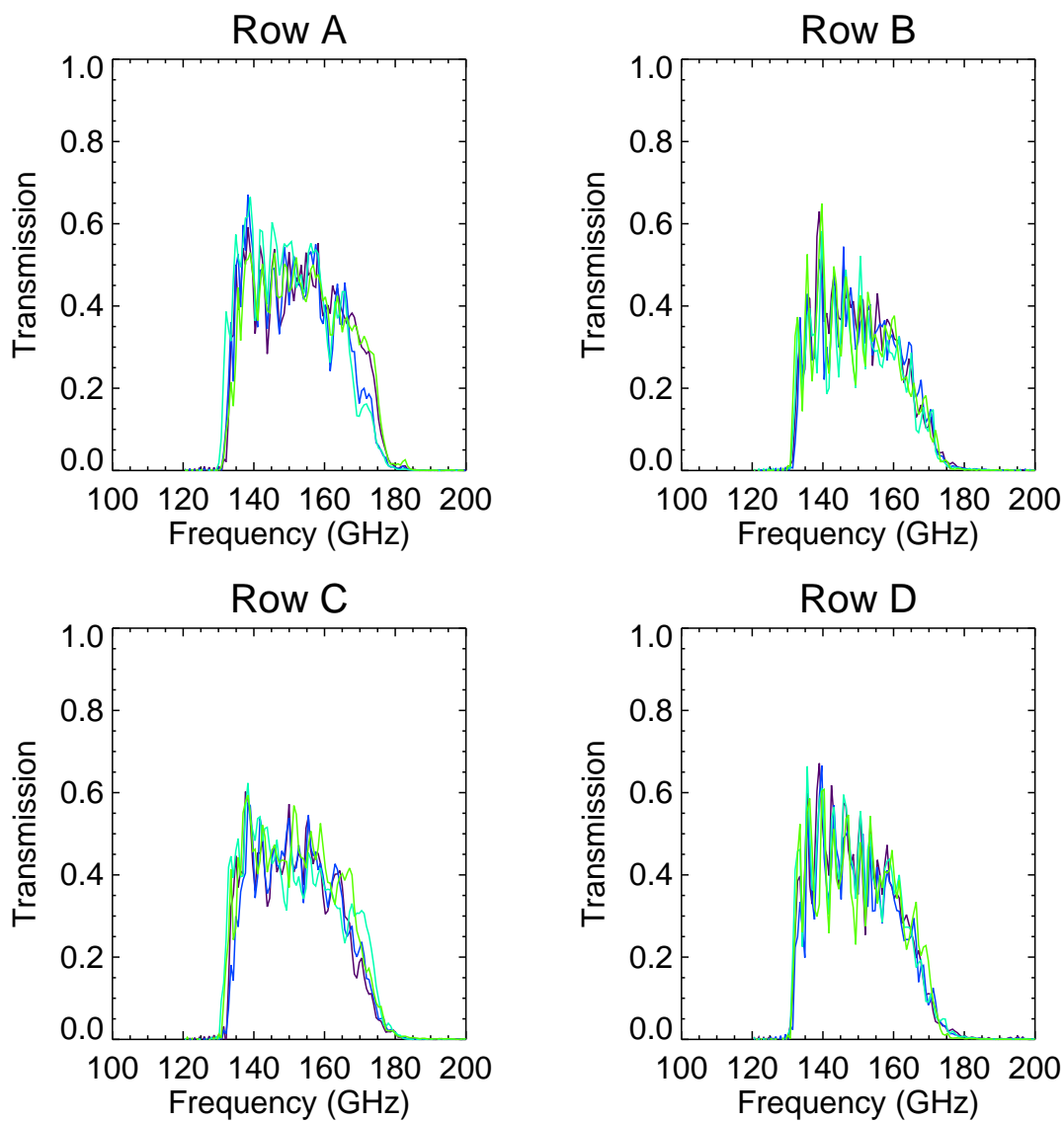
Figure 2.5: The transmission spectra for the 2005 ACBAR 150 GHz channels. The spectra for the 16 channels have been divided into sets of four. On the left-hand side, Rows A and C are the eight new 150 GHz channels. On the right-hand side, Rows B and D have the same filters and bolometers as 2002 and 2004. The band-passes were measured in the ACBAR dewar in December 2004 using a portable FTS setup. The band-passes have been normalized by optical efficiency estimated from the observed power differential between a 288K and 77K source.

upper-edge that avoided the water line at 183 GHz, and an acceptable optical loading. In practice, the problematic requirements were the location of the upper-edge and the elimination of high-frequency leaks. These tests were done in parallel with the BICEP experiment and used BICEP feed horns and bolometers, as the ACBAR equivalents were in the process of being manufactured.

Fourier transform spectroscopy was used to measure the band-pass of the complete optical stack. The spectra were measured out to 234 GHz with a frequency resolution of 458 MHz and noise floor of -20 to -25 dB. Due to time constraints, individual filters, and feed horns were tested as a single unit. Fortunately, we discovered no evidence for significant variations between the band-pass of individual filters or feedhorns. We remeasured the band-passes after installing the feeds, filters and detectors in the ACBAR dewar with a portable FTS setup brought to the South Pole for that purpose. The transmission spectra in the ACBAR dewar are plotted in Fig. 2.5.

The transmission spectra can be convolved with an atmospheric model for the South Pole to estimate the expected atmospheric opacity and atmospheric loading. Two numerical atmospheric modeling codes, AT [26] and ATM [55], predict atmospheric opacities at millimeter wavelengths. ATM breaks down the total opacity according to the contributions from each component of the atmosphere, notably water vapor. This is useful, as the bulk of the variability in atmospheric loading will come from turbulence in the poorly mixed water vapor. However, previous ACBAR measurements suggested that ATM overestimated the absolute opacity and that the AT predictions were more accurate [64]. We renormalized the ATM opacities to match the average AT opacity across the band. When testing different filters, the water vapor opacity and the total opacity were both considered as figures of merit.

We also need to ensure that the filter stack has a reasonable optical efficiency. In the Poisson limit of photon noise, the signal-to-noise will improve as the optical efficiency increases. The predicted optical loading on a bolometer can be parametrized as

$$P_{opt} = \epsilon \int d\nu \, f_b(\nu) B_\nu,$$

where ϵ is the optical efficiency, f_b is the transmission of the band, and B_ν is the spectrum of the source. Clearly, there is a degeneracy between the normalization of the band-pass f_b and optical efficiency ϵ. The percentage of photons that reach the detector will be frequency dependent. We are most interested then in the band-averaged optical efficiency.

There are three elements that go into the optical efficiency measurement: a differential optical power measurement between two or more sources, the transmission of the band-pass, and the spectrum of each source. The optical power differential can be calculated by running a load curve with each optical load. Using the thermal model of a bolometer, the power absorbed by the bolometer can be calculated from its temperature. More robustly, the power differential can be calculated in a model-indepent fashion by isolating regions in both load curves with the same bolometer resistance (and temperature). Energy must be conserved so the difference in applied electrical power will equal the difference in optical power: $\delta P_{elec} = -\delta P_{elec}$. In practice, there can be complications for large power differentials. The electronics will impose an upper limit on the applied electrical power. A large increase in optical loading may also heat up other parts of the dewar such as the filters, changing the internal loading and inflating the apparent optical efficiency. The magnitude of this effect depends on the quality of heat-sinking inside the dewar. The internal loading in the test dewar changed noticeably between room temperature and LN_2 loads. However, the heat-sinking in the ACBAR dewar was sufficiently good that we did not see evidence for similar filter heating at the Pole. The other two elements in determining a meaningful optical efficiency are the spectrum of the source and the band-pass of the detector. For these tests, we construct a black body optical load from sheets of Eccosorb submerged in a bath of a liquid of known temperature (LHe, LN_2, LO_2, ice water, and room temperature). The load is placed directly in front of the window of the dewar with baffles to avoid coupling to other sources in the room. The band-pass was measured using Fourier transform spectrography. The band-averaged optical efficiencies are listed in Table 2.3.

The optical loading naturally depends on the detectors and feed horns as well

Channel	$\delta Q(\delta_T = 211.2K)$ (pW)	ϵ_{opt}	$\langle\epsilon_{opt}\rangle_{135-165GHz}$
A3	107.6	0.67	0.49
A4	102.9	0.59	0.45
A5	107.9	0.57	0.47
A6	98.9	0.67	0.45
B1	76.8	0.64	0.38
B2	71.8	0.54	0.35
B3	67.3	0.58	0.32
B6	72.8	0.65	0.34
C1	101.5	0.60	0.46
C2	100.1	0.63	0.43
C3	89.9	0.58	0.43
C4	91.2	0.60	0.43
D3	86.6	0.61	0.40
D4	90.2	0.66	0.43
D5	89.2	0.67	0.43
D6	81.6	0.67	0.40

Table 2.3: Measured bolometer optical efficiency in the ACBAR dewar on 12/27/2004 between LN_2 and room temperature (77K and 288.2K, respectively). The three columns show the measured optical power differential, the normalization applied to the measured band-pass, and the average optical efficiency between 135 and 165 GHz.

as the filters. We repeated the loading measurements with the ACBAR feed horns and bolometers and discovered that the loading was higher than expected based on measurements with the BICEP horns. The source of the loading was tracked to light leaking out through the narrow thermal gap between 250 mK and 4K. The filter caps were originally gold-plated and highly reflective. Blackening the 250 mK side with Bock black (a mixture of carbon and Stycast) dropped the optical loading in half from 30 pW to 15 pW. The magnitude of this effect might be related to the different throughputs of the 250 mK feed and the 4 K feed. The inner diameter of the 250 mK feed was over-sized in order to increase the optical efficiency [64]. However, in addition to improving optical efficiency, this extra throughput is believed to have spilled into the 4 K cavity and increased the total loading. Blackening the 250 mK filter caps intercepted these rays at 250 mK.

Even small high-frequency leaks can contribute large amounts of power, as the spectra of most background sources is rising as ν^2 and sufficiently high-frequencies can

excite multiple spatial modes ($A\Omega/\lambda^2 > 1$) in a single-moded horn. So-called thick-grill tests provide a robust method to detect high-frequency leaks via the quantity of interest: the optical power absorbed by the detector. A thick-grill filter (TGF) is a sheet of metal with a closely spaced array of holes of fixed diameter. The sheet will block wavelengths above the waveguide cutoff determined by the hole diameter. For a TGF cutoff above the band-pass of a perfect filter stack, the thick-grill filter would look exactly like an unbroken metal sheet. The optical signal should vanish when either one is placed in front of the dewar window. Any residual signal is evidence for a leak. The frequency of a leak can be pinned down by using thick-grill filters with different frequency cutoffs. The experimental setup is very similar to the optical time constant measurement with the substitution of a much brighter, chopped thermal source. A digital lockin is used to maximize the signal-to-noise of the measurement at the chop frequency. The measurement is repeated with the window open, blocked by each thick grill filter, and blanked off. The three data points yield the total signal, the out-of-band signal, and a zero point. In the final set of thick grill tests before putting ACBAR on the telescope, we measured total signal voltages of 800 to 1000 mV and out-of-band signal voltages of 0.1-0.5 mV for rejection level in power of >10,000. The responsivity of the bolometers is lower in the total signal case due to heating of the bolometers. The noise floor appeared to be $\sim$ 0.1-0.2 mV. The filter stack did an excellent job of eliminating high-frequency leaks.

2.4   Cryogenics

There are five temperature stages in the ACBAR dewar. The outside of the dewar is wrapped in insulating blankets and is heated above the ambient temperature for the sake of the attached electronics and vacuum o-rings. Moving inwards, there is a liquid nitrogen stage at 77K and then a liquid helium stage at 4K. There is no vapor-cooled intermediate stage. Swathes of aluminized mylar loosely wrap each stage, taking advantage of a reverse greenhouse effect to reduce the optical load from warmer stages. The cryogen tanks are over-sized for the sake of the winter-overs
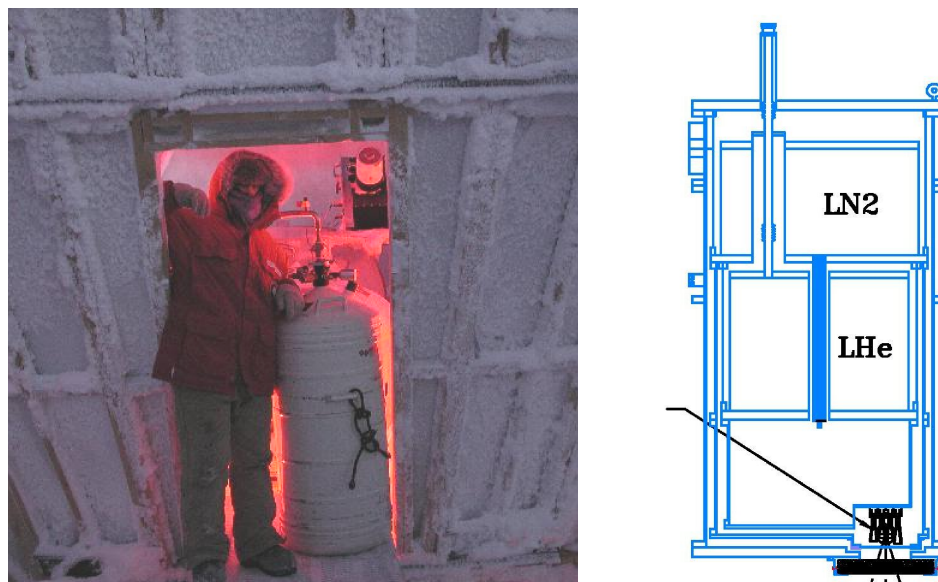
Figure 2.6: On the **left-hand side**, Matt Newcomb filling LHe$_4$ during the winter of 2002. On the **right-hand side**, a schematic of the cryogenic tanks in the ACBAR dewar.

who have to brave the outdoor weather to refill the liquid cryogens. The hold time is approximately three days. Figure 2.6 has a photograph of a mid-winter helium refilling by Matt Newcomb along with a schematic of the ACBAR dewar.

The liquid cryogenics supply is a potential failure point at the South Pole for experiments like ACBAR. LN$_2$ is produced by a single on-site plant. The LHe$_4$ supply is shipped in to the South Pole station during the Austral summer and must last all winter. The helium supply ran out mid-winter in two of the five years in which ACBAR was scheduled to observe, 2003 and 2004. Although it has never failed during the winter, the solitary LN$_2$ plant is another single point of failure. There is a strong argument for using closed-cycle mechanical coolers instead of liquid cryogens at the Pole to avoid these risks in future experiments.

The focal plane is cooled to 232 mK by a three-stage He3-He3-He4 sorption refridgerator[14] . A thermal diagram of the fridge is shown in 2.7. ACBAR used two fridges of similar designs during the years it observed. The original fridge had a hold time of 36 hours, a cycle time of 4 hours, and reached temperatures of 235 mK. This

---

[14]Chase Research Cryogenics Ltd, Sheffield UK
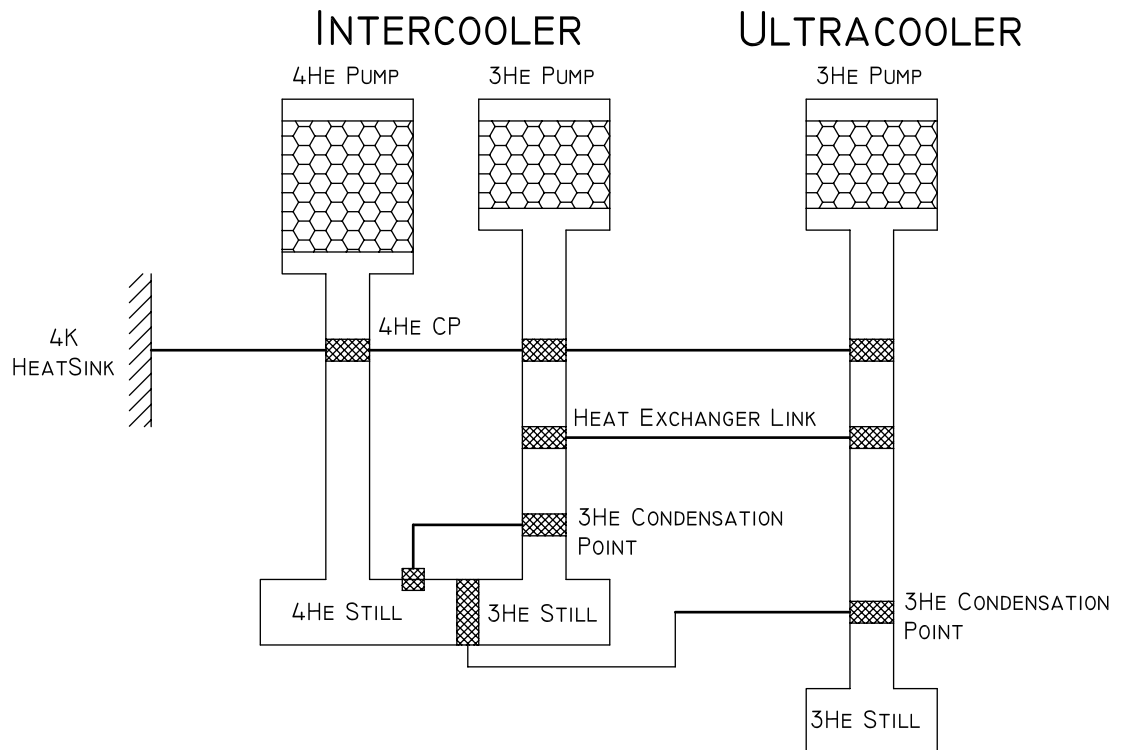
Figure 2.7: A schematic of the three-stage He3-He3-He4 fridges made by Simon Chase and used in ACBAR. The image is taken from [3].

fridge developed problems while being stored at room temperature from July 2004 to November 2004. We believe it developed a leak, but did not check for helium gas till we realized the fridge was behaving erratically. At that point, the dewar had been open for a week to retrofit the focal plane. The leak checker did not detect helium gas. Fortunately, a nearly identical fridge was available in California, and amazingly it reached the South Pole in under a week. The fridge cycle was adapted to the peculiarities of the new fridge. With the new fridge and cycle, the fractional downtime for cycling remained approximately the same, with a shorter hold time of 24 hours and a shorter cycle time of two hours. Unsurprisingly, the 24 hour cycle proved less stressful for the winter-over and led to an overall increase in observing efficiency. Less advantageously, the daily cycle reduced the azimuthal variation in observations of sources used for the pointing model, as the fridge cycle and start of the observation script could be scheduled for the same time each day. In hindsight, it would have been intelligent to occasionally rearrange the order in which sources were observed to improve the pointing model in 2005.

The focal plane temperature was very stable during each season. The measured temperatures over the course of 2005 as can be seen in Figure 2.8. Thermal stability is important, as the bolometer responsivities will vary depending on the focal plane temperature. Increasing the baseplate temperature by 5 mK will change a typical ACBAR bolometer's responsivity by 2.5%. This variability is expected to average down to negligible levels compared to ACBAR's 2.2% absolute calibration over a year of observations.

2.5   Telescope & Pointing

ACBAR is mounted on the Viper telescope. Viper is a 2.1m off-axis gregorian telescope originally built to make CMB measurements with a two pixel 40 GHz HEMT receiver. From its installation at the South Pole in January 1998 to its decommisioning in January 2006, the telescope hosted three long-term experiments: the HEMT-based CORONA experiment ([56]) in 1998 and 1999, SPARO ([18], [53], [61]) in 2000 and
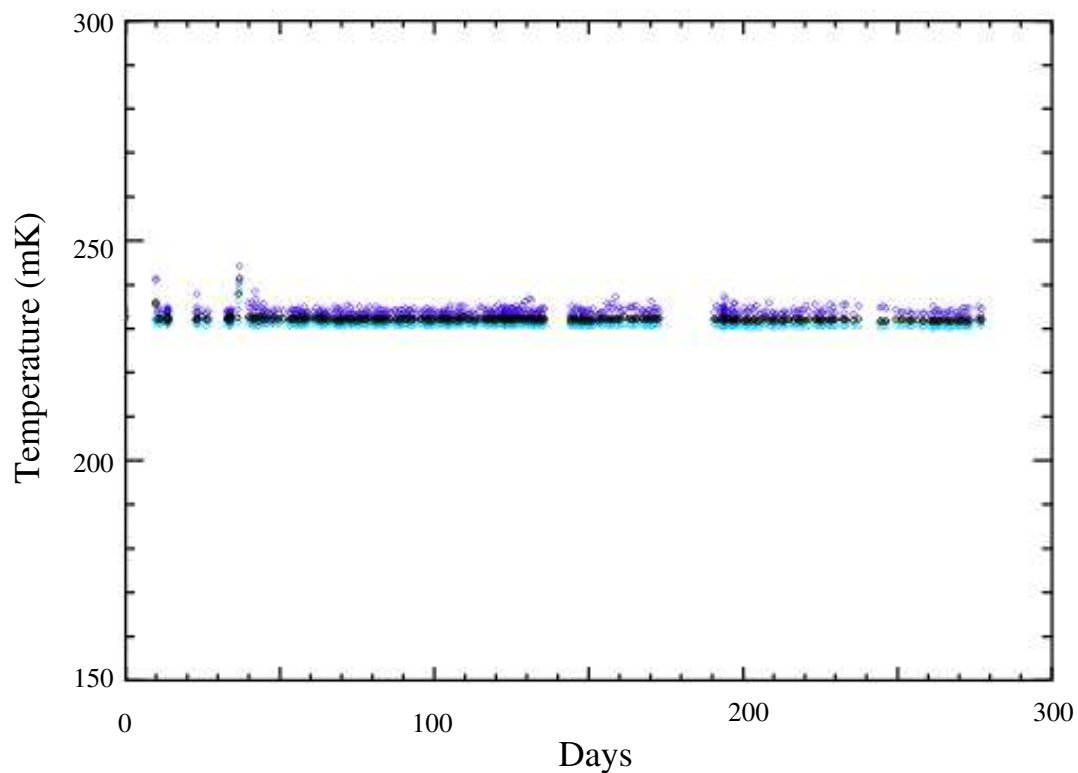
Figure 2.8: The ACBAR focal plane temperatures are very stable for all CMB observations in 2005. The minimum temperature the focal plane reaches during an observation is plotted in torquoise. The maximum temperature is plotted in purple, and the average temperature is plotted in black. The mean focal plane temperatures in 2001-2004 are slightly different due to small differences between the two fridges. The variability before Day 50 is related to telescope maintenance - no CMB observations from this period are used. The gaps in the middle of the season are downtime due to heavy storms or maintenance.
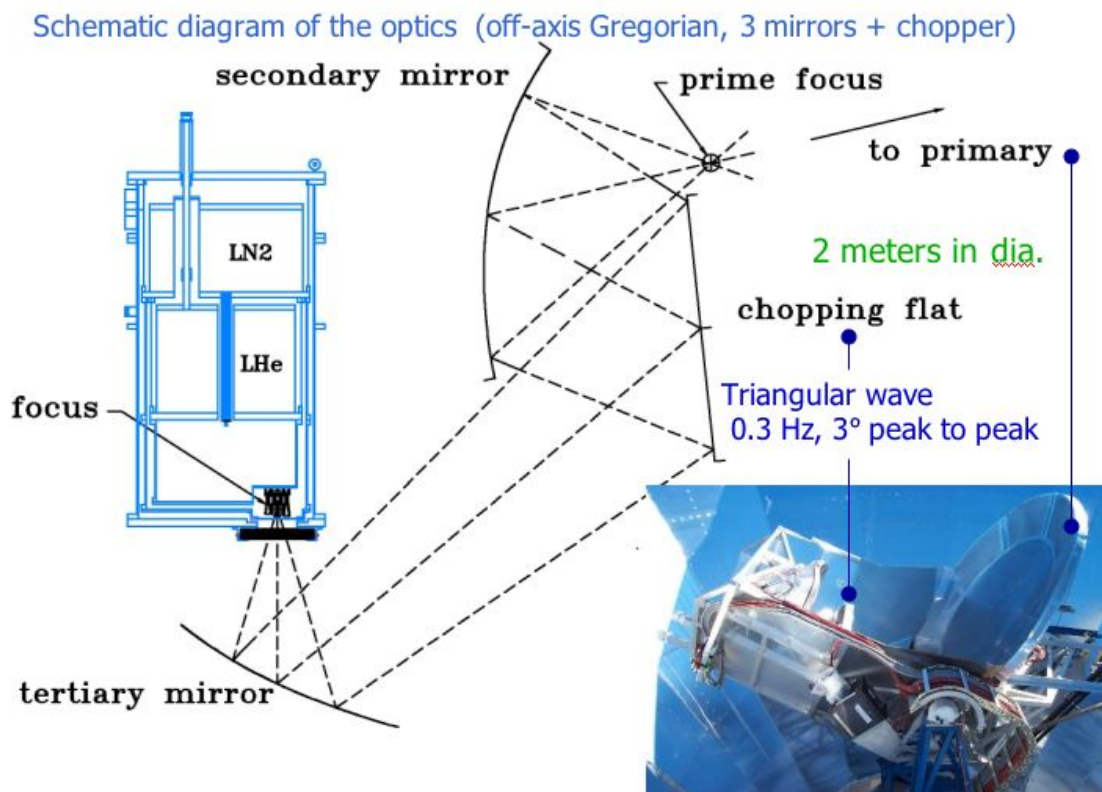
Figure 2.9: A diagram of the Viper telescope, taken from [64]. Viper is a 2.1 m off-axis Gregorian telescope. At 150 GHz, the telescope can achieve 4.7' beam FWHMs. A photograph of the telescope during the summer is located in the lower right corner. The ground shield and reflective baffles to reduce ground spillover can be seen. The chopping mirror and primary are marked. The ACBAR dewar is hidden behind the baffles on the left side.

2003, and finally ACBAR in the Austral winters of 2001, 2002, 2004, and 2005. A schematic of the telescope can be seen in Fig. 2.9. A ground shield surrounds the telescope and baffles are positioned around the mirrors to redirect any spillover onto the sky rather than the ground.

A calibration source is positioned behind the tertiary mirror and visible through a small aperture drilled in the center of the mirror. The hole is plugged with polypropylene to keep ice out. The source consists of a small temperature-controlled Eccosorb source positioned behind a chopping wheel. More details can be found in [41]. The majority of the time the calibrator is maintained at ambient temperatures and all the components are weatherized to survive the cold. The calibrator can be used to
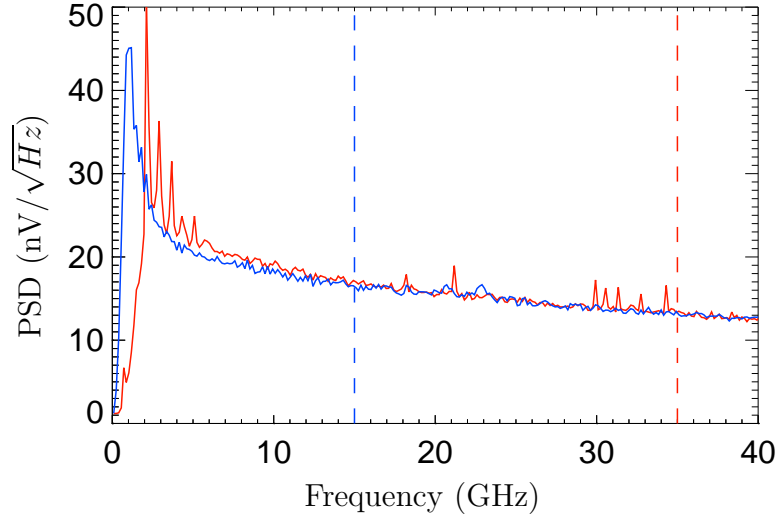
Figure 2.10: PSDs for channel D3 averaged over an entire CMB observation. D3 is worse than average for microphonic lines. A quadratic has been removed from each chopper sweep, but the bolometer time constant has not been deconvolved. The CMB observations were made under good observing conditions on 6/18/2004 (red) and on 6/06/2005 (blue). The chopper frequency was slightly more than twice as fast in 2004 (0.7 Hz vs. 0.3 Hz). The frequency equivalent to $\ell = 3000$ is marked with a vertical dashed line of the respective color to mark the end of the useful signal band. Note that even under good observing conditions there are a host of small microphonic lines in the 2004 data near 20 Hz and above 30 Hz. The chopper harmonics at low frequencies are also slightly more prevalent. Otherwise, the PSDs are quite similar.

measure bolometer time constants under the actual optical loading conditions on the telescope (see Sec. 3.6) and to measure the bolometer responsivity to calibrate the experiment over short timescales.

The Viper telescope scans by means of a chopping flat mirror positioned between the secondary and tertiary mirrors. The telescope points at a fixed RA and Dec position while the chopping mirror moves the beam across the sky. The chopping mirror is carefully counter-balanced to avoid vibrating the telescope and is propelled by induction coils. A full description of it can be found in [41]. Various waveforms can be used for the chopper motion; ACBAR uses a triangular wave which moves the beam at a constant velocity of approximately $1.8°/s$ and full range of $\sim 3°$. The elevation is nearly constant throughout the chopper scan, reducing the atmospheric

signal caused by looking through different optical depths. Later in this work, we will refer to each separate telescope pointing as a stare. Each period of the chopper mirror can be divided in half based on the direction of motion and labeled as a chopper sweep. For example, a 30s stare means that the telescope was pointed at a single spot for 30s. In that time, there would be ∼10 chopper periods and 20 chopper sweeps.

For the 2004 CMB observations, the chopper frequency was increased to 0.7 Hz from 0.3 Hz. The intention was to move the signal bandwidth to higher frequencies away from the 1/f noise. The ACBAR detectors are fast enough to support a higher scan speed. The attempt back-fired, as the faster chop speed caused vibrations that excited microphonics within the signal band in a subset of channels. We also saw evidence that the chopping mirror was vibrating, leading to a comb of harmonics of the chop frequency in the noise power spectral density (PSD). The differences between a 0.3 and 0.7 Hz chopper frequency are illustrated in Figure 2.10. The science results in this work are from observations with the chopper period set at 0.3 Hz.

The Viper telescope's nominal pointing drifts between years as the ice settles. A simple global offset calculated at the beginning of each season is sufficient to get the pointing accuracy to a few arcminutes. A multi-parameter pointing model was developed for the telescope. Each season is split into a small number of temporal periods with set pointing parameters. The splitting is necessary because on rare occasions we observed abrupt pointing steps of an arcminute or two. Presumably, this was caused by a settling event of the telescope's foundation. The parameters of the pointing model are derived from observations of galactic and extra-galactic sources with known positions. The model is checked on the coadded observations of the CMB quasars. These quasars are not used in deriving the model. The estimated pointing RMS for each year is listed in Table 2.4.

2.6   Electronics

The ACBAR electronics were designed with the strengths and weaknesses of bolometers in mind. Due to the high impedance of NTD thermistors, bolometers are ex-

Year	δRA ($''$)	δDec ($''$)
2002	16.9	25.2
2004	18	24
2005	21	36

Table 2.4: Estimated pointing uncertainties from the residual scatter source locations after the ACBAR pointing model has been applied. The pointing model is populated with observations of Galactic and Extra-galactic sources with known positions. The pointing errors are larger in 2005 due to the reduced azimuthal variation for the source observations .

tremely sensitive to microphonics. The length of high-impedance wiring is minimized by passing the bolometer signals directly to JFETs in a nearby, sealed box off the 4 K stage. The JFETs are temperature-controlled, as their performance is temperature dependent. From the JFETs, the signal runs directly to warm amplifiers situated in two RF-sealed boxes bolted to the side of the dewar. The electronics are described in more detail in Runyan et al. [65] and Runyan [64]. Each channel is digitized and saved at two levels of amplification. The DC-levels are amplified by a factor of 200. After this initial amplification, a single-pole high-pass filter with $T = 0.1s$ is applied to remove the DC component. The higher frequencies are amplified by an additional factor of 200 for a total amplification factor of 40,000. The DC signals are used for tests such as bolometer load curves and sampled at a few Hz. The science results are derived from the AC signals. After an anti-aliasing filter, the AC voltages are sampled by a 16 bit A/D converter at 2400 Hz in 2002 and 2004, and 2500 Hz in 2005. The samples are box-car averaged in groups of eight before being written to disk for an effective sampling rate of 300 - 312.5 Hz.

ACBAR uses NJ132 JFET follower pairs manufactured by Interfet[15]. Three out of twenty JFET pairs failed over the operating lifespan of the experiment. Two JFET pairs which read dark bolometers failed between 2002 and 2004. A third resistor channel displayed symptoms of contact noise during preparations for the 2005 observing season. No repairs or detailed diagnostics were attempted for any of these channels, as sufficient dark channels remained operational for the science

---

[15]Interfet, Garland, TX 75042

results. Opening the dewar introduces risk, including the possibility of additional JFET failures during the thermal cycle.

Chapter 3

Observations and Performance

3.1 The South Pole Environment

The South Pole is a superb site for microwave observations. Operating in such a remote environment would be impossible without the logistics support provided the United States Antarctic Program. The Amundsen-Scott South Pole Station is located at an altitude of 9300 feet (2847 m), however the effective altitude is approximately 10,500 feet due to the Earth's rotation. The South Pole is one of the coldest places on the Earth, with average winter temperatures between $-40°$ and $-70°$ C. The six winter months of uninterrupted darkness allow continuous observing with excellent thermal stability. The weather conditions are generally quite stable during the winter, with the weather being dominated by a flow of cooling air from the Antarctic plateau to the coast. The measured background loading during the 2005 observing season is plotted in Fig. 3.1 to illustrate its stability.

The freezing temperatures contribute to the extremely dessicated conditions at the Pole; the saturated vapor pressure of water is very low. At 0.26 ± 0.2 mm, the mean integrated precipitable water column depth during the winter is much lower than the precipitable water measured for the best six months at other sub-mm sites such as Mauna Kea (1.65 mm) and Atacama (1.00 mm) [46, 12]. While other gases contribute to a constant background at 150 GHz, water vapor is poorly mixed in the atmosphere, causing the optical loading to fluctuate as turbulent flows combine. The dry conditions significantly reduce atmospheric noise.
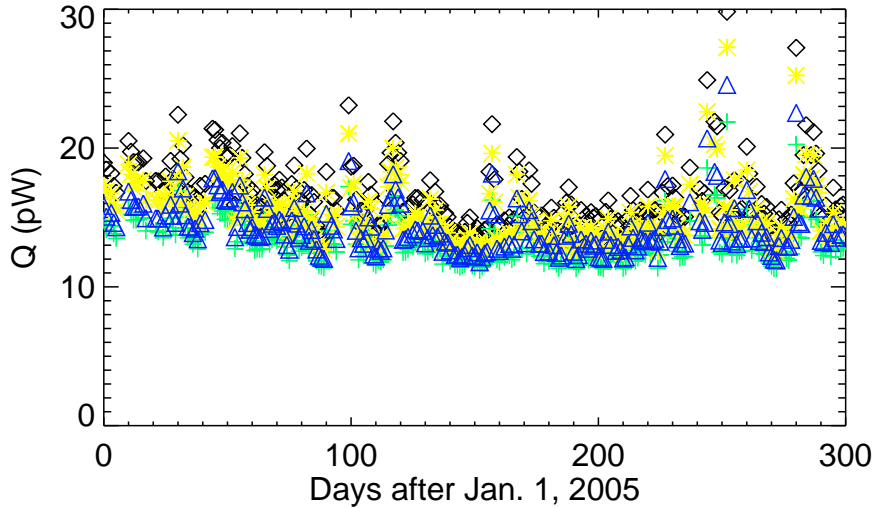
Figure 3.1: The optical loading measured during the 2005 Austral winter. The average loading for each row of four detectors is plotted (Row A is black, Row B is torquoise, Row D is blue, Row C is yellow). The persistent differences are caused by slight differences in the bandpasses and optical efficiency of the detectors.

3.2 Sky Coverage

ACBAR has conducted CMB observations in $\sim$700 deg^2 of sky spread across 10 fields. Statistics about the ACBAR fields are presented in Table 3.1. Every ACBAR field is situated at high Galactic latitude in a region of low dust emission to minimize the amplitude of the synchrotron and dust foregrounds (see Figure 3.2). The dust emission measured by IRAS at 100 microns in the ACBAR fields is 1 MJy/sr, while the average emission over the entire sky is 16 MJy/sr. The 2005 observing season dramatically expanded the ACBAR sky coverage, adding 490% more area. The four fields observed in 2001 and 2002 are approximately 25 deg^2 in size. The six fields added in 2005 are each around 90 deg^2. This reflects a deliberate change to the observing patterns, driven by a new calibration strategy and a new focus on the power spectrum at larger angular scales.

Going into the 2005 season, we planned to calibrate the ACBAR data set with a direct comparison of the ACBAR maps to the maps of either B03 or WMAP. Preliminary simulations done by Jon Goldstein indicated that the calibration error

would be similar for both paths. The CMB8 field covers 60 deg^2 of the B03 deep region. The positions of the six large fields, CMB7ext, CMB9, CMB10, CMB11, CMB12, and CMB13, were selected based on WMAP's per-pixel integration time from the low-dust sky visible at elevations of $>45°$. The selection effect is mild since WMAP has fairly uniform coverage in this region. The calibration is discussed in detail in §3.4.3.

Expectations for the power spectrum were modeled as part of the planning process for the 2005 season and focal plane refurbishment (§2). The modeling was later expanded to analyze the effects of observation strategies. A small number of predicted band-power and calibration errors were passed to CITA to evaluate the cosmological parameter implications of reducing the band-power errors at different angular scales. Given the ACBAR beam size $\ell_{beam} \sim 1450$, it is difficult to push the ACBAR power spectrum to angular scales smaller than $\ell = 3000$. Secondary anisotropies also become increasingly important at $\ell > 2500$ and are impossible to disentangle from the primary anisotropies with a single frequency experiment. On the other hand, the ℓ-range from 800-2000 is an easy target for ACBAR, with the K07 band-power errors being dominated by cosmic variance. This ℓ-range is also more interesting than $\ell > 2000$ for cosmological parameter estimation due to the presence of the fourth and fifth acoustic peaks. The decision to focus attention on ℓs around 1200 meshed perfectly with the WMAP-based calibration strategy; both required a significant increase in ACBAR's sky coverage.

3.3   Beams

An accurate beam measurement is required to calculate the experimental window function for the CMB power spectrum analysis. Mistakes in the beam function can introduce a tilt or amplitude shift to the power spectrum, hampering efforts to constrain similar cosmological effects such as the running of the scalar index. The ACBAR beams are well-described by symmetric gaussian functions, with their main beam FWHM determined to 2.6% by in situ measurements of the images of bright

Field	RA (°)	Dec (°)	Area (deg^2)	Time (hrs.)	Year	# of detectors
CMB2(CMB4)	73.963	-46.268	26(17)	506(142)	2001(2002)	4(8)
CMB5	43.371	-54.836	28	1656(665)	2002(2005)	8(16)
CMB6	32.693	-50.983	23	351	2002	8
CMB7(ext*)	338.805	-48.600	28(107)	420(778)	2002(2005)	8(16)
CMB8	338.805	-48.600	61	1072	2005	16
CMB9*	359.818	-53.135	93	252	2005	16
CMB10*	19.544	-53.171	93	224	2005	16
CMB11*	339.910	-64.178	91	308	2005	16
CMB12*	21.849	-64.197	92	168	2005	16
CMB13*	43.732	-59.871	78	477	2005	16

Table 3.1: The central coordinates and size of each CMB field observed by ACBAR. The fifth column gives the detector integration time for each field after cuts. The last column gives the number of 150 GHz detectors. The detector sensitivity was comparable ($\sim$10%) between 2002 and 2005. The six largest fields (marked with a *) are used in the calibration to WMAP. Note that the 2005 observations extended the declination range of the CMB7 field, leading to the combined field CMB7ext. CMB2(CMB4) and CMB8 also partially overlap, but are analyzed separately for computational reasons. Approximately 1/4 of the CMB2(CMB4) scans have been discarded to eliminate the overlapping coverage. The listed numbers reflect this loss.

quasars located in the CMB fields. Beam maps off these sources have the advantage of naturally including pointing jitter and any other issues which might affect the instrumental beam for the CMB observations. The quasars can probe the beam to 15 to 20 dB before hitting the CMB confusion limit. The beam sidelobes are measured to 30 dB with observations of Venus made in 2002. There are extended periods during which ACBAR was unable to observe Venus, requiring us to estimate the stability of the sidelobes across multiple years. Coadded RCW38 observations are used to set an upper limit on the sidelobe variability. The chopper mirror modulates the positioning of the beam on the mirrors slightly, which leads to a variation in the beam size with chopper position [65]. RCW38 observations are also used to characterize the dependence of the beam on chopper position. We discuss each of these steps in more detail below.

The most detailed measurements of the ACBAR beams are from observations of Venus made in 2002. Venus has an angular size of $\lesssim 1'$, so it is effectively a point
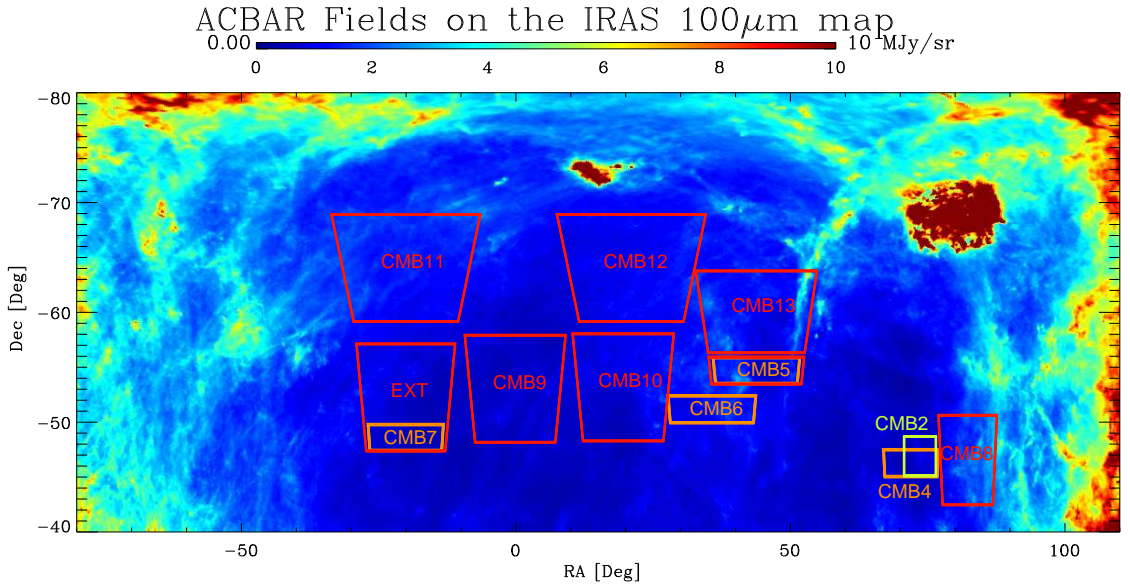
Figure 3.2: The ACBAR fields overlaid on the IRAS dust map. The position of each field is plotted and labeled with the detector integration time in each year. The color coding indicates the year in which the observations occured: yellow ≡ 2001, orange ≡ 2002, and red ≡ 2005. The bulk of the 2005 season was targeted at large, comparatively shallow fields, increasing the total sky coverage by a factor of six. The fields are plotted on top of the 100 μm IRAS dust map [68]. Each field has been targeted at the "Southern hole," a region of low dust emission visible from the South Pole. The average dust emission at 100 microns in the ACBAR fields is $1MJy/sr$, only 6% the all-sky average of $16MJy/sr$. The CMB8 field (lower right corner) was targeted at the deep region of the B03 experiment as an alternative calibration path to the WMAP cross-calibration used for the results presented here.

source for the 5′ ACBAR beams. Venus is extremely bright at 150 GHz, with a peak amplitude of 5 K in an ACBAR CMB calibrated map. This is about 70 times as bright as RCW38 and 50,000 times as bright as the largest CMB anisotropies in the ACBAR maps. A single hour-long Venus observation can constrain the sidelobes to -30 dB in intensity. The weather during the Venus observations was excellent, leading to small chopper synchronous offsets and simplifying the measurement of the sidelobes. The timestreams are low-pass filtered at 40 Hz and binned into 1′ chopper bins. A first-order polynomial is removed from each stare. To avoid introducing shadows around Venus or filtering the sidelobes, points within 15′ of the planet are masked and do not affect the polynomial fit. Stares from all eight channels (there
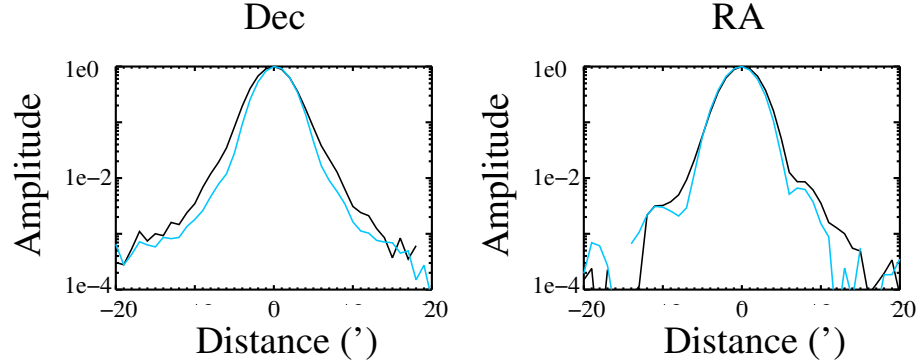
Figure 3.3: Cross-sections of Venus as observed by ACBAR. The **left-hand plot** shows the cross-section perpendicular to the scan direction while the **right-hand side** displays the beam profile in the direction of the motion of the chopping flat mirror. The telescope geometry is assymetrical for these two directions. A thin sheet of ice accumulated on the dewar window over the 2002 season. The window was redesigned to prevent ice buildup in later years. The black curve is based on an observation of Venus made shortly before removing the ice. The blue curve is ice-free. The accumulated ice expanded ACBARs beam size.

were only eight 150 GHz channels in 2002) are coadded into a map with a pixel size of $1'$. One-dimensional cross-sections of these maps through the central pixel are plotted in Figure 3.3. The sidelobes are more distinct in the direction of the chopper motion. Using the channel-averaged maps improves the signal-to-noise and is a valid simplifying assumption, as temperature maps for the power spectrum estimation are also averaged across all channels. The Venus maps are Fourier transformed and binned into narrow frequency bins with $\Delta\ell = 50$ to determine the symmetrized beam function $B(\ell)$. As seen in Figure 3.4, the beam function is poorly fit by a single gaussian function. However, the sum of two gaussian functions fits the experimental beam function very well

$$B(\ell) = (1 - \alpha)B_g^1(\ell) + \alpha B_g^2(\ell).$$

This approximation can be viewed as the sum of a main lobe gaussian function B_g^1 and a sidelobe gaussian function B_g^2. The parameters of the sidelobe, α and $B_g^2(\ell)$, are fixed according to the Venus fits. The average value of these parameters across
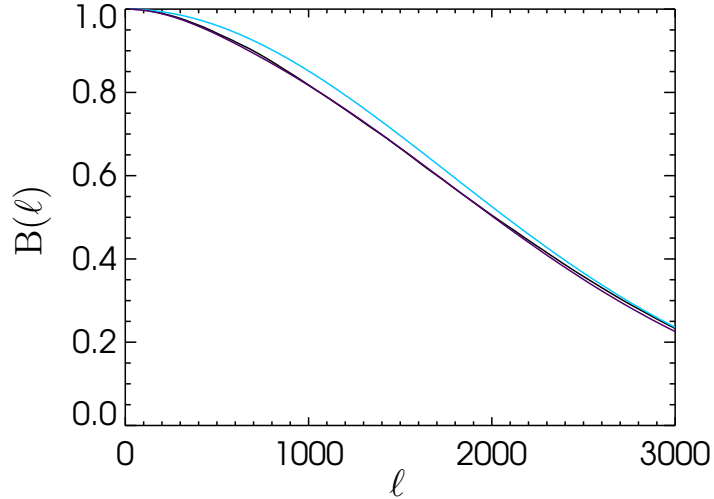
Figure 3.4: ACBARs experimental beam function is plotted in black. The beam function has been measured using radial- and channel-averaged maps of Venus. The results of a single Venus observation are shown here. Neglecting the sidelobe structure and modeling the beam as a single gaussian would produce the turquoise curve. This can introduce biases of up to 5% in the beam function. The beam function is well-approximated to the sub-percent level by the sum of two gaussians (purple curve) $B(\ell) = (1 - \alpha)B_g^1(\ell) + \alpha B_g^2(\ell)$. The FWHM of the first or "main lobe" gaussian is identical to the single gaussian fit ($\sim$4.5'). The relative amplitude $\alpha = 0.0428$ and FWHM=20.267' of the second, "sidelobe" gaussian is fixed to the mean value across all channels in two Venus observations.

all Venus observations is $\alpha = 0.04281$, with a FWHM $= 20.2672'$. The FWHM of the main lobe gaussian is allowed to vary between fields based on the quasar images.

The central quasars and their measured amplitude in the CMB fields are listed in Table 6.3. In fields with multiple point sources, the brightest, isolated source (marked with an asterisk) is used to measure the beam. The data for each channel are coadded into a map with 1' resolution. Large-scale offsets, including the shadowing caused by the polynomial filtering, are removed by doing a joint fit of a gaussian plus quadratic to each row and then subtracting the fit quadratic. The cleaned maps are fit to a two-dimensional gaussian, with the major and minor axes free to rotate in a 30' square map around the quasar. The maximum beam ellipticity $\epsilon = \frac{(FWHM_{major} - FWHM_{minor})}{(FWHM_{major} + FWHM_{minor})}$ is 0.083 for the ACBAR channels. The average beam ellipticity is 0.03. The results are stored and used to parametrize the channel beams for the power spectrum maps.

The large fields, CMB9-12, did not have bright, central quasars with which to estimate the beam main lobe. Instead, the main lobe in these large fields is assumed to be the same as the main lobes measured in 2005 observations of CMB5. While this assumption is imperfect, it should be adequate at low $\ell < 1800$. These large, shallow fields do not contribute to the power spectrum at smaller angular scales due to their high pixel noise and large $6'$ pixel size. The deep fields CMB5 and CMB8 are the most important fields to the high-ℓ results. CMB5 accounts for 77% of the weight in the highest-ℓ bin, while CMB8 accounts for most of the remainder. The additional beam uncertainty for the large fields is not expected to significantly affect the power spectrum results.

The error in the main lobe fit is estimated using a combination of Monte Carlo methods and sub-divisions of the real data. One hundred realizations of the CMB sky are generated for each field. A point source is added at the nominal position of the quasar, and the map is filtered identically to the real data. The fitting code is run on the filtered, fake maps, testing how well the known input beam sizes are recovered. In addition to the Monte Carloes, the observations are divided into subsets, with the beam fit for each subset. The observed variation in the recovered beam size yields a second estimate of the beam uncertainty. The fits are repeated on maps shifted by half a pixel to probe for any systematic effects due to pixelation. For a single field and year, the overall statistical uncertainty proved to be between 1.5% - 4%, with a possible systematic errror of up to 2%. As multiple fields and years are combined into the final power spectrum, the statistical uncertainties are combined according to the relative weights of the field in highest-ℓ bin of the power spectrum. The combined statistical uncertainty is 1.7%, which when combined with the possible systematic error leads to an overall main lobe beam uncertainty of 2.6% for the power spectrum.

The beam function measurement depends on the sidelobes measured in 2002 remaining unchanged in 2005. With 20/20 hindsight, it would have been better to observe a planet in 2005. ACBAR observed RCW38, a bright HII region in the galactic plane, every day. We compare deep, coadded observations of RCW38 to constrain the temporal variability of the beam sidelobes when Venus was unavailable. The

complex structure in the neighborhood of RCW38 (see Fig. 3.6) makes it difficult to recover the beam shape $B(\mathbf{r})$. We sidestep that complication by examining ratios of the beam-smoothed RCW38 maps $\int d^2 r S^{RCW38}(\mathbf{r})B(\mathbf{r})$. Any observed differences in the maps would indicate a change to the instrumental beam function, as RCW38's morphology S^{RCW38} is expected to be constant. The observations of RCW38 are split into two to four periods for each year. About 30 observations pass atmospheric cuts and are coadded in each period. The pixel noise level in the maps is at approximately -32 dB of the peak amplitude of RCW38. The map is Fourier transformed and binned in ℓ to estimate $B_\ell^{eff.RCW38} = F_{\ell\ell'}B_{\ell'} * S^{RCW38}$. Here, $F_{\ell\ell'}$ is the filtering applied to the map. Although care is taken to apply the same filtering to all the maps, residual filtering and atmosphere differences are the dominant source of noise for the method. There is one other complication in comparing in the maps of RCW38. The FWHM of the beam main lobe measured on the quasars changed between 2002 and 2005. This is unsurprising, as there are eight new channels in 2005, and the telescope was refocused. To correct for the changed beam main lobe, the measured $B_\ell^{eff.RCW38}$ for 2005 was multiplied by the ratio $B_\ell^{2002-ML}/B_\ell^{2005-ML}$, where $B_\ell^{200X-ML}$ is the quasar main lobe beam function for that period. The ratio of $B_\ell^{eff.RCW38}$ during the Venus observations to other months set an upper-limit on temporal variations in the beam transfer function as a function of ℓ. Figure 3.5 shows the beam uncertainty used for the final power spectrum. The plotted beam uncertainty includes the uncertainty in sidelobes and the 2.6% uncertainty in measuring the FWHM of the main lobe.

As discussed in [64] and [41], ice building up on the dewar window during the winter of 2002 affected the beam shape. Venus observations immediately before the ice was removed in 2002 have larger sidelobes than are seen in observations made immediately afterwards. Ice buildup was eliminated in 2004 and 2005 by adding a thin mylar sheet in front of the dewar window to create a small air gap vented with dry nitrogen gas. We therefore base our sidelobe model on two Venus observations made in late September 2002, after the ice was chipped off of the dewar window. The sidelobes during 2002 are tricky since we expect them to change at an unknown rate as ice accumulates. Fortunately, the CMB5 observations were made at the beginning

ACBAR Beam Uncertainty
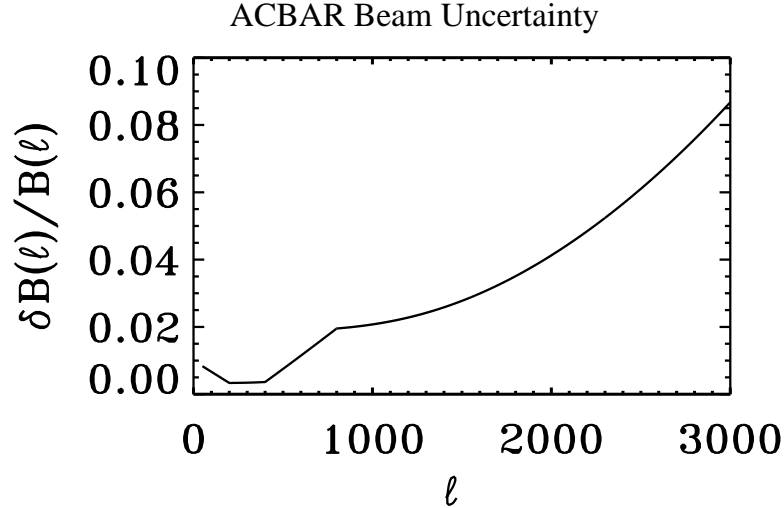
Figure 3.5: The estimated uncertainty in the ACBAR beam function. Above $\ell = 1000$, the error is dominated by the 2.6% uncertainty in the measuring the main lobe's FWHM on bright quasar's in the CMB fields. Below $\ell = 1000$, the uncertainty is dominated by the reliability of extending the Venus sidelobe model to the CMB observations. The uncertainty is minimized around $\ell \sim 350$, as the absolute calibration is measured on those angular scales.

of the 2002 season when relatively little ice had accumulated on the window and the no-ice sidelobe model proved adequate for that period. The RCW38 tests described above should capture the effects of ice on the beam function.

The chopping mirror moves the beam's position on the secondary mirror as well as slightly on the primary mirror, which can modulate the beam shape on the sky. The effects are larger for pixels at the edge of the focal plane. To characterize this effect, we made maps of RCW38 centered at various chopper positions several times each year during periods of good weather. These observations are time-consuming, requiring the better part of a day of observation. A channel's beam at each chopper position is parameterized with a gaussian fit which is used to calculate the beam solid angle. Variations in the beam solid angle will affect the CMB window function. The solid angle is found to have a linear dependence on chopper position in each year, parameterized as $\Omega = \Omega_0[1 + (V_{chopper}) * A_{channel}]$, where Ω_0 is the measured solid angle for $V_{chopper} = 0$. On average, the beam solid angle varies by ~10% across a full

± 10V chopper sweep in 2005.

3.4   Calibration

The ACBAR calibration can be divided into three distinct steps based on the timescales involved. On the shortest timescales, the daily calibration brings each observation in a single season to a common level. The power spectrum uses data from multiple years; the second calibration step ties multiple years together. Finally, this "ACBAR" temperature scale must be converted to a true, absolute temperature scale in order to compare the ACBAR power spectrum to theory and results from other experiments. Each of these steps will be discussed below, with special attention paid to the absolute calibration.

The absolute calibration for the first ACBAR data release was obtained by observations of Venus and Mars, as detailed in [64, 65]. We explored alternative calibration methods in order to improve upon the 10% temperature calibration error of the planetary calibration. A precise calibration between low-ℓ and high-ℓ experimental data dramatically strengthens the combined data set's ability to constrain cosmological parameters. For instance, calibration uncertainty can hide the tilt in the power spectrum caused by a running spectral index. Two calibration schemes were successfully developed for later data releases. The RCW38-based calibration for 2002 reduced the temperature calibration error to 6% in [42]. The 2005 calibration based on a comparison of CMB temperature anisotropies with WMAP3 has an error of 2.2%. At this level, the calibration uncertainty is comparable to the beam uncertainty.

3.4.1   Day-to-day Calibration

The calibration depends on several factors such as the atmospheric opacity, optical loading, detector responsivity, and snow accumulation on the mirrors, which may vary over the course of a day. ACBAR's treatment of these factors is summarized here for reference; a more detailed description can be found in [64, 65].

RCW38 is a bright, compact HII region which fulfills multiple roles in the ACBAR analysis including the daily calibration. At $-47.533°$, RCW38 is at a similar elevation to the CMB fields, which are centered at declinations between $-64°$ and $-46°$. RCW38 was typically observed 1-2 times each day in between CMB observations. For the calibration, each RCW38 observation is binned into single-channel maps with 1' pixels. The chopper-synchronous offsets are removed by subtracting a second-order polynomial first from constant-elevation strips and then in the perpendicular direction from constant chopper-voltage strips. The area within an 8' radius of RCW38 is masked and ignored for these polynomial fits. The ratio of the measured integrated voltage within 8' of RCW38 to the known flux of RCW38 yields a voltage-to-Kelvin calibration. Small corrections are applied for the changes in atmospheric opacity and bolometer responsivity between observations. The voltage-to-Kelvin calibrations for the RCW38 observations are carried over to the CMB observations using a linear interpolation. If the CMB observation occurs at time t_{CMB} in between two RCW38 observations at $t = 0$ with a calibration of $V/K = R_0$ and at $t = T$ with a calibration of $V/K = R_1$, respectively, then the CMB observation is calibrated by $V/K = R_0(1 - t_{CMB}/T) + R_1(t_{CMB}/T)$. The assumption of linearity might fail if changes are abrupt rather than gradual. For instance, a storm might deposit a sudden flurry of snow on the mirrors, or the winterover might sweep snow off the mirrors. We impose an upper limit on the possible fluctuations by discarding CMB observations if the calibration ratio changed by more than 10% between the immediately adjacent RCW38 observations. The low residual variability is an acceptable calibration error that should average down to insignificant levels over the hundreds of CMB observations.

The atmospheric opacity τ is necessary to convert the RCW38 calibration from the elevation of RCW38 to the elevation of the CMB fields and also to correct for changes in τ over time. The opacity can be calculated using a 'skydip', in which the atmospheric loading is measured at a number of elevations and fit to $P = P_0 e^{-\tau/cos(\theta)}$ to solve for τ. This is a time-intensive procedure that ACBAR only performs a few times per day. Instead, ACBAR depends on the opacity measurements made every 15

minutes by the 350 μm tipper experiment mounted on the nearby AST/RO building [58]. A linear relation is observed between the 350 μm and 150 GHz atmospheric opacities under typical atmospheric conditions. The relationship breaks down at high-τ; such data is discarded without loss since it corresponds to terrible weather. The "Tipper unusable" entry in Table 4.1 includes data cut for this reason and also for the rare periods when the tipper data was unavailable.

A single calibration K/V number is calculated for each channel and observation. Each observation can take 4 to 12 hours. Most events that change the calibration will also change the optical loading and DC level of the bolometers. Observations with >2% variations in the DC levels are flagged and excluded from the analysis (listed in Table 4.1). The residual calibration fluctuations about the mean within each observation are expected to average down to sub-percent levels over the course of a season.

3.4.2 Revised 2002 Calibration

3.4.2.1 Map-based Calibration

Before settling on the RCW38-based calibration used in K07, we had planned to calibrate the second ACBAR data release with a cross-calibration to Boomerang via the CMB temperature anisotropies. The CMB4 field observed in 2002 has overlapping coverage with both B98 and B03. The calibration scheme was fundamentally different than what is detailed below for the 2005 spherical harmonic calibration algorithm (§3.4.3.1). A pixel-to-pixel comparison of the maps from each experiment would be used to establish the relative calibration. The map-based comparison proved very sensitive to details of the noise, pixel binning, beams, and pointing. Monte Carlo simulations were used extensively to understand the subtleties of the method. This is an abbreviated list of the the issues we investigated, many of which are general to any CMB-based calibration scheme:

- Beam differences;

- Beam uncertainty;

- Filtering differences;

- Pointing shifts;

- Pixel schemes (best to use the same one);

- Mode-mixing due to partial sky coverage (masking);

- Noise bias (notably correlated noise causes trouble);

- Diffuse foregrounds & point sources (which have a different frequency dependence than CMB).

The effects of some of these items are self-evident. Clearly, the beam shape and filtering will change the signal in a map. The importance of the pixelation scheme is less obvious. The original implementation of the map calibration scheme converted Boomerang's Healpix maps to ACBAR's flat-sky maps with similarly-sized pixels. It ran afoul of large-scale correlations in the offsets between the Healpix and flat-sky pixel centers. The issue can be avoided by explicitly taking a weighted average based on the fraction of an input pixel's area which lies within the output pixel. A simpler solution used in the WMAP calibration is to sidestep the issue by using the same pixel scheme for both maps. It is important to handle each of these issues for the calibration.

Although the low signal-to-noise in the CMB2(CMB4) map made it difficult to disentangle the effects, we eventually solved most of the issues for the map-based calibration. One outstanding issue remained: the pointing consistency between Boomerang and ACBAR. In particular, we worried that the maps lacked adequate signal-to-noise to detect small pointing offsets that might significantly bias the calibration. Although no offset was detected between the CMB4 map for 2002 and the Boomerang maps, we did detect an offset when we examined the much deeper 2004 observations covering part of the B03 deep field. The pointing difference was not a simple offset but a

function of declination. We fit it to an empirical model

$$RA' = RA + 0.0393 - 0.0171(Dec + 46.5806)$$

$$Dec' = Dec - 0.0267,$$

where RA and Dec are in degrees and found offsets of up to $7'$ across the field. The declination of -46.5806° in the equation is the declination of a bright point source in the map, PMN J0538-4405. QUaD, a CMB polarization experiment at the South Pole, observed the same area of sky and found a similar pointing offset to B03 [21]. These offsets are a fraction of the B03 beam size. The error is probably in the Boomerang pointing model and may be more complicated than the simple model above. The pointing issues led us to abandon the map-based calibration to Boomerang in favor of the simpler RCW38-based calibration detailed below, and encouraged us to use WMAP3 to calibrate the 2005 maps.

3.4.2.2 RCW38-based Calibration

RCW38 is a compact HII region in the Galactic plane at a declination similar to the ACBAR CMB fields. It has a large and stable flux and served as the primary calibrator for the second ACBAR data release. We determine the absolute flux of RCW38 using maps from the 2003 flight of BOOMERANG ([49], B03), which are calibrated relative to the WMAP experiment with an absolute uncertainty of 1.8%. RCW38 does not have a black-body spectrum, requiring spectral corrections for the calibration of CMB anisotropies. However, the similarity in the spectral responses of the 150 GHz bands in the B03 and ACBAR experiments ensures these corrections will be small.

ACBAR made daily high signal-to-noise maps of the galactic source RCW38. B03 also mapped portions of the galactic plane including RCW38 (Fig. 3.6), allowing a direct comparison of the high signal-to-noise maps made by the two experiments. The experiments have different scan patterns, beam widths, and spatial filters that can affect the measured flux. We resample the B03 map using pointing information for
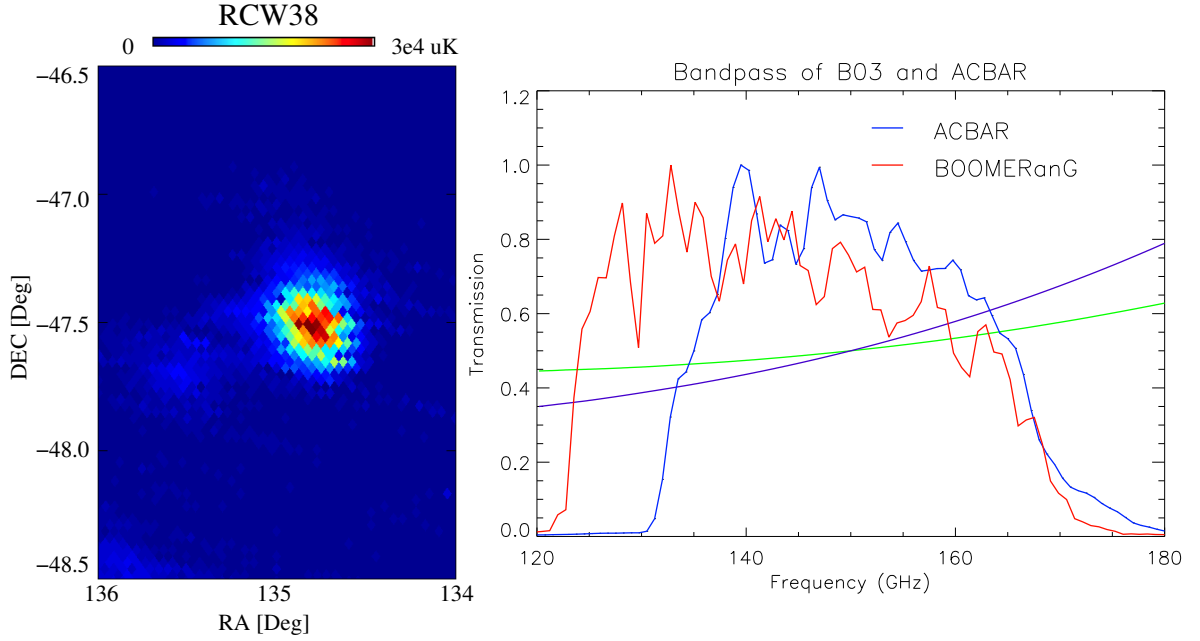
Figure 3.6: On the **left-hand side** is a map of RCW38 made by B03. The band-passes for each experiment measured by Fourier transform spectroscopy are shown on the **right**. The range of possible spectra (1σ) for RCW38 is also shown, with each spectrum being normalized to 0.50 at 150 GHz. (green and violet lines).

Source	Value	Uncertainty (%)
Ratio of B03 over ACBAR	1.060	-
Statistical error		0.53
Residual chopper synchronous offsets		0.1
B03 Instrumental noise		0.3
Variability during 2002		2.0
Transfer function:	1.056	-
Statistical error		0.17
Uncertainty in the signal model		3.0
Dependence upon the radius of integration		1.5
Beam uncertainty		1.35
Spectral Correction	1.008	-
RCW38's spectrum and experimental bandpasses		2.1
Spectrum of extended structure		3.0
B03's Absolute Calibration through WMAP		1.8
Overall	1.128	5.84%

Table 3.2: Error budget for the RCW38-based ACBAR calibration. The calibration of ACBAR through RCW38 has multiple factors and potential sources of error, tabulated here for reference. The dominant calibration uncertainties are due to un-certainties in the emission spectrum of RCW38 and the morphology and spectrum of the extended galactic structure.

each ACBAR observation to generate an ACBAR-equivalent B03 observation. The ACBAR maps are smoothed to simulate the effect of Boomerang's larger beam. Large spatial modes in both experiments are corrupted; in ACBAR by chopper-synchronous offsets and in B03 by the high-pass filter. We simultaneously fit a quadratic offset and Gaussian source model from each scan of the ACBAR and B03 maps which removes these modes without affecting the amplitude of a point source. After coadding the channel maps, we integrate the flux within a $18'$ radius of the source. The integrated flux is robust to small misestimates or changes in the effective beam size (including any smearing due to pointing jitter). The measured flux ratio and the associated uncertainties are listed under *Ratio of B03 over ACBAR* in Table 3.4.

We use Monte Carlo techniques to estimate the transfer function of this method. Using a model of RCW38 and its surroundings, we generate simulated timestreams for the observations with each experiment. Maps are created from the timestreams and are filtered as described above. The ratio of the transfer functions is found to be $ACBAR/B03 = 1.056 \pm 0.002$. We have tested the dependence of the transfer function on the assumed signal template and include a 3% uncertainty in our calibration due to this effect. This technique is readily adapted to include the effect of the beam uncertainty for each experiment, and we find that the beam contributes 1.35% to our estimated uncertainty. The effective beam used for each experiment includes smearing due to pointing errors. As the listed B03 beams are for the CMB field and the pointing uncertainty in the vicinity of RCW38 may be slightly different, we have doubled the B03 beam uncertainty to be conservative. The effect of the transfer function and the associated uncertainty are listed under *Transfer Function* in Table 3.4.

RCW38 has a much different spectrum than the CMB, and the effective CMB temperature difference it produces depends on the photon-frequency. The calibration described here is based on observations with ACBAR's 150 GHz channels and Boomerang's 145 GHz channels, which have similar bandpasses (Fig. 3.6). We account for the small difference in bandpass by convolving the measured spectral response of each experiment with a model of RCW38's spectrum from [49]. If two maps

nominally calibrated in CMB temperature units are integrated about RCW38, the true calibration factor **K** will depend on the measured flux ratio I_{B03}/I_{ACBAR}, the bandpass of each experiment t_ν, the spectrum of RCW38 S_ν^{RCW38} and the known blackbody spectrum of the CMB $\frac{dB_\nu}{dT}|_{T_{CMB}}$:

$$K = \frac{I_{B03}}{I_{ACBAR}} * R$$

,

$$\text{where } R = \frac{\int t_\nu^{ACBAR}\lambda^2 S_\nu^{RCW38}d\nu}{\int t_\nu^{B03}\lambda^2 S_\nu^{RCW38}d\nu} \frac{\int t_\nu^{B03}\lambda^2 \frac{dB_\nu}{dT}|_{T_{CMB}}d\nu}{\int t_\nu^{ACBAR}\lambda^2 \frac{dB_\nu}{dT}|_{T_{CMB}}d\nu}.$$

This factor R includes the full dependence of the calibration on RCW38's spectrum and the bandpasses of each experiment. The dominant source of uncertainty is RCW38's spectrum; to be conservative, we double the estimates listed in [49]. The model consists of two components: a power law term with $\alpha = 0.5 \pm 0.2$ and a dust term with $T_{dust} = 22.4 \pm 1.8\,\text{K}$. Only the relative amplitude of the two terms is important: $A_{power\ law\ @\ 30\,GHz}/A_{dust\ peak} = 867 \pm 400$. We also include the uncertainty in the laboratory measurement of each experiment's bandpass. The mean value and uncertainty in R is estimated using 100,000 realizations of the above parameters, and found to be 1.008 ± 0.021 (See *Spectral Correction* in Table 3.4.) Given that our integration radius is larger then RCW38's size, the flux contribution of diffuse emission near RCW38 can be significant. The spectrum of this extended structure may be different from that of RCW38, in which case the calibration ratio would depend on the integration radius. We estimate this uncertainty from the observed variability of the calibration ratio with integration distance.

The calibration value from the real map is normalized by the spectral correction for RCW38 and the signal-only transfer functions estimated for each experiment. The result of this analysis is that the temperature scale for ACBAR's CMB fields in 2002 should be multiplied by 1.128 ± 0.066 relative to the planet-based calibration given in [65]. Table 3.4 tabulates the contributing factors and error budget.

3.4.3 Calibration of the Full ACBAR Dataset

We derive the absolute calibration of ACBAR by directly comparing the 2005 ACBAR maps to the WMAP3 V and W-band temperature maps [28]. We pass the WMAP3 maps through a simulated version of the ACBAR pipeline to ensure equal filtering. Cross-spectra are calculated for each field. The ratios of the cross-spectra are used to measure the relative calibration after being corrected for the respective instrumental beam functions. Results for ACBAR's six largest fields (approximately 600 deg^2 in area and marked with a * in Table 3.1) are combined to achieve an accuracy of 2.17%. For the power spectrum analysis, the CMB13 field is truncated to avoid overlapping CMB5 (as shown in Figure 3.2). The calibration uses the complete coverage of CMB13, encompassing the areas marked as CMB5 and CMB13. Additional details of this procedure are discussed in the next section.

The 2005 calibration is transfered to 2001 and 2002 via power spectra for overlapping regions observed by ACBAR in each year. The CMB5 field is used to extend the calibration of the 2005 season to the 2002 data. The CMB5 calibration is carried to other fields observed in 2002 by daily observations of the flux of RCW38. The calibration of the CMB4 field (observed in 2002) then is transfered to the 70% overlapping CMB2 field (observed in 2001). We determine the corrections to RCW38-based calibration for the 2002 data in K07 to be 0.973 ± 0.032. Including the year-to-year calibration uncertainty, the final calibration has an uncertainty of 2.23% in CMB temperature units (4.5% in power). Table 3.4 has detailed accounting of calibration uncertainty.

3.4.3.1 WMAP-ACBAR 2005 Calibration

Calibrating with the CMB temperature anisotropies has two main advantages. The first is that the calibration of the WMAP temperature maps (at 0.5% in temperature) is an order of magnitude more precise than the flux calibration of the calibration sources ACBAR used in previous releases. The second advantage is that by construction, the anisotropies have the same spectrum as what is being calibrated, rendering

the large frequency gap between WMAP and ACBAR irrelevant.

The two experiments have different scan patterns, noise, beam widths, and spatial filters that will effect the measured flux. In this analysis, we assume that the WMAP3 maps are effectively unfiltered except for instrumental beam function. The two maps can then be represented as:

$$S_i^{WMAP} = \int T(x)B_{WMAP}(x_i - x)dx + N_i^{WMAP}$$

$$S_i^{ACBAR} = F_{ij}\int T(x)B_{ACBAR}(x_j - x)dx + N_i^{ACBAR},$$

where T is the underlying CMB signal, N is the instrumental noise, B is the beam function, and F_{ij} is the ACBAR filter matrix as defined in Section 4.1. We reduce the filtering differences by resampling the WMAP map using the ACBAR pointing information and applying the ACBAR spatial filtering to generate an 'ACBAR-filtered' WMAP map:

$$S_i^{WMAP-equivalent} = F_{ij}(\int T(x)B_{WMAP}(x_j - x)dx + N_i^{WMAP}).$$

An example of this process when applied to the B03 map is shown in Figure 3.7. We choose to do the absolute calibration via cross-power spectra rather than a direct pixel-to-pixel comparison of the maps. Using cross-spectra significantly reduces the impact of the noise model on the result. The significant beam differences between the experiments are more naturally dealt with in multipole space than in pixel space. We construct the ratio from the filtered maps:

$$R = \Re(\langle \frac{a_{\ell m}^{WMAP-X*} * a_{\ell m}^{ACBAR-Z}}{a_{\ell m}^{ACBAR-Y*} * a_{\ell m}^{ACBAR-Z}(B_\ell^{WMAP-X}/B_\ell^{ACBAR})}\rangle),$$

where X can denote either the V- or W-band map for WMAP and Y/Z marks either of two noise-independent ACBAR combinations. There is a narrow ℓ-range from 256-512 useful for calibration. The range is limited at high-ℓ by the rapidly falling WMAP beam function and at low-ℓ by the ACBAR polynomial filtering, which acts
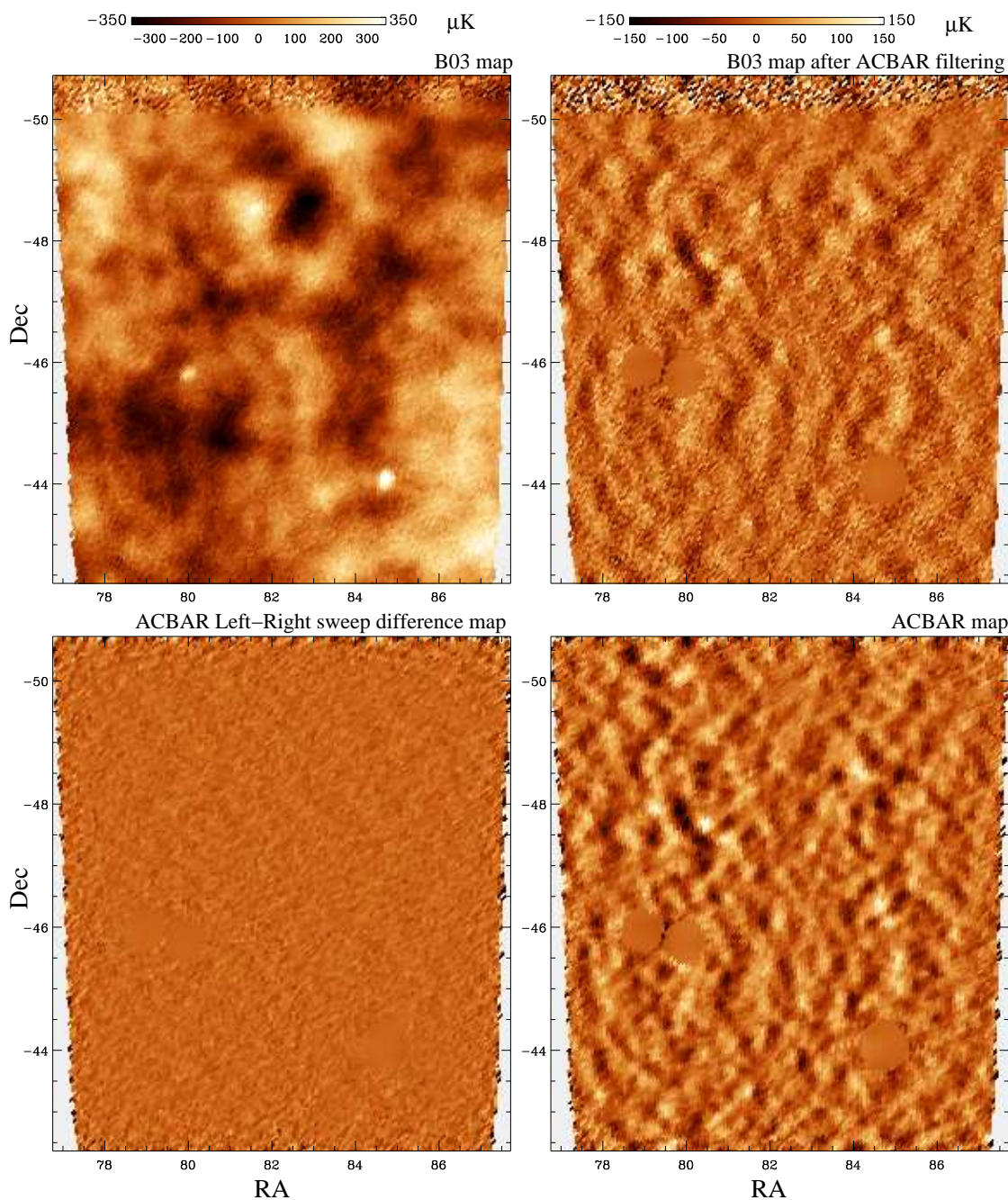
Figure 3.7: A comparison of observations of the CMB8 field made with B03 and ACBAR. This field lies in the deep region of the B03 map. The top two maps are from B03. The bottom two maps are from ACBAR. In the *top left* panel, the B03 map of the CMB8 field. The dynamic range of this map is greater than that of the other three figures. The increased noise at one edge marks the edge of the B03 deep coverage. The ACBAR filtering is applied to the B03 map to create the map in the *top right* panel. Directly below it in the *bottom right* panel is the ACBAR map of same region. Note the clear correspondence between the CMB anisotropies observed by B03 and ACBAR. Three bright point sources have been masked. An ACBAR left-right sweep difference map is shown in the *bottom left* panel. The power spectrum of this map (and the other 9 fields) is plotted in Fig. 5.4.

Foreground	Frequency	$RMS_{foreground}/RMS_{CMB}$
Dust	62 GHz	0.1e-2
Dust	91 GHz	0.4e-2
Dust	150 GHz	1.5e-2
Free-free	62 GHz	1.9e-3
Free-free	91 GHz	0.9e-3
Free-free	150 GHz	0.03e-3
Synchrotron	62 GHz	3.6e-4
Synchrotron	91 GHz	1.6e-4
Synchrotron	150 GHz	0.8e-4

Table 3.3: Average ratio of the RMS foreground signal to RMS CMB signal in our six calibration fields for each frequency band. The foreground levels in these fields are well below the all-sky averages. Dust emission is expected to be the most significant contaminant in these fields; however, a set of simulations found that any dust bias would be more than order of magnitude smaller than other sources of error in the calibration. We conclude that ACBARs calibration is not biased by the presence of foregrounds.

as a high-pass filter. We choose to use the WMAP V & W bands to take advantage of their smaller beam size.

Monte Carlo simulations are used to determine the transfer function of this estimator. We generate CMB sky simulations convolved with the respective instrumental beam functions using the Healpix[1] library. We resample each realization and apply the ACBAR filtering matrix described above to generate equivalent maps for each field. We expected and found a small intrinsic bias, as the beam convolution and filtering operations do not commute: $B^{ACBAR} * F_{ij}B^{WMAP} \neq B^{WMAP} * F_{ij}B^{ACBAR}$. We correct the real data by the ℓ-dependent transfer function measured in the simulations. The technique is easily adapted to estimate the error caused by pointing uncertainties and to confirm that the estimator is unbiased with the inclusion of noise. The derived error in the transfer function is listed in Table 3.4.

Foreground sources have the potential to systematically bias a calibration bridging 60 to 150 GHz. Radio sources, synchrotron emission, dust, and free-free emission all have a distinctly different spectral dependence than the CMB that could lead to a

---

[1]http://healpix.jpl.nasa.gov

Source	Uncertainty (%)
Statistical Error in the Calibration ratio	1.32
ℓ dependence of the Calibration ratio	1.1
Statistical Error in the Transfer Function of the Calibration ratio	0.35
Uncertainty in the WMAP B_ℓ	0.5
Relative pointing uncertainty	1.0
Uncertainty in the Year-to-year ACBAR calibration	0.3
Uncertainty in the Transfer Function for the Power Spectrum	0.5
Contamination from foregrounds	0.2
WMAP3's Absolute Calibration	0.5
Overall	2.23%

Table 3.4: The calibration of ACBAR using the WMAP3 temperature maps has multiple potential sources of error, tabulated here for reference. The dominant calibration uncertainties are due to tied to noise in the WMAP maps at the angular scales used for calibration. The uncertainty in the ACBAR beam function is comparable to the calibration uncertainty.

calibration bias. This risk is ameliorated by the positioning of the ACBAR fields in regions of exceptionally low foregrounds. Radio sources are masked and excluded from the calibration. We use the MEM foreground models in Hinshaw et al. [28] to estimate the RMS fluctuations of each foreground relative to the CMB fluctuations (see Table 3.3) and find that the free-free and synchrotron fluctuations are less than 0.1% of the CMB fluctuations in all frequency bands, while dust emission can reach 1.5% of CMB fluctuations in the 150 GHz maps. We test the effects of the most significant foreground, dust, by adding the FDS99 dust model [20] to a set of CMB realizations. The resultant maps are passed through a simulated pipeline as outlined in the previous paragraph. We find that the addition of dust does not introduce a detectable bias with an uncertainty of 0.2%.

We perform a weighted average of the measured calibration ratio across all ℓ-bin, field and band combinations after correcting for the estimated signal-only transfer functions. We estimate the calibration error to be 2.23%. Table 3.4 tabulates the contributing factors and error budget. We now proceed to propagate this $a_{\ell m}$-based calibration to the CMB observations done in 2001 and 2002.

3.4.3.2   ACBAR 2001-2002 and 2002-2005 Cross Calibrations

We carry the 2005 calibration into 2001 and 2002 by comparing the 2001 observations of the CMB2 field to the overlapping 2002 CMB4 field, and the 2002 observations of the CMB5 field to the 2005 observations of the CMB5 field. A power spectrum is calculated for each overlapping region, and the ratio of the bandpowers is used to derive a cross calibration. The procedures used are outlined in more detail in K07. We use the same relative calibration for 2001 as K07: $T_{2001}/T_{2002} = 1.238 \pm 0.067$. We find cross-calibration factor for 2002 to be $T_{2005}/T_{2002} = 1.035 \pm 0.025$. We apply these corrections to the data and determine the overall calibration uncertainty to be 2.23% (in temperature units) based primarily on the uncertainties associated with WMAP/ACBAR-2005 cross calibration.

3.5   Sensitivity

A number of uncorrelated sources contribute to a bolometer's noise and have been modeled in the literature [51, 24, 73]

$$NEP^2 = (NEP^2_{Johnson} + NEP^2_{phonon} + NEP^2_{photon}) + (NEP^2_{load} + NEP^2_{amplifier}).$$

The first three terms are intrinsic to the bolometer, while the last two terms originate in the read-out circuit (see Figure A). We have neglected the noise from atmospheric fluctuations, which is important at low frequencies. The amplifier noise must be measured, but the other terms can be calculated from the physical model of a bolometer. Actual values of these NEPs for ACBAR under good observing conditions are listed in Table 3.5, along with other bolometer parameters and the realized ACBAR sensitivities.

Johnson noise is caused by the thermal excitations of charge carriers and is universal to all resistors. The voltage noise in the load resistors will show up as current

noise across the bolometer, so the two load resistors in the circuit will contribute

$$NEV_{load}^2 = 4k_bT_{bath}/R_L \left(\frac{(R_Lz)}{R_L + z} \right)^2,$$

where T_{bath} is the focal plane temperature and R_l is the total load resistance ($R_L = 60$ MΩ for ACBAR). In a bolometer, the Johnson noise is suppressed by electrothermal feedback and is reduced to

$$NEV_{Johnson}^2 = k_bT\frac{(R + z)^2}{R},$$

where z is the dynamic impedance of the bolometer, T is the bolometer temperature and R is the bolometer resistance. This expression reduces to the standard Johnson noise level of $NEV^2 = 4k_bTR$ if the bias current is set to zero. These NEVs can be converted to NEPs using the bolometer responsitivity $S \equiv \frac{\delta V_s}{\delta P}$ as $NEP^2 = NEV^2/|S|^2$. An expression for the bolometer responsivity and dynamic impedance can be found in Appendix A.

Phonon noise is caused by random energy flows into and out of the detectors at the microscopic level. Electrons, phonons, or other energy carriers have some finite mean free path which leads to temperature fluctuations at the detector. For an isothermal object, the noise power can be shown to be $NEP_{phonon}^2 = 4k_bG_dT^2$. Real bolometers have a continuous temperature drop along the thermal link from the bolometer to the bath leading to

$$NEP_{phonon}^2 = 4k_bG_dT^2\gamma,$$

where G_d is the dynamic G of the bolometer and $\gamma = \frac{(\beta+1)}{(2\beta+3)} \frac{(1-(T_{bath}/T)^{(2\beta+3)})}{(1-(T_{bath}/T)^{(\beta+1)})}$ is a correction factor between 0 and 1 for the temperature variation along the thermal link.

3.5.1 Photon Noise

Bolometers act like photon number counters with an integration time set by the bolometer time constant. As such, the statistical distribution of photons is a fun-

150 GHz Channels	All	Old	New
$\Delta\nu$ (GHz)	30	30	30
η (%)	0.42	0.38	0.45
FWHM (')	4.7	4.7	4.7
Q_{total} (pW)	12.8	11.8	13.3
T_{RJ} (K)	29	31	28
R (MΩ)	6.7	7.8	5.6
T_{bolo} (mK)	351	352	350
G(T) (pW/K)	434	458	411
S ($\times 10^8$ V/W)	-2.4	-2.5	-2.2
NEP_γ ($\times 10^{17}$ $W/\sqrt{Hz}$)	7.8	7.6	8.0
NEP_J ($\times 10^{17}$ $W/\sqrt{Hz}$)	2.3	2.2	2.3
NEP_G ($\times 10^{17}$ $W/\sqrt{Hz}$)	4.2	4.4	4.1
NEP_{load} ($\times 10^{17}$ $W/\sqrt{Hz}$)	0.1	0.1	0.0
NEP_A ($\times 10^{17}$ $W/\sqrt{Hz}$)	1.2	1.2	1.3
NEP_{total} ($\times 10^{17}$ $W/\sqrt{Hz}$)	9.3	9.1	9.4
$NEP_{achieved}$ ($\times 10^{17}$ $W/\sqrt{Hz}$)	8.9	8.7	9.1
NET_{RJ} ($\mu K\sqrt{s}$)	213	231	193
$NEFD$ ($mJy\sqrt{s}$)	316	339	291
NET_{CMB} ($\mu K\sqrt{s}$)	375	404	343
NET_{CMB} ($\mu K\sqrt{s}$)	354	QUaD	
NET_{CMB} ($\mu K\sqrt{s}$)	297	BICEP	

Table 3.5: A listing of typical bolometer properties and noise performance for the 2005 season. The parameters are listed for the average over all 16 detectors, as well as the average over the original eight 150 GHz detectors and the eight new 150 GHz detectors. The performance of the two sets is similar. The bolometer parameters are taken from load curves measured at EL=60° on 6/6/2005. The actual noise properties are derived from the PSD of the timestreams for a CMB5 observation on the same day. The quoted $NEP_{achieved}$ is the average of the time constant corrected PSD between 5 and 15 Hz divided by the responsivity, S. Figure 2.10 plots an uncorrected PSD for this CMB observation. The bolometer noise model agrees well with the realized noise for ACBAR. The JFET and amplifier noise power is scaled from an estimate of the amplifier voltage noise at 10 Hz, $3 \times 10^{-9} V/\sqrt{Hz}$[64]. The 1/f noise due to the atmosphere and JFETs is not modeled. For comparison, the NET per feed of two other bolometer experiments currently observing from the South Pole at 150 GHz are also listed [39]. QUaD and BICEP are polarization experiments. BICEP has no warm optics and lower optical loading, which likely accounts for some of the improvement. The optical loading from ACBAR's optics is listed in Table 3.6.

damental noise floor. The detailed theory of photon fluctuations was first developed by Hanbury Brown and Twiss [8, 9, 10] for a two-photomultiplier interferometry experiment in the 1950s. A number of authors have built upon that work since then. In particular, Lamarre [45] and the Appendix B of [34] are recommended for a more thorough discussion of the subject.

Photons follow Bose-Einstein statistics so the occupancy number of a state is

$$n(\nu, T) = \frac{1}{e^{\left(\frac{h\nu}{k_b T}\right)} - 1}. \tag{3.1}$$

The variance in the number of photons arriving in some time interval can be written as

$$\delta \bar{N}^2 = \bar{N} + \frac{\bar{N}^2}{g}, \tag{3.2}$$

where $\bar{N}$ is the mean number of photons and $g >> 1$ is volume of phase space the photons occupy. The first term is the standard variance for a Poisson distribution, while the second term is caused by the preference of bosons to share the same state and is often referred to as the "Bose term." The fluctuations in the observed power on the bolometer will be

$$\delta \bar{W}^2 = (h\nu)^2 \delta \bar{N}^2 = (h\nu)^2 \bar{N} \left(1 + \frac{\bar{N}^2}{g}\right). \tag{3.3}$$

The mean number of photons can be calculated from the optical loading using $Q = (h\nu)\bar{N}$.

[45] derives the following expression for the optical noise power:

$$NEP^2_{photon} = 2 \int h\nu Q_\nu d\nu + 2 \int \Delta(\nu) Q_\nu^2 d\nu. \tag{3.4}$$

The spectral power of the optical loading on the detector will be the product of the optical efficiency ζ_ν and incoming flux P_ν, $Q_\nu = \zeta_\nu P_\nu$. The factor of two comes from the two photon polarizations. The first term corresponds to the Poisson fluctuations

and can be approximated straightforwardly as

$$NEP^2_{photon,Poisson} \equiv 2 \int h\nu Q_\nu d\nu = 2h\nu_0 Q,$$

where ν_0 is the central frequency of the optical band-pass. The second, Bose term hides a wealth of complications in the factor $\Delta(\nu)$, which is defined in Eq. 10 of [45] by a double integral over both the source and detector intensities. This integral has not been calculated for ACBAR, as it is unnecessary for the interpretation of the CMB results and would require a more detailed knowledge of the sources of ACBAR loading than presently exists. The value of $\Delta(\nu)$ is bounded between 1 (for a point source) and 0 (for a source spatially coherent on large scales). ACBAR's realized noise properties are consistent with this range.

A number of approximations to the Bose term exist for practical applications. The estimate of NEP^2_{photon} presented here follows Appendix B of [34]. In this toy model, the loading is assumed to originate at a single source with constant Q_ν and an emissivity of unity. The effective temperature will then be $T_{RJ} = Q/(\zeta k_b \delta\nu)$.

$$NEP^2_{photon} = 2h\nu_0 Q \left(1 + \zeta n(\nu_0, T_{RJ})\right) \tag{3.5}$$

The second term, $\zeta n(\nu_0, T_{RJ})$, is the photon occupancy number of the emitted flux times the detector's optical efficiency. The occupancy fraction is defined as the number of photons per state and is an analogue to $\frac{\bar{N}}{g}$. The photon noise in Table tab:noisebudget is calculated from Eq. 3.5.1.

The predictions from the ACBAR noise model presented here are slightly (5%) higher than the observed NEPs. This is likely related to the approximations involved in calculating the Bose term. While physically unrealistic, the emissivity assumption will not change the result [41]. However, the assumption of a constant Q_ν and a single, isothermal source have the potential to modify the predictions. ACBAR optical band-pass is an imperfect square function (see Figure fig:bandpass). ACBAR's actual optical background is dominated by loading from the atmosphere and telescope

150 GHz Optical Loading	T_{RJ}
Atmosphere+CMB	10 K
Mirrors+Baffles	9 K
Internal	10 K
Total	29 K

Table 3.6: A breakdown of the contributing sources of optical loading for the 2005 season. The breakdown is based on the measured loading of $\langle T_{RJ} \rangle = 29\ K$ in load curves taken on 6/6/2005. The estimated loading due to the emissivity of the telescope mirrors and baffles is 4 K and 5 K, respectively [64]. The atmospheric loading is estimated by $T_{atm}(1 - e^{-\tau/cos(\theta)})$ and found to be 10K. The CMB's small contribution of 0.6 K has been included in this number. There are periods with higher atmospheric loading. The internal loading of the ACBAR dewar accounts for the remainder and is consistent with expectations from the loading tests conducted before mounting the dewar on the telescope.

mirrors, all sources at ~240K (see Table 3.6). However, about a third of the loading comes from inside the dewar at temperatures between 4K and 77K. The combination of these two factors are believed to explain the over-estimate in the noise model.

3.6 Bolometer Time Constants

The bolometer time constants are measured in situ on the telescope every day. A small calibrator source is visible through a small hole drilled in the tertiary mirror (see §2.5). When in use, the source is heated to $+10°$ over ambient. This produces an acceptable signal-to-noise without significantly increasing the optical loading and possibly changing the bolometer time constant. The frequency of the chopping wheel is varied in 10 Hz increments from 5 Hz to 150 Hz, and the amplitude of bolometer's response measured at each frequency. In retrospect, additional points in the signal band between 1 and 15 Hz would have improved the accuracy of the transfer function reconstruction. The results are well-fit by a single-pole bolometer time constant model. The time constants for 2002, 2004, and 2005 are listed in Table 3.7. The time constants of some bolometers slow down between years; this is believed to be due to the webs picking up dust or other microdebris when the dewar was opened or while stored at ambient pressure in 2003. The dust would add heat capacity to the webs

Channel	τ_{2002} (ms)	τ_{2004} (ms)	τ_{2005} (ms)
A5	-	-	3.65
A3	-	-	1.51
A6	-	-	2.34
A4	-	-	3.27
D3	7.94	7.94	7.94
D4	2.35	2.35	2.37
D6	5.24	5.66	5.66
D5	2.20	2.20	2.28
B6	3.40	3.58	3.58
B3	2.23	2.23	2.23
B2	2.02	2.02	2.03
B1	4.62	6.69	6.69
C1	-	-	1.76
C2	-	-	1.68
C3	-	-	3.40
C4	-	-	3.95

Table 3.7: Measured bolometer time constants under observing conditions on the Viper telescope. Only 150 GHz detectors are listed. The time constants changes for some detectors between 2002 and 2004 are hypothesized to be due to dust or small debris collecting on the webs during storage: the devices were not changed.

and slow the detectors.

In 2005, the chopping wheel motor failed three times. The first two replacements failed due to improper oiling: one was not oiled, and the second one's oil froze at the ambient temperatures. While we do not have time constant data while the motor was not operational, the time constants were observed to be constant during the rest of the 2005 season, and it is expected that they remained constant in the missing weeks. Differenced maps of RCW38, a very bright HII region, constructed from left-going minus right-going chopper sweeps should be a sensitive probe of transfer function mis-estimates. We examined these maps for the full year and detected no sign of a transfer function mis-estimate during the time when the calibrator was inoperational.

Chapter 4

Power Spectrum Analysis

There are a number of well-developed algorithms to estimate the CMB power spectrum from a data set [6, 30, 74, 76, 77]. These algorithms loosely fall into two categories depending on whether the noise matrix is inverted or Monte Carlo simulations are used. The processing time required for matrix-based algorithms scales with the map size as N_{pixel}^3, while the time needed for Monte Carlo methods scales with the number of samples as $N_{timestream} * ln(N_{timestream})$. ACBAR has been analyzed with a matrix-based algorithm due to the small field sizes, the lack of cross-linking, and the asymmetric filtering induced by its scan strategy. Here, we first outline the method used to calculate the ACBAR power spectrum and then dive into the implementation details.

4.1 Power Spectrum Analysis Overview

Following the conventions of the previous data releases, the band-powers $\mathbf{q}$ are reported in units of μK^2 and are used to parameterize the power spectrum according to

$$\ell(\ell+1)C_\ell/2\pi \equiv \mathcal{D}_\ell = \sum_B q_B \chi_{B\ell} \, , \tag{4.1}$$

where $\chi_{B\ell}$ are tophat functions; $\chi_{B\ell} = 1$ for $\ell \in B$, and $\chi_{B\ell} = 0$ for $\ell \notin B$. The ACBAR observations were carried out in a *lead-main-trail* (LMT) pattern. Originally, the three fields were differenced according to the formula $M - (L + T)/2$ in order

to remove time-dependent chopper synchronous offsets. In K07, this conservative strategy was shown to be unnecessary and an un-differenced analysis presented. We continued to observe in a lead-trail or LMT pattern in 2005 in order to produce maps wider than the maximum range ($\sim 3°$) of the chopping tertiary mirror. The un-differenced analysis presented in K07 and used for this paper's results is outlined below with any differences in the application to the 2005 data set highlighted.

Let d_α be a measurement of the CMB temperature at pixel α. The data vector can be represented as the sum of the signal, noise, and chopper synchronous offsets: $d_\alpha = s_\alpha + n_\alpha + o_\alpha$. For example, although the chopping mirror moves the beams at nearly-constant elevation, the slight residual atmospheric gradient produces a chopper synchronous signal o_α, which is a function of chopper angle with an amplitude of around 20 - 50 mK.

To remove these offsets, the data from each chopper sweep are filtered with the "corrupted mode projection" matrix $\mathbf{\Pi}$ to produce the cleaned time stream $\tilde{\mathbf{d}} \equiv \mathbf{\Pi d}$. The $\mathbf{\Pi}$ matrix projects out a third to tenth order polynomial which suppresses large angular scale chopper offsets. The order of the polynomial removed depends on the amplitude of atmosphere-induced cross-channel correlations. As described in K07, small angular scale offsets can be be removed by subtracting an "average" chopper function. In 2002, we remove a chopper synchronous offset from each data strip, where the amplitude of the offset at each sample in the strip is free to vary quadratically with elevation in the map. In 2005, we allow the offset to vary from a third to fifth order polynomial depending on the declination (dec) extent of the map. The large fields observed in 2005 could subtend up to four times the dec range of the fields observed in 2001 and 2002 ($\sim 10°$ vs. $\sim 2.5°$). A zeroth order polynomial removes the average chopper function. The higher order terms effectively act as a high-pass filter on changes in the offset as a function of time or elevation. This anisotropic filtering removes the offset-corrupted modes while preserving the maximum number of uncorrupted modes for the power spectrum analysis. The loss of information at high-ℓ is a small, as the removed modes account for only a few percent of the total degrees of freedom of the data.

The corrupted mode projection matrix Π can be represented as the product of two matrices, $\Pi \equiv \Pi_2\Pi_1$. The operator Π_1 is the original Π matrix referenced in K04, which adaptively removes polynomial modes in RA. The additional operator Π_2 removes modes in Dec independently for each of the lead, main, and trail fields and can be further decomposed into the product $\Pi_2 = \Pi_2^{Poly}\Pi_2^{LPF}$. The operator Π_2^{Poly} performs the forementioned polynomial projection in Dec to remove small-scale chopper offsets. The second operator Π_2^{LPF} imposes a low-pass filter $\ell < 3200$ on each Dec strip. The Dec strips are perpendicular to the scan direction; the timestreams have always had a low-pass filter applied in the scan direction. The need for the Dec low-pass filter was discovered through the jackknife tests (see §5.3); however, it is fundamentally advantageous to apply the low-pass filter. The pixelation used for the power spectrum is too large to resolve all of the noise power (at ℓ up to 10,800), causing out-of-band noise to be aliased into the signal band ($\ell < 3000$). Eliminating this high-frequency noise reduces the contribution of instrumental noise on the reported band-powers.

Using the pointing model, the cleaned timestreams are coadded to create a map:

$$\mathbf{\Delta} = \mathbf{Ld}.$$

The noise covariance matrix of the map can be represented as

$$\mathbf{C}_N = \mathbf{L}\langle\mathbf{nn}^t\rangle\mathbf{L}^t,$$

where $\mathbf{n}$ is the timestream noise. The noise matrix is diagonalized as part of applying a high signal-to-noise transformation to the data. Eliminating modes with insignficant information content reduces the computational requirements of later steps in the analysis.

In order to apply the iterative quadratic band-power estimator, we need to know the partial derivative $\frac{\partial \mathbf{C}_T}{\partial q_B}$ of the theory covariance matrix $\mathbf{C}_T$ with respect to each band-power q_B. The theory matrix can be estimated by considering the effects of the

filtering on the raw sky signal. The signal timestream s_α is the convolution of the true temperature map $\mathfrak{T}(\mathbf{r})$ with the instrumental beam function $B_\alpha(\mathbf{r})$

$$s_\alpha = \int d^2 r \mathfrak{T}(\mathbf{r}) B_\alpha(\mathbf{r}).$$

The signal component of the coadded map will be $\boldsymbol{\Delta}^{\mathbf{sig}} = \mathbf{Ls}$ or

$$\Delta_i^{sig} = \int d^2 r F_i(\mathbf{r}) \mathfrak{T}(\mathbf{r}), \tag{4.2}$$

where we have defined the pixel-beam filter function F_i

$$F_i(\mathbf{r}) = \sum_\alpha L_{i\alpha} B_\alpha(\mathbf{r}). \tag{4.3}$$

The theory covariance matrix can be calculated in the flat sky case to be

$$C_{T\{ij\}} \equiv \langle \Delta_i \Delta_j \rangle^{sig} = \iint d^2 r d^2 r' F_i(\mathbf{r}) F_j(\mathbf{r}') \langle \mathfrak{T}(\mathbf{r}) \mathfrak{T}(\mathbf{r}') \rangle$$

$$= \iint d^2 r d^2 r' F_i(\mathbf{r}) F_j(\mathbf{r}') \int \frac{d^2 l}{(2\pi)^2} C_\ell \cdot e^{i\mathbf{l} \cdot (\mathbf{r} - \mathbf{r}')}$$

$$= \int \frac{d^2 \ell}{(2\pi)^2} C_\ell \cdot \tilde{F}_i^*(\mathbf{l}) \tilde{F}_j(\mathbf{l}), \tag{4.4}$$

where $\tilde{F}_i(\mathbf{l})$ is the Fourier transform of the pixel-beam filter function. The partial derivative of the theory matrix can be calculated straightforwardly from equations 4.1 and 4.4.

Although this algorithm does not require the instrument beams to remain constant, we impose that restriction in this analysis. The actual ACBAR beam sizes vary slightly with chopper angle [65]. The measured beam variations can be fit to a semi-analytic function as described in K04 to create a more accurate representation of the true beam shape across the map. We use the corrected beam sizes when removing point sources. In K04 and K07, we found that the differences in the power spectra from using the averaged beam or exact beam for each pixel were negligible. For the
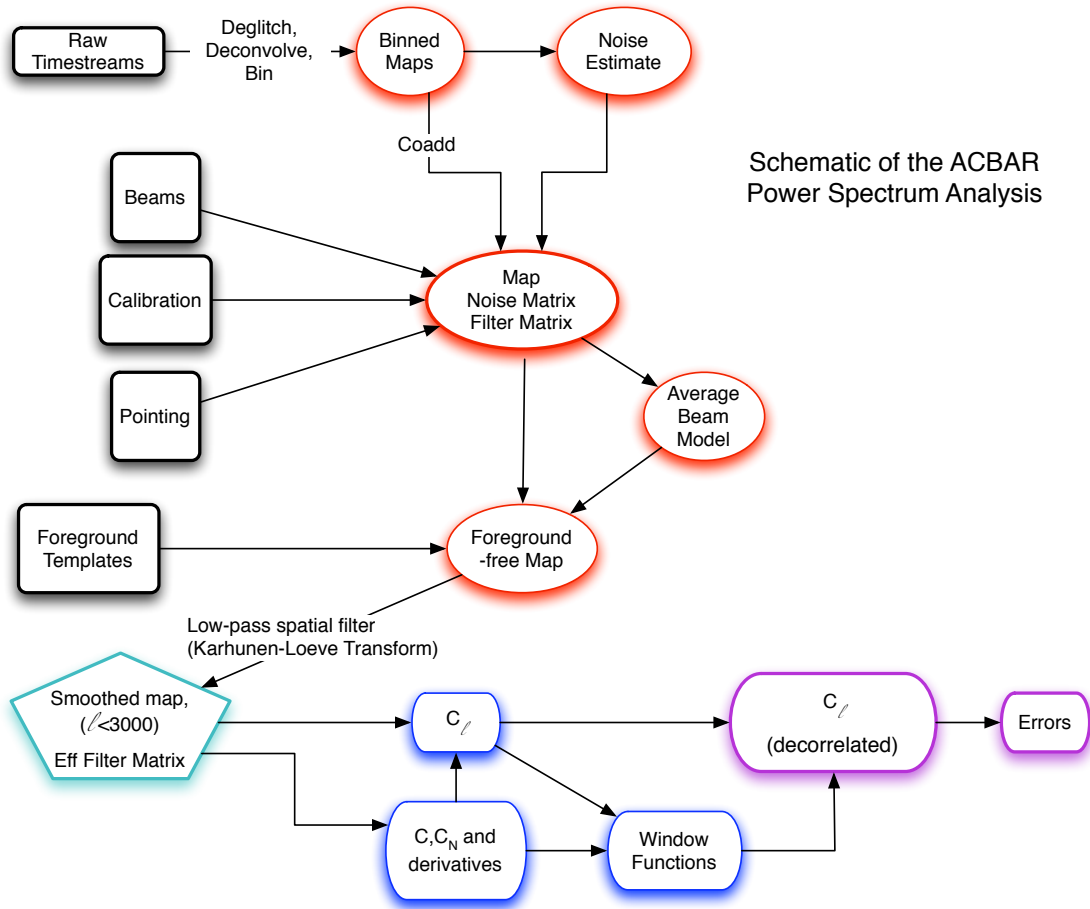
Figure 4.1: An schematic view of the ACBAR power spectrum analysis. Details of each step can be found in the text.

band-powers reported in Table 5.1, an averaged beam is used for the entire map.

As in K07, we calculate the full two dimensional noise correlation matrix directly from the time stream data without using Fourier transforms (§4.4).

All the numerical calculations are performed on the National Energy Research Scientific Computing Center (NERSC) IBM SP RS/6000. The evaluation and Fourier transform of $F_i(\mathbf{r})$ is the most computationally challenging element of this analysis. We use an iterative quadratic estimator to find the maximum likelihood band-powers [6]. The results of this analysis are presented in Table 5.1 and Figure 5.1.

4.2   Data Cuts

We enacted a number of data cuts to avoid introducing spurious signals into our time streams. Some observations had egregious problems, for instance if there was a power outage or the fridge ran out in the middle of an observation. We cut the entire observation if it had problems associated with the fridge temperature, the bias voltage, or telescope pointing. A detailed list of the cuts and the fraction of data flagged is presented in Table 4.1.

Spider web bolometers enjoy a very low cross-section to cosmic rays, which allows us to be quite conservative about removing cosmic ray hits. The published power spectrum is insensitive to the exact level of the cosmic ray cuts. We generated power spectrum of our deepest fields (CMB5 & CMB8) with stricter cosmic ray cuts and found the power spectrum to be unchanged.

The pipeline has three layers of cosmic ray cuts. The first cut is intended to flag points which railed the A/D before the timestream is Fourier transformed. It checks for massive hits above a set voltage threshold in the raw timestreams. The second cut is checked after the bolometer and electronic time constants have been deconvolved. A cosmic ray hit should be a delta function, and is highlighted by an effective high pass filter: $y'[i] = y[i] - \sum_{j=i-m,i+m} y[j]/(2m+1)$, with m=4. Any point in the high pass filtered timestream more than 5.5 standard deviations from zero is flagged. This test is run iteratively to avoid allowing extremely bright cosmic rays from influencing the standard deviation and the cut level. The third cut is a variation on the map-based cosmic ray cuts used by other experiments. The dominant signal in the raw timestreams is actually the chopper synchronous offsets. Therefore, we compare each sweep to the chopper synchronous signal averaged over a period of 15 minutes. If any point deviates by >4 standard deviations from the average for that chopper position, the sweep is flagged. (Sweeps near known bright sources are excluded from this cut.)

We flag the entire sweep (1.7s of data) if a cosmic ray is detected in it by any of the three cuts. In the extremely rare case that a cosmic rays lands within 26ms (6.5 times the average bolometer time constant) of the border, both sweeps are flagged.

Class	Label	Description	Frequency
Electronics	Abnormal bias	Bias voltage is outside the nominal range of 2.7-2.9V	rare
Electronics	Unstable bias	No bias voltage may vary by more than 5%	rare
Fridge	Baseplate Warm	Baseplate temperature is above 250 mK	occasional
Fridge	Unstable Temperature	Baseplate temperatute varies by >3%	rare
Pointing	Wrong pointing	Telescope was pointed at the wrong RA/Dec	few
Pointing	Pointing not achieved	Telescope did not reach the commanded RA/Dec	few
Optical	Variable DC levels	The DC bolometer voltages shifted by >2% due to changes in optical loading. This will impact the bolometer responsivity and calibration	rare
Optical	Tipper Unusable	350 μm tipper data is unavailable. (used to measure optical depth)	10%
Optical	Snow cut	Snow on mirrors	25%
Chopper	Abnormal chopper function	Chopper range or frequency is incorrect.	5%

Table 4.1: Data cuts applied to the ACBAR data

On average, 2% of the time stream is flagged for cosmic ray hits. The bulk (98%) of the flagged data is in the very conservative buffer; ∼530 samples are flagged around the ∼9 samples affected by a typical cosmic ray.

The Viper mirrors and ground shield make a bowl-like shape ideal for collecting snow drifts. Our valiant winterover has the daily chore of sweeping the snow off the mirrors while the fridge is cycling. The process can take some gymnastics, as shown in Picture 4.2. In bad weather, snow can still pile up in between the daily cleanings. Snow accumulation on the mirrors has a number of unpleasant side effects: increased chopper synchronous signals, increased loading, and reduced sensitivty. Most seriously, snow will increase the actual optical depth without affecting the the 350-μm tipper data used to monitor the optical depth. This could bias our calibration. The

Figure 4.2: Our 2005 winterover, Jessica Dempsey, cleaning snow off the tertiary mirror. Snow removal can require some acrobatics for someone in a parka.

higher frequency channels are more sensitive to snow; therefore the 280 GHz channels were used as a snow cut in 2001 to 2004. In 2005, we replaced the 280 GHz channels with additional 150 GHz detectors and had to develop a new snow cut. The most readily detectable effect of snow is to reduce the observed flux of RCW38. We therefore cut observations for which we observed low fluxes for RCW38. Additionally, if the RCW38 flux changed significantly (>10%) from one observation to the next, the intervening period is cut because it is impossible to determine when the when the change occured.

4.3   Time-dependent Pointing Shifts

While a global offset is meaningless, a time-dependent pointing drift could impact the CMB band-power estimation. Pointing drifts are especially worrisome when considering fields observed across multiple years. The bright quasars in the deep CMB

fields are used to measure possible pointing offsets. The maps are created following the algorithm for the power spectrum maps, however with a finer $1'$ - $2'$ resolution. Chopper synchronous offsets are less significant for centroiding a bright source, so the dec polynomial filtering is reduced to a zeroth order polynomial. A $30'$ square around the QSO is extracted to determine the pointing offsets. The mean is removed from each column and row of this square, with the points within $7'$ of the center masked, in order to correct for the filtering shadows around the bright point sources. A two-dimensional gaussian is fit to the cleaned maps, and the pointing correction is calculated as the difference between the fit centroids and nominal position of the quasar. These offsets can be up to an arcminute, somewhat larger then would be expected for the nominal pointing RMS residuals of $\sim25''$ on sources used in the ACBAR pointing model. The offsets applied to the CMB data are tabulated in Table 4.2 and have a measurement uncertainty of $\sim12''$ - $20''$.

4.4 Timestreams to Chopper-voltage Binned Maps

There are two time constants suppressing high frequency information in the raw timesteams: the bolometer time constants and the time constants of the read-out electronics. The electronic time constants are an order of magnitude faster than the bolometric time constants. As described below, we remove spikes due to cosmic rays and then Fourier transform the timestream to deconvolve both time constants. A low-pass filter is applied at the same time. For the results in this work, the LPF was set to $f < 16 - 17\ Hz$, corresponding to $\ell < 3200 - 3400$. The results are insensitive to the exact LPF used for $f < 20\ Hz$. There are microphonic lines in the PSDs above 20 Hz.

To reduce the computational requirements, the ACBAR timestreams are down-sampled after deconvolution, but before being passed to the map-making software. More precisely, the timestreams are interpolated at fixed positions of the chopping flat mirror. Interpolation is chosen instead of binning, as each bin may only be hit once or twice per chopper period. In these conditions, binning can introduce artifi-

	CMB5		CMB8	
Period	ΔRA	ΔDec	ΔRA	ΔDec
Mar/Apr '02	-0.63	0.42		
Apr/May '02	-0.58	1.13		
Jun/Jul '02	-0.34	1.18		
Jul '02	-0.05	0.36		
Jan/Feb '04	0.18	-1.26	0.19	-1.06
May '04	-0.17	0.01	-0.10	-0.27
Jun '04	0.12	-0.12	0.04	-0.34
Mar/Apr '05	-1.44	0.01	0.07	0.13
Apr/May '05	-1.11	0.49	0.06	0.32
Jun '05	-0.67	0.86	0.10	0.36
Oct '05	0.32	0.43	0.75	0.51

Cross-year Fields

	CMB52,3,4		CMB7(ext)	
Year	ΔRA	ΔDec	ΔRA	ΔDec
2001	0.00	0.00		
2002	0.10	0.60	0.00	0.60
2005			0.60	0.00

Table 4.2: Measured pointing offsets across the four years of ACBAR observations. The CMB5 and CMB8 observations are spread out across several months in each year, and this time has been subdivided into several periods for offset calculations. These periods have been aligned with natural break points due to observing changes or telescope maintenance. The other fields were observed for less time in each year, and a single offset parameter is applied to correct the year-to-year drift. Unlisted fields were observed for less time and in a single year, and have not had pointing corrections applied. There was some evidence for a constant $<1'$ offset in the uncorrected fields.

cial features and see-sawing up and down due to the induced pointing mis-estimate. This is worsened because the periodicity of the ACBAR chopper period and sample frequency is such that these binning offsets can remain constant across multiple stares and cause striping on large scales. In some binned maps, this effect induced a high-frequency line in the PSD that was not present in the original timestream. The interpolation is done for each chopper sweep, and the sweeps are averaged. A sweep is one full chopper period, and there are 10-20 sweeps per stare. Approximately 5% of each sweep is discarded near the chopper turnaround to avoid dealing with the changing scan speed and potential vibrations excited by the turnaround. The result is refered to as the chopper-voltage binned map.

Interpolation has non-trivial effects on both the signal and noise. The effects are tested and quantified with Monte Carlo simulations. A number of fake signal-only timestreams were generated by re-observing simulated maps of the CMB or point sources with and without the interpolation. The simulations showed an effective low-pass filter in the scan direction which could be approximated by a Gaussian. This is unsurprising, since like binning and downsampling, interpolation loses high-frequency information. As it is approximately a Gaussian, interpolation's LPF can be dealt with with the experimental beam function (which is also approximated by Gaussian functions).

The noise properties of the ACBAR data are estimated for the chopper-binned maps. The noise is assumed to be stationary within a 36-50 minute interval and is estimated independently for each interval. Correlations between stares are neglected, but correlations between different chopper positions within a chopper sweep are explicitly calculated. Each sweep has been binned into N chopper bins, so this produces a NxN noise correlation matrix. The correlation matrix is then averaged over all the sweeps in the stare and all the stares in the ~ 45 minute chunk (~ 800 realizations). Cross-channel correlations between neighboring channels are calculated in the same manner and used for an atmospheric cut.
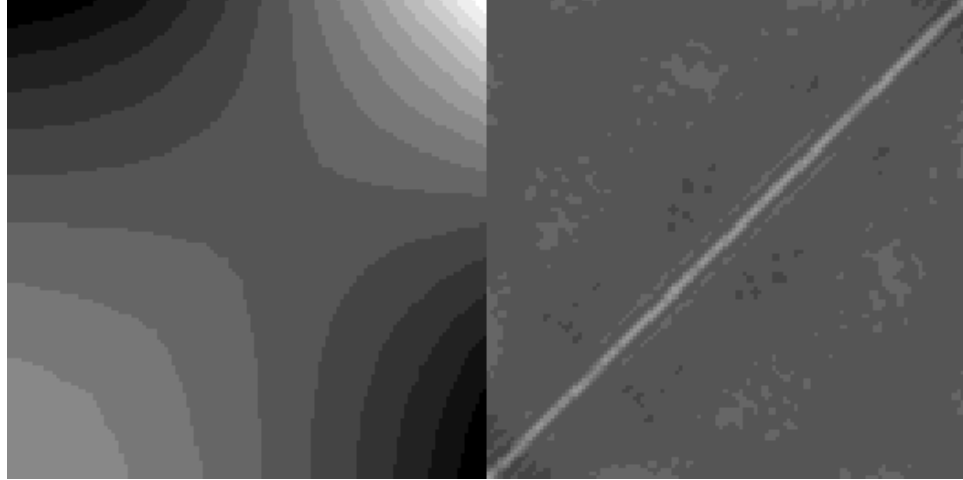
Figure 4.3: The auto-correlation matrix for a bolometer from an observation on 3/19/2005. The left-hand side is the raw auto-correlation matrix; the right-hand side is the matrix after a 4th-order polynomial has been removed in RA. The polynomial order was selected based on cross-channel correlations, as detailed in §4.5. The large-scale correlations introduced by the atmosphere are clearly visible on the LHS, but largely eliminated on the RHS. In the ideal of uncorrelated noise, the matrix would be purely diagonal. The finite width of the diagonal structure is caused by the finite signal bandwidth.

4.5 Naive Mapmaking and Filtering

Every experiment has noisy modes that can be filtered to increase the signal-to-noise of the result. The worst contaminants in the ACBAR data are chopper-synchronous offsets. The chopping mirror moves the beams approximately at a constant elevation, but the small modulation of atmospheric depth produces a chopper-synchronous signal. Actual offsets are further complicated by the effects of clouds, snow on the mirrors, and other factors. We remove these offsets with fitted polynomials in the fore-mentioned "corrupted mode projection" matrix $\mathbf{\Pi} = \mathbf{\Pi_2}\mathbf{\Pi_1}$. Figure 4.5 is an image of a single field of CMB8 at each stage of offset removal.

The $\mathbf{\Pi_1}$ matrix removes modes from each chopper sweep. The chopper sweeps fall in the RA direction at nearly constant declination, so this matrix effectively removes RA modes. We project out a third to tenth order polynomial to suppress the large angular scale chopper offsets. The degree of the polynomial removed from RA

is determined by comparing the magnitude of the auto-correlation to cross-channel correlations. The requirement is that the maximum of the cross-channel correlation function is less than 5% of the maximum of the auto-correlation function. Observations which do not meet this requirement with a tenth order polynomial are cut. Offsets on smaller angular scales are removed by the $\mathbf{\Pi_2}$ matrix, which removes a polynomial perpendicular to the sweeps.

We have always low-pass filtered the timestreams to avoid aliasing all noise and microphonic lines in the extra bandwidth into the signal band. For this work, we added a second LPF perpendicular to the scan direction. The raw chopper-binned maps have information on frequency scales well above the Nyquist frequency of the coadded map, as the declination step size between stares is a factor of three smaller than the map pixel size. This was accidentally realized in the course of investigating jackknife failures by examining the Fourier transform of the jackknife maps. The deepest field, CMB5, has $1'$ steps in dec corresponding to $\ell = 10,800$ and a map pixel size $= 3'$ or $\ell = 3600$. The exact frequencies vary between fields based on differences in the pixel size and dec spacing between stares. Noise and microphonics in this band will be aliased back into frequencies below $\ell = 3600$, increasing the noise in the maps and making the precision of the noise estimate more important.

The most straightforward solution given the structure of the analysis pipeline is to FFT and apply a LPF filter to the chopper-binned maps. This allows us to preserve information on the filtering and its effects on the underlying CMB power spectrum. Fourier transforms and low-pass filters are linear operations and can be expressed as matrix operations for a fixed filter and array size. If Ω is a vector representing the filter and M is the input vector, we want to find the matrix Π_{fft} such that

$$\Pi_{fft}M = FFT^{-1}[\Omega \times FFT[M]].$$

By expanding the FFT operation as $FFT[M](f) = \frac{1}{\sqrt{N}} \sum_x M(x) \times e^{-j2\pi fx/N}$, we can solve for:

$$(\Pi_{fft}M)(y) = \frac{1}{N} \sum_f \Omega(f) e^{j2\pi fy/N} \sum_x M(x) e^{-j2\pi fx/N}$$
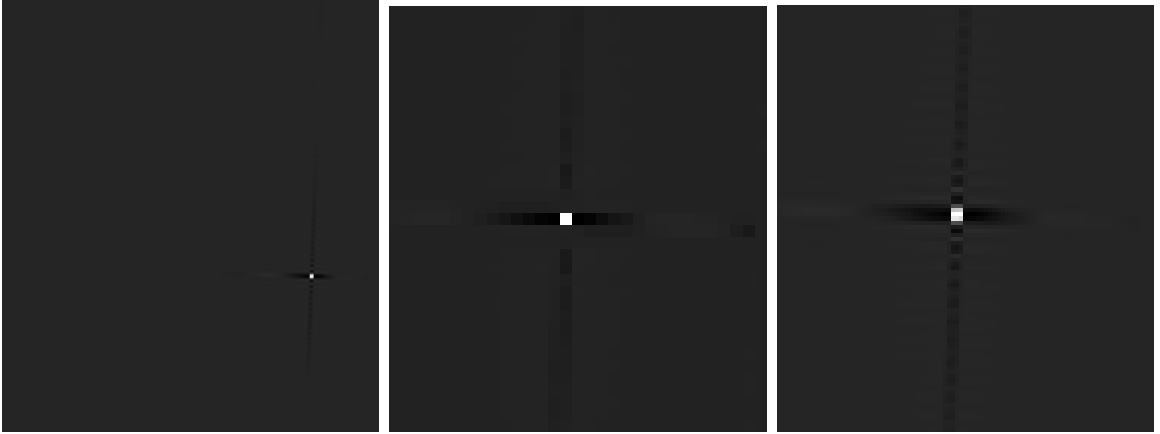
Figure 4.4: From left to right, the full high-resolution filtering matrix for a single pixel in CMB8, a blow-up of the low-resolution filtering matrix for the same pixel and a blow-up of the high-resolution filtering matrix. The coarse resolution matrix has the same pixel scale as the map and misses some of the features in the true filtering. The high-resolution version is used almost exclusively in the analysis and has a nine pixels within every map pixel. The large cross pattern is produced by the polynomial filtering. The high-frequency waves are a product of the LPF applied in the Dec direction.

$$(\Pi_{fft})_{yx} = \frac{1}{N} \sum_f \Omega(f) e^{j2\pi f/N \times (y-x)}.$$

The natural symmetries of this expression along with the symmetries of the FFT of a real vector allow the number of terms to be reduced further. The cut is implemented in 1D as $k_y < 3200$ rather than $k \equiv \sqrt{k_x^2 + k_y^2} < 3200$. Limiting it to 1D reduces the computational requirements of creating the filter matrix, as only the column and row have non-zero entries. The 1D low-pass filter matrix can easily be integrated into the analysis method as a revision to the matrix removing polynomials from Dec (Π_2) to create $\Pi_2' = \Pi_{lpf}\Pi_2$. We found that implementing this filtering improved the noise estimate and reduced the χ^2 of the jackknife tests.

The map is constructed by taking the weighted average of the filtered chopper-binned maps $\mathbf{\Pi d}$. The weighting of each stare ω_{stare} is based on the variance of the

center bin and is held constant for all bins in a stare.

$$\omega_{stare} = \frac{1}{\sigma^2_{center}}, \sigma^2_\alpha = \sum_{\beta\gamma} \Pi_{\alpha\beta} N_{\beta\gamma} \Pi_{\alpha\gamma}$$

$$T_i = \lambda_i \sum_\beta \omega_\alpha \Pi_{\alpha\beta} d_\beta$$

λ_i is set to fulfill the normalization condition for a pixel that $\lambda_i \sum_{\alpha\in i} \omega_\alpha = 1$.

The effective filtering matrix F_{ij} is a N_{map} x $N_{h.r.\ map}$ matrix, basically containing the weighted average of the various polynomials that have been removed. The map pixels at $3' - 6'$ are large compared to the ACBAR beam size of $5'$. Therefore, the filter matrix must have a higher resolution than the map in order to represent fully the actual filtering. Using a higher resolution improved the point source removal and reduced filtering artifacts in the power spectrum at low-ℓ. The high and low resolution version of the filter matrix for a typical pixel are shown in Figure 4.4. The matrix can be explicitly written as:

$$F_{ij} = \lambda_i \sum_{\alpha\in i,\beta\in j} \omega_\alpha \Pi_{\alpha\beta}.$$

A theoretical CMB sky map that has been convolved by the ACBAR beam can be transformed into the filtered ACBAR map basis by:

$$T_i^{ACBAR} = \sum_j F_{ij} T_j^0.$$

The full noise covariance matrix is built up in the same manner from the noise estimates constructed for the binned chopper maps (see §4.4). The ACBAR noise model assumes that different channels and stares are uncorrelated, but allows for bin-to-bin correlations within each stare.

[65] demonstrated that the ACBAR beam sizes depend on the angle of the chopping mirror. The changes can be fit by a function of the form $A' = A\sqrt{1 + c_1 V + c_2 V^2}$, where A is the beam area and V is the voltage supplied to the chopper. A given map
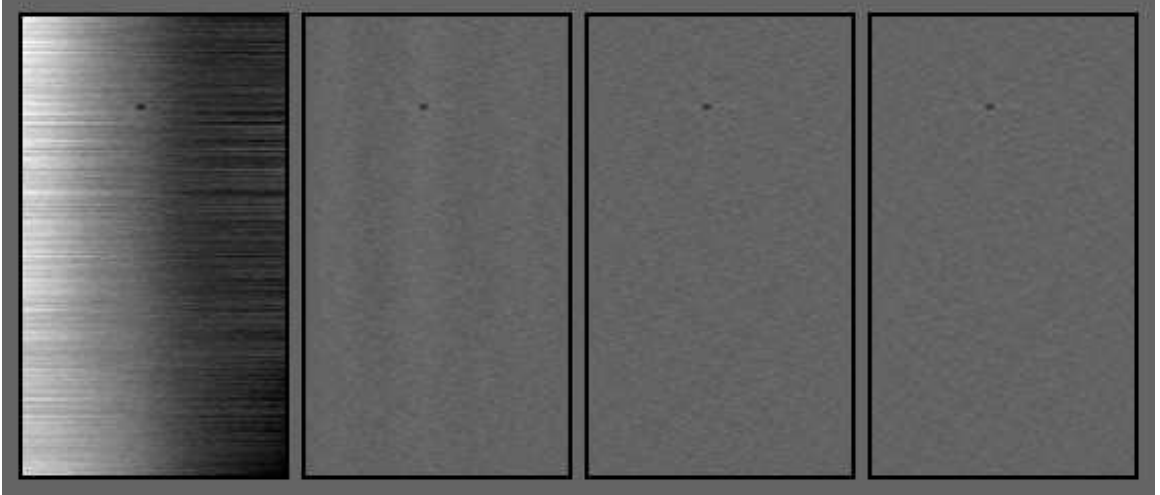
Figure 4.5: Maps of the trail field of CMB8 from a single observation with channel D4. From left to right, the raw map, the map after RA polynomial removal $(m' = \Pi_1 m)$, the map after RA and Dec polynomial removal $(m' = \Pi_2^{Poly}\Pi_1 m)$, and the fully cleaned map $(m' = \Pi_2^{LPF}\Pi_2^{Poly}\Pi_1 m)$. The bright point source is the quasar PMN J0538-4405. Pixels with bright sources are excluded from the calculation of the noise correlation matrix.

pixel will be observed multiple times with different channels and at different chopper voltages. To track this, a small array is created for each map pixel. Each time the pixel is hit, the expected beam shape is added to that array with the appropriate weight. Together with creating the high-resolution filter matrix, populating this beam array is the most time-consuming step of the coadding process. A second program fits a guassian to the full, averaged beam shape for each pixel, reducing the information content from a 2-dimensional map per pixel to two FWHMs. The same routine calculates the weighted-average beam size for the full map.

The power spectrum can be calculated either with the individual pixel beam functions or the map-averaged beam function. The resulting power spectrum is only slightly dependent of this choice since the beam area is conserved (K04, K06) and it is computationally advantageous to use a map-averaged beam function. The map-averaged beam function was used for the 2005 power spectrum results in this work. The pixel-specific beams are used to remove point sources.

4.6   Foreground Removal

The sky is cluttered with sources besides the CMB which could potentially contaminate the ACBAR power spectrum. This section focuses on the methodology for removing foreground-contaminated modes from the power spectrum: however, a variation on the method has been used to constrain the foreground amplitudes. While not the main focus of this thesis, foregrounds are an important field of study and will become increasing important as experiments take aim on the minuscule signals of the B-mode polarization. Foreground limits derived from the ACBAR data set are discussed in more detail in §6.3.

If we have a template for the position and shape of a source, its transformed shape in the ACBAR maps can be found by applying the filter matrix after convolving with the ACBAR beam: $S'_i = \mathbf{F}_{ij}S_j$. We populate an array $\mathbf{B}$ where the columns are the filtered versions of known, potential sources. If all the modes are independent, we can define the "bad mode" projection matrix as $\mathbf{\Pi_B} \equiv \mathbf{I} - \mathbf{B}(\mathbf{B^t B})^{-1}\mathbf{B^t}$ ([76]). It is easy to show that $\mathbf{\Pi_B B} = \mathbf{0}$. If the map is represented as $M = M' + S_{foreground}$, where $S_{foreground}$ is an linear combination of the modes in B, then the foreground-free map can be extracted with $M' = \mathbf{\Pi_B}M$.

In practice, the assumption that the modes are independent fails for a small number of highly overlapping modes. We initially resolved this by manually removing the near-duplicate modes. However, the difficulty can be dealt with more robustly by revising the algorithm, specifically the calculation of $(\mathbf{B^t B})^{-1}$. The inverse of a square matrix $\mathbf{A}$ can be written as $\mathbf{A}^{-1} = \mathbf{U^t \Lambda^{-1} U}$, where $\mathbf{\Lambda}$ is a diagonal matrix whose entries are the eigenvalues of $\mathbf{A}$ and $\mathbf{U}$ is a matrix whose columns are the eigenvectors of $\mathbf{A}$. If $\mathbf{A}$ is non-invertible, one or more eigenvalues will be zero. The appropriate entry in $\mathbf{\Lambda^{-1}}$ is replaced by zero for eigenvalues below some threshold, effectively eliminating terms until the remaining modes are linearly independent. The threshold is chosen to be 0.05. An alternative way to view this is that the small eigenvalue modes have practically no information content and can be deleted with minimal effects on the output.

Three types of foregrounds templates are removed from the ACBAR maps. The most blatant objects in the ACBAR maps are the central quasars. Most ACBAR fields are centered on a bright quasar for beam mapping and pointing checks. Being bright enough for a good beam map, these sources also have more than enough flux to affect the CMB power spectrum. The Monte Carloed effects of the CMB5 central quasar with and without masking can be seen in Figure 4.6. Given the amplitude, we treat the quasars and any other point source with $F_{150Ghz} > 170$ mJy differently than the dimmer point sources in the maps. One mode is removed per high-resolution pixel within $8'$ of the quasar, leaving the amplitude of each pixel as a free parameter. Effectively this will remove an arbitrary source shape and eliminates any dependence on the beam model or pointing solution.

There are also a number of lower flux point sources in the ACBAR fields. Following K04, we consider all point sources from the PMN catalogue in the ACBAR fields with $F_{4.8Ghz} > 40$ mJy. This list has $\sim$1600 sources. The majority of these are not detected at 150 GHz in the ACBAR maps. A foreground template is constructed corresponding to a point source at each location and added to the "bad mode" projection matrix $\mathbf{B}$. The beam shape for that specific map pixel, including the the beam variation with chopper position, is used instead of the map-averaged beam shape. Each of the PMN sources will be removed from the ACBAR maps without requiring prior knowledge of their flux at 150 GHz.

Finally, a dust template is removed from the ACBAR fields. The template is based on the FDS99 dust model at 150 GHz [20]. The FDS dust model is based on data from DIRBE and IRAS and has an angular resolution of $6'$. As with the radio sources, this input template map is multiplied by the ACBAR filtering matrix to make the "bad mode" template. The ACBAR fields are located in a region of low dust contrast (see Figure 3.2). The dust emission measured by IRAS at 100 microns in the ACBAR fields is $\sim$1 MJy/sr, while the average for the entire sky is 16 MJy/sr. We do not detect dust in any field, and the dust mode projection does not affect band-powers above $\ell > 100$.
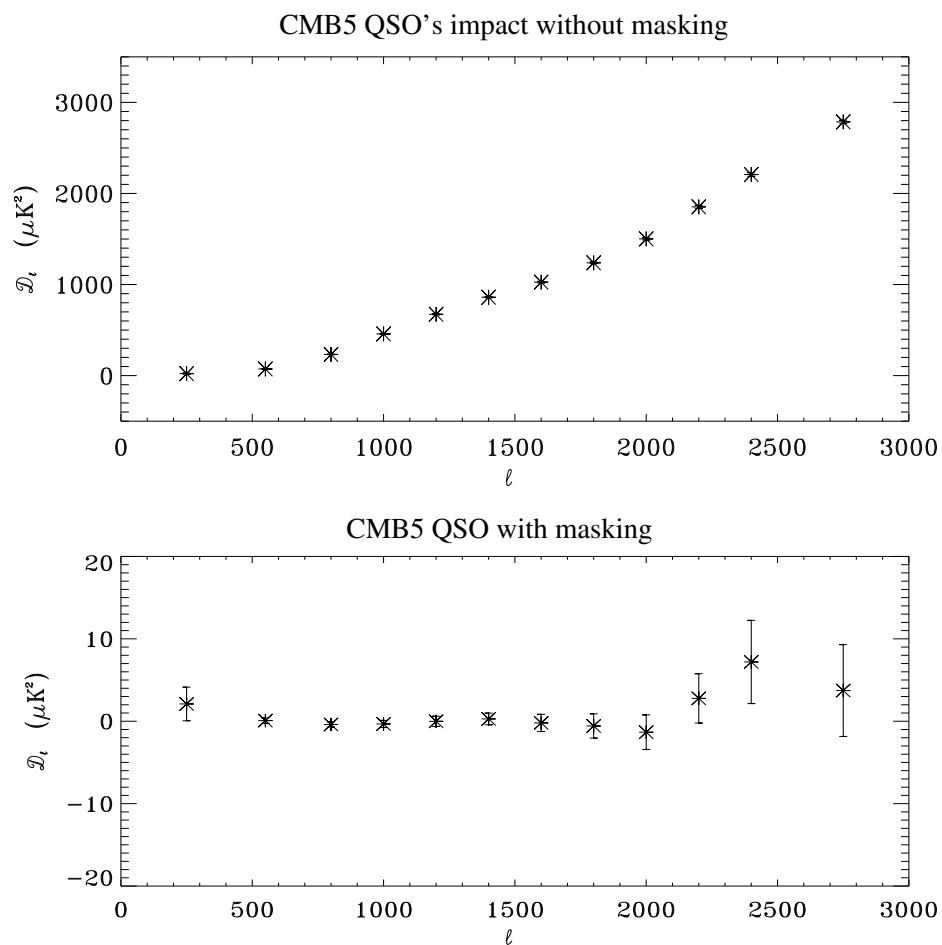
Figure 4.6: The central QSOs would dominate the CMB power spectrum if left unmasked in the maps (see top panel). CMB5 is ACBAR's deepest field and has the third brightest quasar (see Table 6.3). The masking method described in §4.6 reduces the power by a factor of more than 400 to a level consistent with zero (see bottom panel).

4.7 High S/N Mode Truncation

The data are compressed using a Karhunen-Loéve transfomation following Bunn and White [11] and Bond et al. [6]. The matrix method of power spectrum estimation scales as $O(N_{pixel}^3)$ due to the inversion of the $N_{pixel} \times N_{pixel}$ noise matrix. While this inversion must be done once, applying the signal-to-noise transformation to the data saves computational time in the later steps. The S/N transformation turns the noise matrix into the identity matrix and also reduces the numbers of independent modes used in the later analysis.

Following K02, the signal-to-noise transformation requires small modifications to deal with the modes zeroed by foreground removal. The foreground removal projection $\mathbf{\Pi_B}$ can be applied to the noise correlation matrix as well as the map, creating the filtered noise matrix $N' = \mathbf{\Pi_B N \Pi_B}$. The eigenvectors and eigenvalues of N' are calculated. If m-modes have been removed, then the first m eigenvalues will be zero. The "whitening" matrix is defined as

$$
\mathbf{W} \equiv \begin{bmatrix} | & | & & | \\ \omega_{m+1}^{-1/2}\mathbf{e}_{m+1} & \omega_{m+2}^{-1/2}\mathbf{e}_{m+2} & \ldots & \omega_n^{-1/2}\mathbf{e}_n \\ \downarrow & \downarrow & & \downarrow \end{bmatrix},
$$

with the result that $\mathbf{W}^t\mathbf{C}'_N\mathbf{W}$ is the (n-m) dimensional identity matrix. In this basis, we can proceed with the standard Karhunen-Loéve transfomation. The fiducial theory matrix is constructed from $C_T = \sum_B q_B \partial C_t / \partial q_B$, where q_B is the band-power of the theoretical power spectrum. K02 and K07 used a very conservative fiducial power spectrum, assuming a flat $D_\ell = 10^4 \ \mu K^2$ for all $\ell < 3000$. Since 2002, the CMB temperature anisotropies have been accurately measured by a number of experiments, allowing us to adopt a lower fiducial power spectrum and reduce the number of high S/N modes used in the analysis while remaining very conservative. We use the piece-wise flat power spectrum plotted in Figure 4.7. The whitening matrix is applied to the fiducial theory matrix to account for the mode removal before the K-L tranformation: $C'_T = W^t C_T W$. All modes with S/N ratios > 0.05 are kept.
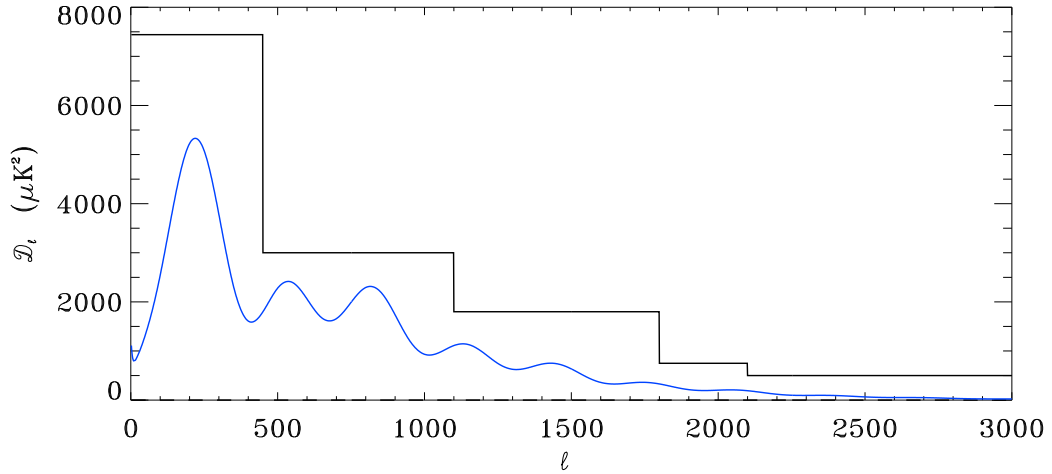
Figure 4.7: The fiducial power spectrum used for the ACBAR high signal-to-noise transformation. A WMAP3 model power spectrum is over-plotted in blue for comparison.

4.8   Bandpower Estimation

The ACBAR temperature anisotropy power spectrum is parameterized by the binned band-powers q_B as

$$D_\ell \equiv \sum_B q_B \chi_{B\ell}. \tag{4.5}$$

$\chi_{B\ell}$ is chosen straightforwardly to be a "top-hat" function. Binning significantly reduces the computational requirements ($O(N_{bins}^3)$) without losing very much leverage on cosmological parameters. Due to the the finite size of the ACBAR fields, individual D_ℓs are massively correlated, with a correlation length on the order of $\ell \sim 50$. The cosmological parameter estimation codes are designed for bin-to-bin correlations below 30-40% [13]. The final binning of the power spectrum presented in this thesis was chosen to achieve the maximum ℓ-resolution over the third to fifth acoustic peaks within that correlation constraint while degrading the resolution at other angular scales to reduce the computational requirements. The wider bins do not significantly reduce the scientific import of the ACBAR power spectrum, as at low-ℓ the results from large-scale experiments such as WMAP3 dominate, and at high-ℓ the power spectrum is featureless at the precision of the ACBAR measurements.

The ACBAR band-powers are estimated using the iterative quadratic estimator outlined in Tegmark [76] and Bond et al. [6]. The quadratic estimator relies on two successive approximations. First, the likelihood function will be a continuous function, and any continuous function can be approximated as a Gaussian near the peak. Effectively, this means truncating the Taylor expansion of the log likelihood function to the second-order:

$$ln\mathcal{L}(q_0 + \delta q) \simeq ln\mathcal{L}(q_0) \sum_B \frac{\partial ln\mathcal{L}(q_0)}{\partial q_B} \delta q_B + \frac{1}{2} \sum_{BB'} \frac{\partial^2 ln\mathcal{L}(q_0)}{\partial q_B \partial q_{B'}} \delta q_B \delta q_{B'}.$$

Assuming this functional form for the likelihood function allows us to directly solve for the maximum instead of sampling the likelihood function repeatedly. The δq_B to maximize the likelihood function will be:

$$\delta q_B = -\sum_{B'} \left[\frac{\partial^2 ln\mathcal{L}(q_0)}{\partial q_B \partial q_{B'}} \right]^{-1} \frac{\partial ln\mathcal{L}(q_0)}{\partial q_{B'}}.$$

These quantities can be expressed in array forms more naturally derived from a real data set. The first derivative can be written as:

$$
\begin{aligned}
\frac{\partial ln\mathcal{L}(q_0)}{\partial q_{B'}} \equiv \frac{1}{2}\mathbf{y_B} &= \frac{1}{2}Tr\left[(TT^t - C)\left(C^{-1}C_{T,B'}C^{-1} \right) \right] \\
&= \frac{1}{2}Tr\left[\left(TT^t C^{-1} C_{T,B'} C^{-1} \right) - \left(CC^{-1} C_{T,B'} C^{-1} \right) \right] \\
&= \frac{1}{2}\left[\left(T^t C^{-1} C_{T,B'} C^{-1} T \right) - Tr\left(C_{T,B'} C^{-1} \right) \right],
\end{aligned}
$$

and the second derivative can by renamed the curvature matrix $\mathcal{F}_{BB'}$:

$$
\begin{aligned}
\mathcal{F}_{BB'}^{(q)} &\equiv -\frac{\partial^2 ln\mathcal{L}(q_0)}{\partial q_B \partial q_{B'}} \\
&= Tr\left[(TT^t - C)(C^{-1}C_{T,B}C^{-1}C_{T,B'}C^{-1} - \frac{1}{2}C^{-1}C_{T,B}C^{-1}) \right] \\
&\quad + \frac{1}{2}Tr\left(C^{-1}C_{T,B}C^{-1}C_{T,B'} \right),
\end{aligned}
$$

where $C_{T,B}$ is the partial derivative of C_T with respect to q_B and from Eq. 4.5 can

be calculated as

$$C_{T,B} = \sum_{\ell} \frac{\partial C_T}{\partial \mathcal{D}_{\ell}} \chi_{B\ell}. \tag{4.6}$$

The curvature matrix is still numerically impractical to compute repeatedly. We can approximate the curvature matrix by its ensemble average, the Fisher matrix $F_{BB'}$. To take the ensemble average, we assume that our band-powers and noise model are correct, so $\langle TT^t \rangle \equiv C$. This reduces the expression for the Fisher matrix to the last term, a much more tractable expression:

$$F_{BB'} \equiv \langle \mathcal{F}_{BB'} \rangle = \frac{1}{2} Tr \left(C^{-1} C_{T,B} C^{-1} C_{T,B'} \right). \tag{4.7}$$

With the above substitutions, the estimate for the next iteration's δq_B becomes:

$$\delta q_B = \frac{1}{2} \sum_{B'} F_{BB'}^{-1} y_B.$$

The final band-powers are found by iteratively applying the quadratic estimator with:

$$q_B^{n+1} = q_B^n - \rho \frac{1}{2} \sum_{B'} F_{BB'}^{-1} y_B, \tag{4.8}$$

where $\rho \in [0, 1]$ is a relaxation factor introduced to prevent the estimator from over-shooting and falling into a local minima. In practice, the relaxation constant was set to 0.1 for the first iteration and progressively increased to 0.5 by the fifth iteration. It is set to unity for the last iteration. The bandpowers converged to $\sim 1 \mu K^2$ in nine iterations and to $\lesssim 0.1 \ \mu K^2$ by the twelfth and final iteration. Bond et al. [6] show that the iterative quadratic estimator will converge to the exact maximum of the likelihood function. The errors estimated from the Fisher matrix are not exact; however as discussed below, we directly sample the likelihood function rather than using the Fisher matrix to estimate ACBARs bandpower errors.

As the ACBAR data set expanded with the inclusion of more data spread across more fields, the serial code to perform the iterative quadratic estimator became prohibitively expensive in time and memory usage. Fortunately, the time- and memory-

intensive steps are straightforwardly parallizeable, as each field is independent. In this case, the full data set arrays become summations over the equivalent terms for the individual fields, e.g.,

$$F_{BB'} = \sum_k F_{BB'}^k \quad \& \quad y_B = \sum_k y_B^k,$$

where k denotes one of the ten ACBAR fields. The calculation of $F_{BB'}$ and y_B are the most computationally-intensive steps. Once the code was optimized sufficiently to handle the largest single field on a shared memory node, expanding it to multiple fields by allocating one or more fields to each node is simple. This allocation requires minimal data transfer ($F_{BB'}$ and y_B) between nodes. The slowest node determines the timing for each iteration, as the results from all the fields are required to calculate $F_{BB'}^{-1}$ and determine the starting point of the next iteration q_B^{n+1}. A simple algorithm was implemented to dynamically allocate the fields between nodes in order to balance the load based on the time required for each field $t \sim O(n_s^3 N_{bin})$, where n_s is the number of high S/N modes kept and N_{bin} is the number of ℓ-binnings. It worked quite well.

The band-powers will be correlated due to ACBAR's finite sky coverage. We follow the treatment of [27] to de-correlate the band-powers for presenting the ACBAR results. The correlated band-powers are multiplied by the de-correlation matrix $\mathbf{W}$,

$$\hat{q}' = \mathbf{W}\hat{q}, \tag{4.9}$$

to produce de-correlated band-powers. $\mathbf{W}$ is determined by decomposing the Fisher matrix as $\mathbf{F} = \mathbf{W}^T \mathbf{W}$. The correlation matrix in the new basis is diagonal as $\mathbf{W} \left\langle qq^T \right\rangle \mathbf{W}^T = \mathbf{W} \mathbf{F}^{-1} \mathbf{W}^T = \mathbf{I}$. There is not a unique solution to this equation. Multiplying a de-correlation matrix $\mathbf{W}$ by any orthonormal matrix will produce a new solution. We use the square root of the Fisher matrix for the de-correlation matrix $\mathbf{W} = \mathbf{F}^{1/2}$.

4.9   Estimating the Band-power Uncertainties

A Gaussian distribution is completely described by its mean and covariance matrix. The curvature, or Fisher, matrix is defined as the inverse of the covariance matrix. Under the assumption of Gaussianity, a simple estimate of the band-power errors can be derived by evaluating the Fisher matrix at the maximum of the likelihood function. However, the distribution is not Gaussian. The likelihood function evaluated from many independent modes will tend towards Gaussianity near the peak due to the central limit theorem, but the tails of the likelihood function will only slowly converge towards a Gaussian distribution.

As discussed in Bond et al. [7], the assumption of Gaussianity will lead to a "cosmic bias". The bias arises because the true uncertainty is dependent on the band-powers $\delta \mathcal{C}_\ell = (\mathcal{C}_\ell + \mathcal{N}_\ell/B_\ell^2)/\sqrt{\ell + 1/2}$, while for a Guassian distribution $\delta \mathcal{C}_\ell$ is independent of $\mathcal{C}_\ell$. $\mathcal{N}_\ell$ is a representation of the noise power spectrum, and B_ℓ^2 is the experimental beam function. Due to this, positive fluctuations above the true mean are more likely than would be predicted by a normal distribution, while negative fluctuations are less likely. The bias is most significant at low ℓs.

The offset-lognormal distribution [7] is a better approximation to the true likelihood function. If Z_ℓ is defined such that $\delta Z_\ell \propto \delta \mathcal{C}_\ell/(\mathcal{C}_\ell + \mathcal{N}_\ell/B_\ell^2)$, then δZ_ℓ is a constant and Z_ℓ can be approximated by a Gaussian distribution. The reported ACBAR band-power uncertainties utilize the offset-lognormal approximation,

$$Z_\ell \equiv ln(\mathcal{C}_\ell + x_\ell). \tag{4.10}$$

The curvature σ and log-normal offsets x_ℓ in Table 5.1 are determined by explicitly fitting the likelihood function rather than an analytic formula based on the Fisher matrix or $\mathcal{N}_\ell/B_\ell^2$. We evaluate the Fisher matrix at the peak of the likelihood function and use it to set a characteristic scale for fluctuations in each bin's bandpower. As the bandpower's have been de-correlated, the Fisher matrix is diagonal with a value of $1/\sigma_i^2$ for the ith bin. The true likelihood is calculated at 11 points per bin, in

0.5σ increments from -2.5σ to $+2.5\sigma$, and fit to the log-normal functional form to determine the published error estimates. While evaluating the likelihood function is slow, this method is straightforwardly parellizeable since it boils down to $N_{fields} \times N_{bins} \times 11$ almost independent calculations. It is interesting to note that the likelihood fitting provides a confirmation that the derived band-powers are near the maximum likelihood solution. If the band-powers are shifted away from the maximum likelihood solution by a few μK^2, the log-normal functional form has trouble fitting the measured likelihood surface.

4.10   Window Function Calculation

We have laid out the algorithms used to derive the ACBAR band-powers from the data. In order to extract science, we must also be able to go from a theoretical power spectrum to the band-powers. To do so, we need to determine the band-power window functions, W_ℓ^B, defined by:

$$\langle q_B \rangle = \sum_\ell \left(W_\ell^B / \ell \right) \mathcal{D}_\ell^{th}, \tag{4.11}$$

where $\mathcal{D}_\ell^{th}$ is the theoretical power spectrum for a given set of cosmological parameters. The natural normalization is $\langle q_B \rangle = \mathcal{D}_\ell$ for a flat power spectrum. The window function is particularly important for a small-scale experiment like ACBAR whose bin width is comparable to the scale of features in the power spectrum. The window function for the quadratic estimator was determined in Knox [36] to be

$$W_\ell^B / \ell = \frac{1}{2} \sum_{B'} (F^{-1})_{BB'} Tr \left(\frac{\partial C_T}{\partial D_\ell} C^{-1} C_{T,B'} C^{-1} \right). \tag{4.12}$$

We imposed a limit on the ℓ-range considered in these sums to speed the numerical calculation. If a bin is defined by $\ell \in [\ell_{min}, \ell_{max}]$, then the sum was done only for $\ell \in [\ell_{min} - 500, \ell_{max} + 500]$. This width was chosen by contrasting the true and truncated window functions for the last ACBAR data release [43] and requiring the

maximum bandpower mis-estimate for any bin to be $< 0.1\%$ for a suite of WMAP-derived power spectra. This is an insignificant compared to the other sources of uncertainty in the band-power estimation. Based on Eq. 4.6 and 4.7, it can be seen that the window function will fulfill the normalization condition:

$$\sum_\ell \chi_\ell^B W_\ell^B / \ell = \delta_{BB'}.$$

This condition proved a useful sanity check of the derived window functions. Monte Carlo realizations of the CMB sky for the WMAP3ext model were used to confirm that the calculated window functions agreed with the average Monte Carlo band-powers to $\lesssim 1\%$.

The required resolution of the window function is not immediately obvious beyond the limits of $\triangle \ell_{window} \in [1, \triangle \ell_{bin}]$. The goal will be to bin the window function sufficiently finely that either the power spectrum $\mathcal{D}_\ell^{th}$ is flat across the bin or the true window function is flat across the bin. An all-sky experiment might not need to define a window function, as its ℓ-space resolution is sufficient to pick out every feature in the power spectrum. This is not the case for ACBAR. The ACBAR window functions reported here are binned with $\triangle \ell_{window} = 15$. This resolution is well below the expected scale of features in the power spectrum and also below the observed scale of features in the window function. The calculated window functions are plotted in Fig. 4.8 and are smoothly peaked functions centered at each bin center with negative wings abutting the neighboring bins. A numerical tabulation of the window functions is available on the ACBAR website[1].

The window function code is computationally intensive. Fortunately, it is trivially parallizeable in terms of splitting $W_\ell^B / \ell = \sum_i (W_\ell^B / \ell)_i$ for each field i. The matrices $K_B = (F^{-1})_{BB'} (C^{-1} C_{T,B'} C^{-1})$ are pre-computed for each field. With this division, the largest field ran in under 3 hours. This code could be parallized further if needed: there would be at most a modest duplication of effort if each shared-memory node calculated a subset of the ℓ-bins.

---

[1]http://cosmology.berkeley.edu/group/swlh/acbar/
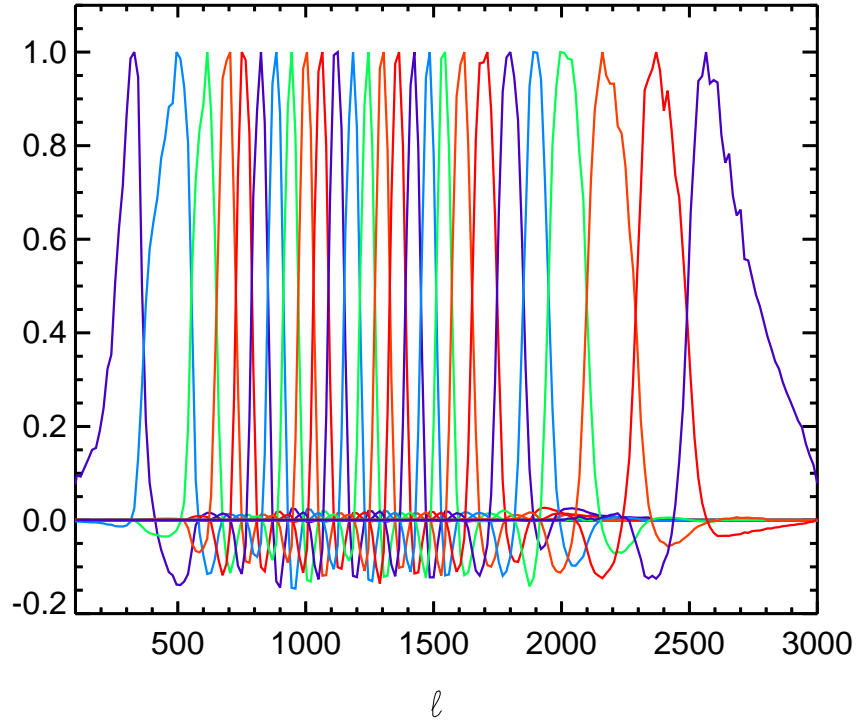
Figure 4.8: The window functions calculated for the ACBAR power spectrum de-correlated band-powers. The window functions have been normalized to unity for plotting purposes. The resolution of the window function is $\triangle\ell_{window} = 15$. The left-most bin is discarded for the published power spectrum. The window function of the right-most bin is calculated above $\ell = 3000$, although the plot ends at that point.

4.11   Transfer Function

The ACBAR power spectrum estimation algorithm outlined above is intended to be an unbiased estimator of the underlying power spectrum. This is one of the fundamental differences between it and Monte Carlo estimators such as MASTER which explicitly determine an effective transfer function from Monte Carloes. Any filtering applied to the ACBAR data which might affect the signal bandwidth was performed in the map domain and accounted for in the analysis by the filtering matrix F_{ij}. There is an important caveat to this ideal. The inputs are the chopper-binned maps instead of the raw time streams, and multiple operations are necessary to produce those maps. For instance, the timestreams have been low-pass filtered at an effective ℓ-scale of 3200. Although each operation was designed to avoid biasing the transfer function,

it is interesting to test their cumulative effect to confirm the assumption that the transfer function is unity.

As in the MASTER algorithm, signal-only Monte Carloes are used to measure the actual ACBAR transfer function. 100 realizations of the CMB sky are generated with 1' resolution. For each stare, the pointing for each channel is calculated at a set of chopper voltages approximately 0.5' apart. The pointing is used to look up the input signal $s_i(v_j)$ for that chopper voltage and channel. The chopper voltage at every data point in the stare is known; the signal voltage timestream for each channel is linearly interpolated from the set of sampled signal voltages. Several variants on the method involving different voltage spacings, theory map resolutions, and interpolation schemes were tested in order to understand the elements of the transfer function unique to the Monte Carlo version of the mapmaking code. The finite pixel size of the theory map caused a noticeable drop in high-ℓ power and was corrected for by dividing the input power spectrum by the calculated B_ℓ^2 of the theory map's pixels.

After the construction of the signal-only timestreams, the Monte Carlo code follows the analysis pipeline exactly. The chopper-binned maps are generated from the timestreams. Maps are generated from the coadded chopper-binned maps and then projected into the high-S/N basis of the real maps. The power spectrum is then calculated and compared to the input power spectrum for the original CMB realizations. We found that the transfer function agreed with unity for the pipeline after the chopper-binned maps: the creation of the chopper binned maps introduced a bias. The transfer function dropped smoothly from unity to 0.88 in power by $\ell = 3000$. Upon testing, it became clear that the roll off of high-frequency power is caused (unsurprisingly) by an interpolation step in the creation of the chopper-binned maps. The timestreams are interpolated to fixed chopper voltages to create these maps. The interpolation effectively changes the experimental beam function in the chop direction. However, the effect of this extra beam smoothing should already be accounted for in the real data, as the beam functions for each channel are measured from maps created by coadding the interpolated, chopper-binned maps. We therefore conclude that the ACBARs power spectrum estimation algorithm is unbiased to the limits of

our Monte Carlo test, approximately 10% of the cosmic variance for each band-power.

Chapter 5

Power Spectrum Results and Cosmological Parameters

5.1 Power Spectrum

The ACBAR band-powers for the CMB temperature anisotropies are listed in Table 5.1 and plotted in Figures 5.1 and 5.2. Band-powers have been derived from $\ell = 350$ to 3000 using the methods described in Chapter 4. The band-powers have been de-correlated so that each bin is independent unless otherwise noted. The maximum bin-to-bin anti-correlation is 21% before de-correlation. Decorrelating reduces the number of parameters required to describe the data set and makes the interpretation of plots more intuitive.

The damping tail and higher acoustic peaks of the TT power spectrum are clearly visible in the ACBAR band-powers. The temperature anisotropies have been measured at extremely high S/N out to $\ell \sim 2500$, as can be seen by comparing the band-powers to the instrumental noise only error bars in the bottom panel of Figure 5.4. The deepest ACBAR field is cosmic variance limited below $\ell = 1950$, while the shallowest field is cosmic variance limited to $\ell = 1090$. Individual power spectra for the seven largest fields are shown in Figure 5.3 to demonstrate the degree of agreement between fields.

There is stunning consistency between the ACBAR data at small angular scales ($\ell \lesssim 3000$) with CMB models derived from the largest angular scales ($\ell \lesssim 600$).
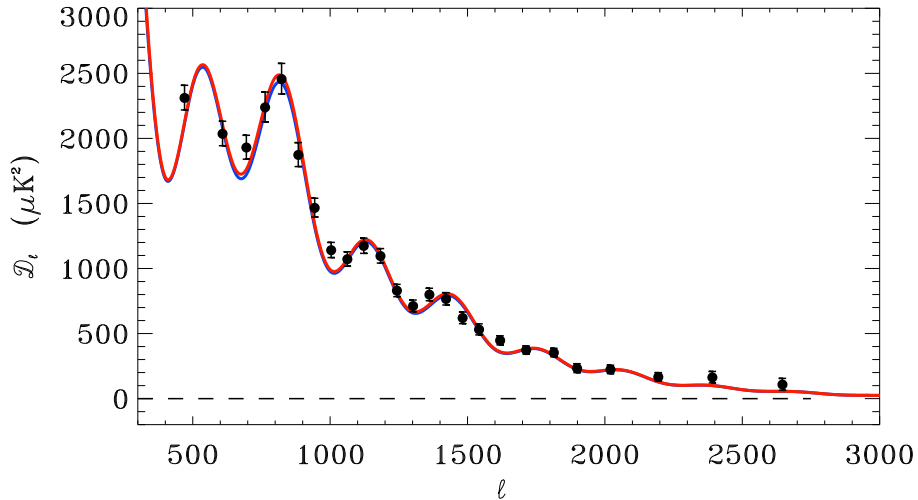
Figure 5.1: The decorrelated ACBAR band-powers for the full data-set. The 1-σ error bars are derived from the offset-lognormal fits to the likelihood function. The band-powers are in excellent agreement with a ΛCDM model. The red model line is the best fit to the WMAP3 and ACBAR band-powers for a flat universe. The blue model line is the best fit to the WMAP3 band-powers alone. The damping of the anisotropies is clearly seen with a S/N > 4 out to $\ell = 2500$. The third acoustic peak (at $\ell \sim 800$) and fourth acoustic peak (at $\ell \sim 1100$) are visible.

This is a strong test of the cosmological model and one which is convincingly passed. Figure 5.1 shows the ACBAR band-powers over-plotted on the WMAP3-only best fit model. The χ^2 of the ACBAR band-powers to the WMAP3+ACBAR best-fit model is 30.7 for 25 bins. There is a suggestion of a small excess above $\ell = 2000$ that could be due to excess SZE power as hypothesized in [59] or foregrounds. The excess is discussed in §5.4.

5.2 Cosmological Parameters

An analysis of the cosmological implications of the ACBAR data set in underway but not yet complete. The ACBAR data will be combined in various combinations with a number of other data sets (large-scale structure, WMAP3, all-CMB, BBN, supernovae and Hubble constants measurements) to determine parameter constraints. Preliminary results indicate that the 1-dimensional parameter errors will shrink slightly with

ℓ range	l_{eff}	q (μK^2)	σ (μK^2)	x (μK^2)
350-550	470	2311	95	-355
550-650	608	2035	94	-311
650-730	695	1930	92	-274
730-790	763	2239	114	-245
790-850	823	2456	118	-262
850-910	884	1873	92	-168
910-970	943	1466	72	-107
970-1030	1003	1141	58	-18
1030-1090	1062	1071	56	17
1090-1150	1122	1174	59	35
1150-1210	1183	1096	56	77
1210-1270	1243	830	47	123
1270-1330	1301	712	44	159
1330-1390	1361	799	48	198
1390-1450	1421	766	47	224
1450-1510	1482	620	45	248
1510-1570	1541	531	42	235
1570-1650	1618	447	35	268
1650-1750	1713	373	31	248
1750-1850	1814	353	33	271
1850-1950	1898	233	34	175
1950-2100	2020	223	32	209
2100-2300	2194	166	32	250
2300-2500	2391	163	44	367
2500-3000	2646	108	46	575

Table 5.1: Band multipole range and weighted value ℓ_{eff}, decorrelated band-powers q_B, uncertainty σ_B , and log-normal offset x_B from the joint likelihood analysis of the 10 ACBAR fields. The PMN radio point source and IRAS dust foreground templates have been projected out in this analysis.

addition of the ACBAR data to the WMAP3 data set. The largest improvements are to $\Omega_b h^2$, $\Omega_c h^2$, σ_8, and the age of the universe. Due to unbroken degeneracies between parameters, the 1D error estimates may not tell the full story of ACBAR's impact on the allowed likelihood volume. A multi-dimensional analysis of the allowed likelihood space is also planned.
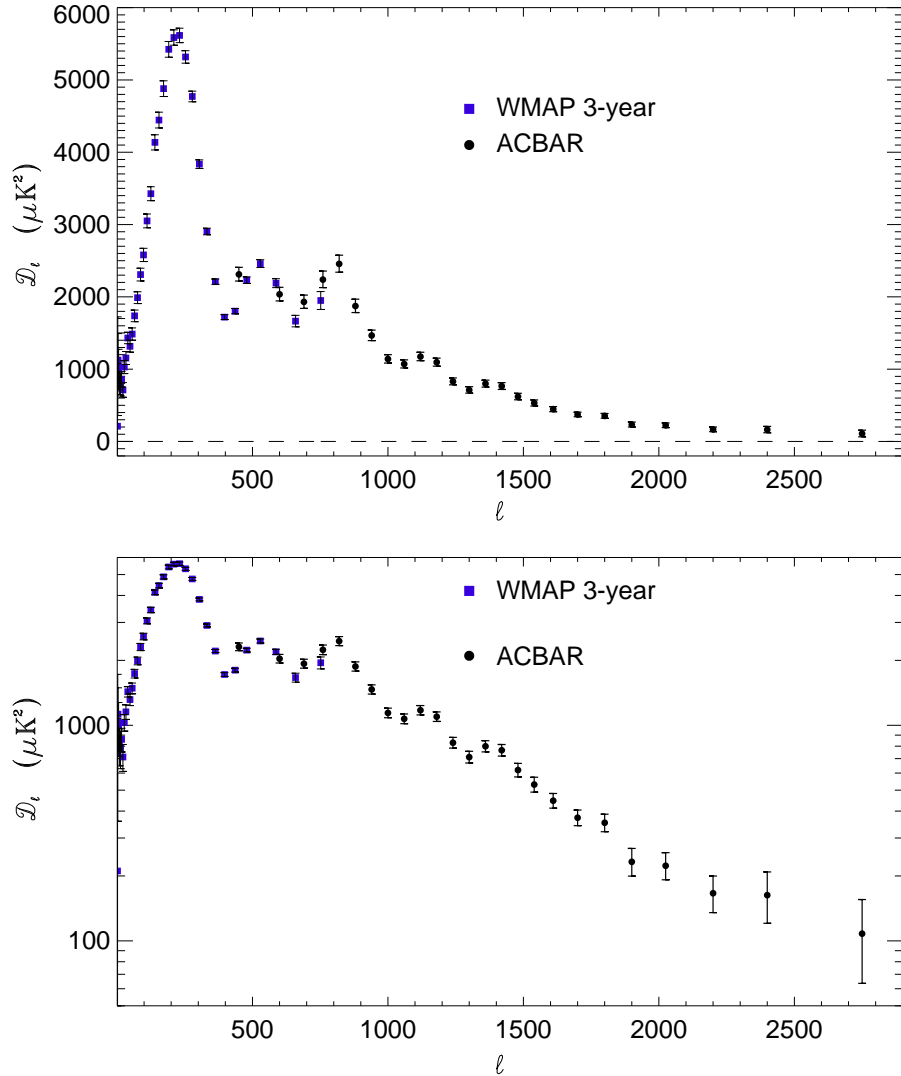
Figure 5.2: The decorrelated ACBAR band-powers for the full data-set plotted with the WMAP3 band-powers. The combined data set covers angular scales from $\ell = 2$ to 3000. The 1-σ error bars for ACBAR are derived from the offset-lognormal fits to the likelihood function. The damping of the anisotropies is clearly seen with a S/N > 4 out to $\ell = 2500$. The first four acoustic peaks can be seen and there are hints of the fifth acoustic peak. The positions of the peaks are regularly spaced in ℓ at $\sim$200, 500, 800, 1100 and 1400.

5.3   Systematic Tests

We performed a series of jackknife tests to constrain the amplitude of potential systematic errors in the power spectrum results. In a jackknife test, the data set is split into two sets which are differenced with the expectation that the result will consistent
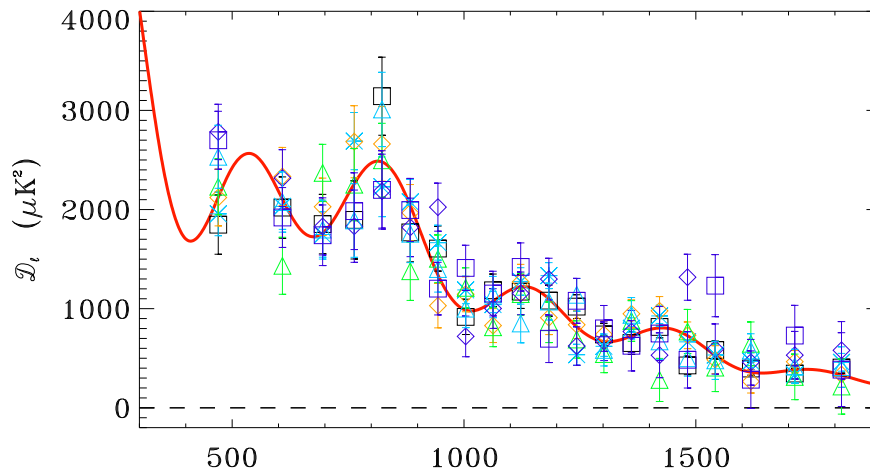
Figure 5.3: The correlated ACBAR band-powers for the seven largest fields. The anti-correlations between neighboring bins are between 10% and 20%. While unbiased, these are not the maximum likelihood band-powers. These band-powers are the result of a single iteration of the quadratic estimator. The plotted errors are derived from the diagonal elements of the fisher matrix and are only plotted to provide a rough estimate of the actual errors. The plotted model line is the best fit to the WMAP3 and ACBAR band-powers. Note the consistency between the fields and with the model.

with signal-free noise realization. Significant departures from zero can reveal the presence of systematic errors in the two sets. Depending on the details of splitting, there may also be a small residual signal component due to filtering or coverage differences. The residual signal can be accounted for with a suite of Monte-carlo realizations. By their nature, jackknives probe systematics down to instrumental noise level and are the most sensitive tests at angular scales where cosmic variance of the signal is dominating the band-power error budget. For instance, at large angular scales ($\ell = 500$), the ACBAR band-power errors are $\sim$100 μK^2 for the power spectrum and $\sim$1 μK^2 for the jackknife tests, while at small angular scales ($\ell = 2500$), the band-power errors are $\sim$40 μK^2 for both. Two main jacknife tests are applied to the ACBAR data: "left-right" and "first half - second half". The results of each test are discussed below and plotted in Figure 5.4.

As described in K04, the data can be divided into two halves based on whether the chopping mirror is moving to the left or right. The "left minus right" jackknife is a sensitive test for errors in the transfer function correction, microphonic vibra-
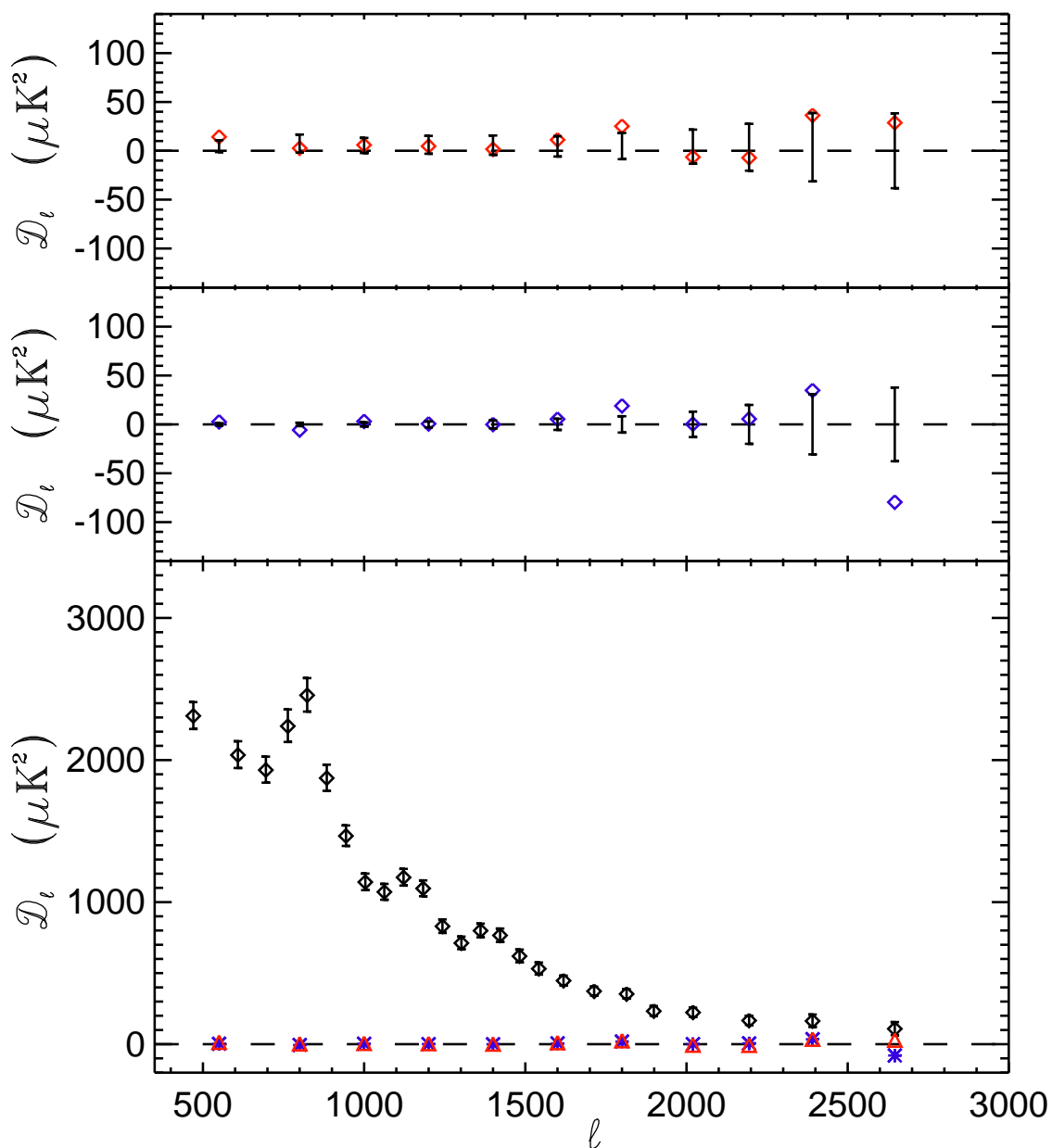
Figure 5.4: Systematic tests performed on the ACBAR data. *Top*: Power spectrum (*diamonds*) for differenced maps from the first half of the season and second half of the season for each field, compared to the results of Monte Carlo simulations (*error bars*). *Middle*: Power spectrum (*diamonds*) derived from difference maps of the left- and right-going chopper sweeps for all ten fields. *Bottom*: The undifferenced band-powers from Table 5.1 (*black diamonds*) compared to both jackknife power spectra: the left-right jackknife (*blue star*) and first half-second half jackknife (*red triangle*).

tions excited by the chopper motion, or the effects of wind direction. Maps with bright sources such as RCW38 can provide particularly powerful tests of the transfer function. Similarly, the data can be divided based on when the observation occured. A non-zero signal can be produced in the "first half minus second half" jackknife by calibration variations, pointing shifts, beam and sidelobe changes, or any other time dependent effects. In addition, the band-powers of both jacknives constrain the mis-estimation of noise.

We performed both tests on the 2005 CMB power spectrum and find the band-powers of each jacknife are inconsistent with zero at 2.5σ at high-ℓ ($\ell > 2100$). We reran a set of left-right jacknives dropping individual channels, and found that two channels stood out. With both channels excluded, the discrepancy in the left-right jackknife band-powers disappeared. We were unable to find evidence for unusual microphonic lines or transfer functions in the two problematic channels. We hypothesize that these two channels have subtle microphonic lines that are detectable only in a deep integration. Both channels are excluded from the 2005 data for all band-powers reported in this paper.

This did not fully resolve the high-ℓ excess observed in the first-second half jackknife. The excess was comparable to a 7% underestimation of the noise power spectrum N_ℓ and was a $\sim 2\sigma$ deviation from zero. We examined the differenced maps in the Fourier plane and realized that noise was present on angular scales extending up to $\ell = 10800$. The analysis algorithm as presented in K07 did not implement a low-pass filter in the direction perpendicular to the scan direction. The Nyquist frequency of the map pixel scale is well below this number, so some fraction of this extra power will be aliased into the signal band, increasing the amplitude of the effective noise power spectrum and the measurement's sensitivity to the noise estimate. A low-pass filter was added with an edge at $\ell = 3200$. This filtering reduces the amplitude of the noise power spectrum by 8% in the $\ell \in [2500, 3000]$ bin. With the 'dec LPF' filtering, the 2005 first-second half jackknife is consistent with zero signal above $\ell = 1100$. The original excess power was likely due to a small mis-estimation of the out-of-band high-frequency noise properties.

We apply the first half-second half jackknife test to the joint CMB power spectrum with the exclusion of the bad channels from the 2005 data and application of the 'dec LPF' to all data. These cuts are used for all band-powers reported in this paper. The power spectrum of the chronologically-differenced maps is compared to the band-powers of a set of Monte-carlo realizations of differenced maps in order to account for a number of effects that are expected to contribute power such as the small filtering differences due to different scan patterns and the temporal uncertainty in the beam sidelobes (see §3.3). We find that the jackknife band-powers are consistent with the predictions of the Monte-carlo above $\ell = 400$. There is a 4σ residual of ~ 15 μK in the first bin. We tentatively posit that since the combined statistical and cosmic variance uncertainty in this bin is a factor of six larger, the band-power estimate will be unbiased.

We also perform the left-right jackknife on the joint CMB power spectrum. The results are consistent with zero for $\ell > 900$. Statistically, the probability to exceed the measured χ^2 for $\ell > 900$ is 15%. The results are inconsistent with zero at a very low (~ 4 μK^2) level (Fig. 5.4) on larger angular scales. The discrepancy would be consistent with a small noise mis-estimate at low ℓ, possibly caused by neglected atmospheric correlations. The jackknife failure of ~ 4 μK^2 is much smaller than the band-power uncertainties (90 - 300 μK^2) in these ℓ-bins. At these angular scales, the band-power uncertainties are dominated by cosmic variance. The first-second half jackknife is insensitive to discrepancies of this magnitude due to the greater uncertainties introduced by the residual filtering differences. We cautiously conclude that the left-right jackknife failure will not significantly impact the error estimate for the combined power spectrum.

In addition to the above baseline jackknives, we explored a number of variations. One of the more useful was a set of 'double' jacknifes. In these, two "left-right" difference maps were created out of the first and second half of observations or the even and odd observations. The two maps were differenced again to estimate band-powers. In principle, this test limits the sources of a jackknife failure and can tease out the time scale involved. For example, the second differencing should not improve

the noise estimate, but the second jackknife consistently reduced the excess at small angular scales. The results of these tests were one reason to conclude that the initial left-right jackknife was failing due to subtle time constant or microphonic issues in some channels and led to the individual channel tests described above.

5.4 Anisotropies at $\ell > 2000$

Several theoretical calculations [14, 37] and hydrodynamical simulations [5, 80] suggest that the thermal Sunyaev-Zel'dovich effect power spectrum will be brighter than the primary CMB temperature anisotropies for $\ell \gtrsim 2500$ at 150 GHz. The amplitude of the SZE power spectrum is closely related to the amplitude of matter perturbations, which is commonly parameterized as σ_8. The SZE power spectrum is expected to scale as σ_8^7. To a lesser extent, the level of the SZE will also depend on details of cluster gas physics and thermal histories. The non-relativistic thermal SZE (ΔT_{SZ}) has a unique frequency dependence

$$\frac{\Delta T_{SZ}}{T_{CMB}} = y \left(x \frac{e^x + 1}{e^x - 1} - 4 \right), \tag{5.1}$$

where $x = \frac{h\nu}{kT_{CMB}} = \nu/56.8\,\text{GHz}$. The variable y is the Compton parameter and is proportional to the integral of the electron pressure along the line of sight. The CBI extended mosaic observations [59] have more power than is expected for the primary CMB anisotropies above $\ell = 2000$. The excess may be the first detection of the SZE power spectrum [50, 59, 5]. However, there are alternative explanations for the observed power ranging from an unresolved population of low-flux radio sources to non-standard inflationary models [15, 25, 72] that produce greater-than-expected CMB anisotropy power at small angular scales. The frequency dependence of the excess can be exploited to discriminate between the SZE and other potential explanations for observed power.

The ACBAR band-powers reported in this paper are slightly higher at $\ell > 2000$ than expected for the "WMAP3+ACBAR" best fit model. We subtract the predicted

band-powers at $\ell > 1950$ from the measured band-powers in Table 5.1 and fit the residuals to a flat spectrum . We find an excess of $34 \pm 20 \mu K$. The ACBAR excess at 150 GHz can be compared to the CBI excess measured at 30 GHz to place constraints on the frequency dependence of the excess power. The "WMAP3-ACBAR" model band-powers are subtracted from the measured band-powers of each experiment at $\ell > 1950$. We parameterize the excess at the two frequencies as $P_{30} = \alpha P_{150}$ and sample the likelihood surface for $\alpha \in [0, 10]$ and $P_{150} \in [0, 300]$ μK^2. The ACBAR beam uncertainty and the calibration error for both experiments is taken into account by Monte-carlo techniques. The likelihood function is averaged over 1000 realizations under the assumption that each of the three errors has a normal distribution. The resultant likelihood function is shown in Figure 5.5. We have assumed that dusty galaxies do not contribute significant power. Given the ACBAR and CBI frequency bands, the ratio, α, should equal 4.3 for the SZ effect. If the excess is due to primary CMB anisotropies, the ratio will be unity ($\alpha = 1$). It is six times more likely that the excess corresponds to the SZE than to primary CMB anisotropies. We expect the flux of radio sources to be a factor of ten or higher at 30 GHz than at 150 GHz ($\alpha \leq 0.1$). Radio sources are only slightly disfavored in this analysis and are $\sim 50\%$ as likely as the SZE to be the source of the excess. Although the detection of excess power in the ACBAR spectrum is more robust than in K07, the constraints on the frequency dependence of the excess are largely unchanged. A firm detection of the power at both 30 and 150 GHz is needed to improve the constraints.

Alternatively, we can infer the foreground amplitudes which would be required to explain the observed excess and compare the inferred amplitudes to those measured in §6.3. The excess might be explained by dusty galaxies or radio sources. The major uncertainty in estimating the band-power contributions from dusty galaxies and radio sources lies in extrapolating the measured fluxes at other frequencies to 150 GHz. We therefore estimate the required spectral dependence $S_\nu \propto \nu^\beta$ to produce the observed excess for each source. We subtract the predicted band-powers at $\ell > 1950$ from the measured band-powers in Table 5.1 and fit the residuals to a ℓ^2 point source spectrum. We find a best-fit excess of 46 ± 26 $(\ell/2600)^2 \mu K$. For dusty galaxies, we average the

number counts estimates from the SHADES survey [16] and Bolocam Lockman Hole Survey [48]. The fluxes of dusty galaxies would need to scale as $S_\nu \propto \nu^{-2.03}$ in order to explain an excess of $46(\ell/2600)^2 \mu K$. A $\beta = -2.03$ is well above the βs from -3 to -4 suggested in the literature. Radio sources might also be marshalled to explain the excess. The radio source band-power estimate is sensitive to the assumed spectral dependence of the sources used to extrapolate the flux cutoff from 4.85 GHz to 150 GHz. We find that $\beta = 0.07$ is required to produce the best-fit excess power. This is dramatically higher than the $\beta = -0.67$ estimated from binned source amplitudes in §6.3.
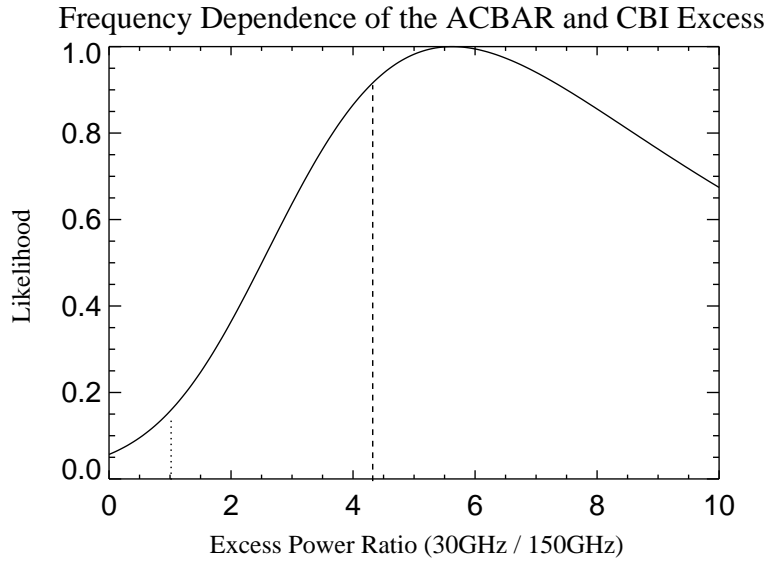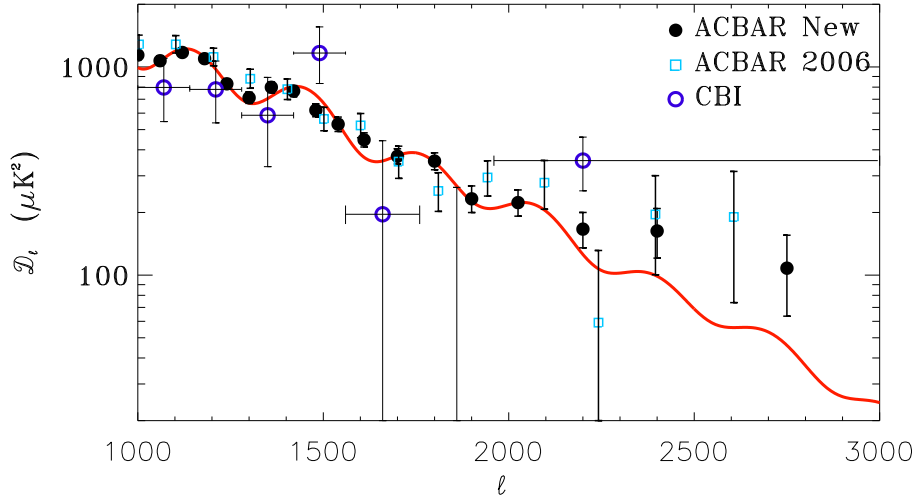
Figure 5.5: ACBAR results on the high-ℓ anisotropies. *Top*: The ACBAR band-powers above $\ell = 1000$ plotted against the best-fit model spectrum. The latest CBI results at 30 GHz are also shown. The ACBAR band-powers for $\ell > 1950$ are consistently above the model spectrum and below the CBI band-power. *Bottom*: The likelihood distribution for the ratio of the "excess" power, observed by CBI at 30 GHz and ACBAR at 150 GHz. The excess for each experiment is defined by a flat spectrum for $\ell > 1950$. The likelihood is estimated by examining the difference of the measured band-powers and the model band-powers. The vertical dashed line represents the expected ratio (4.3) for the excess being due to the SZ effect. If the excess power seen in CBI is caused by non-standard primordial processes, the ratio will be unity (blackbody), indicated by the dotted line. We conclude that it is 6 times more likely that the excess seen by CBI and ACBAR is caused by the thermal SZ effect than a primordial source. Radio source contamination of the lower frequency CBI data is only slightly disfavored. The excess is twice as likely to due to the SZ effect as to radio source contamination. This analysis assumes that dusty proto-galaxies are not a significant contaminant in the ACBAR maps.
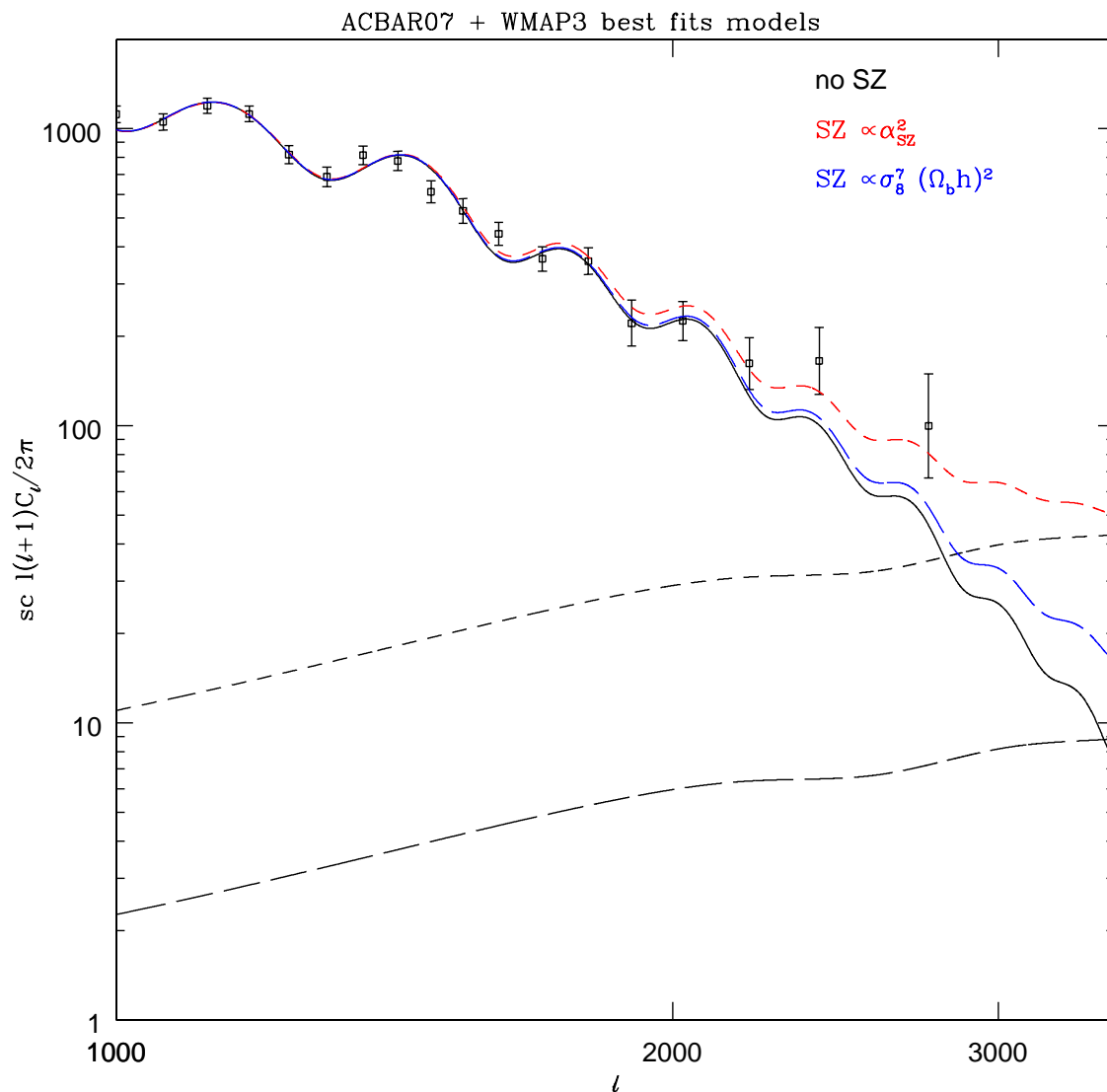
Figure 5.6: The decorrelated ACBAR band-powers for the full data-set plotted on top of three theoretical power spectra. The black curve is the best-fit WMAP3-ACBAR07 model spectrum without a SZE contribution. The blue curve includes the estimate of the SZE power spectrum based on the values of σ_8 and Ω_b derived from the large-angular scale WMAP3 band-powers. In the red curve, the amplitude of the SZE power spectrum has been added as a free parameter. The ACBAR high-ℓ band-powers favor a higher SZE amplitude than would be extrapolated from the low-ℓ power spectrum. Carlo Contaldi provided this plot.

Chapter 6

Other Science Prospects with ACBAR

In addition to measuring the power spectrum of CMB temperature anisotropies, the ACBAR data set has been used to quantify observing conditions at the South Pole [12], to conduct a blind SZ galaxy cluster survey [66], to make pointed SZ galaxy cluster observations [22, 62, 78, 79], to look for gravitational lensing of the CMB anisotropies, and to study foregrounds that may affect future CMB experiments. Several weeks were dedicated to pointed cluster observations. The other studies are based on the same maps as the CMB power spectrum, modulo differences in the data cuts and filtering. Each of these science goals will be discussed briefly in the following sections.

6.1   The Sunyaev Zel'dovich Effect

The Sunyaev-Zel'dovich effect (SZE) is caused by the inverse Compton scattering of CMB photons by hot electrons. The equilibrium pressure of gas trapped in the potential well of a massive cluster is very high, requiring commensurately high temperatures that ionize the hydrogen atoms. This plasma can account for up to 10% of the total cluster mass and can reach temperatures of up to 10^8 K. The hot electrons have a small scattering cross-section to passing CMB photons, allowing the two to exchange energy via inverse Compton scattering. As the electrons are much more energetic than the photons, the photons will gain energy on average. This perturbs the
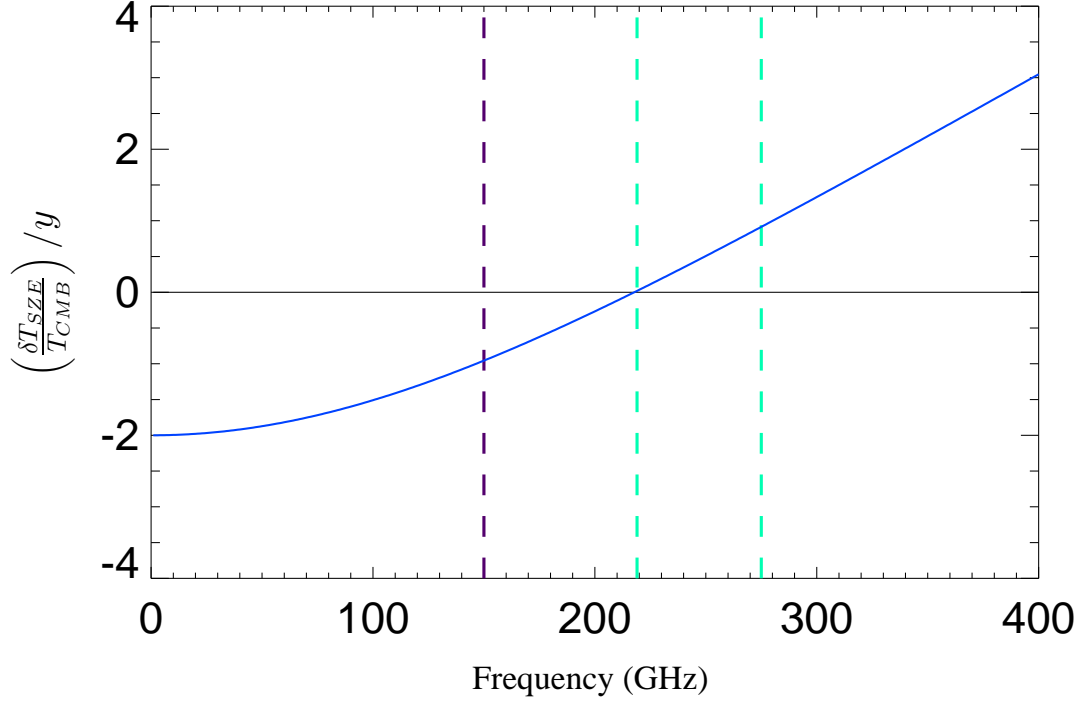
Figure 6.1: The frequency spectrum of the thermal Sunyaev-Zel'dovich Effect. The central frequency of each ACBAR band is marked with a dashed line. ACBAR's 150 GHz channels (purple) will see a SZ decrement. The CMB power spectrum results are derived from the 150 GHz channels. The 220 GHz band is centered at the SZ null and the 280 GHz band will see a positive SZ increment.

black body spectrum of the CMB photons along the line of sight passing through the cluster, creating the Sunyaev-Zel'dovich effect. The magnitude of the perturbation can be related to the Compton y-parameter, which is the integral of the electron gas pressure along the line of sight:

$$y = \frac{k_b \sigma_T}{m_e c^2} \int n_e T_e d\ell$$

where k_b is Boltzmann's constant, σ_T is the Thompson cross-section of an electron, and $m_e, n_e,$ and T_e are the electron mass, number density, and temperature, respectively. The frequency dependence in the non-relativistic limit can be found by applying the Kompaneets Equation with the assumption that $T_e >> T_{CMB}$ and the optical

depth is low ([2]):

$$\frac{\delta T_{SZ}(x)}{T_{CMB}} = y \ (\frac{x}{tanh(x/2)} - 4), \tag{6.1}$$

where $x = h\nu/k_b T_{CMB} = \nu/(56.85GHz)$. The frequency dependence is shown in Fig. 6.1. ACBAR's frequency bands are located below, at, and above the null at 217 GHz where there is no thermal SZ signal.

6.1.1 Blind Cluster Survey

A blind SZ cluster survey is the proverbial holy grail of SZE cosmology and has so far remained equally elusive. While the X-ray brightness of a cluster will fall as $1/z^4$ and the optical brightness of a cluster will fall off as $1/z^3$, the SZ flux is almost independent of the source's redshift. There is a slight redshift dependence, as the apparent size of the cluster depends on the angular diameter distance. A SZE galaxy cluster survey can potentially detect all clusters above a given mass out to their redshift of formation, giving SZ surveys a powerful advantage powerful advantage over optical and x-ray surveys. Galaxy cluster number counts (dN/dz) probe cosmology through their dependence on the volume element of the universe (dV/dz). The number counts are expected to yield sensitive tests of the dynamics of dark energy in particular. The cluster number counts will measure the volume element of the universe from redshifts of a few, where dark energy is sub-dominant, to the present day, when dark energy strongly affects the universe's expansion. Several experiments are planning to make large-scale SZ cluster surveys in the near future, two of which saw first light earlier this year (ACT [38] and SPT [63]). The field is likely to transform rapidly over the next few years, going from no cluster discoveries to thousands of new SZ clusters.

In the course of the CMB observations, ACBAR compiled multi-frequency coverage for 180 deg^2 and single-frequency coverage at 150 GHz for an additional 530 deg^2. Preliminary results for the 2001 and 2002 data sets were reported in [64]. In that analysis, the most sensitive mass limits were reached with single-frequency 150 GHz maps due to the increased noise in the 220 and 280 GHz frequency bands. Due
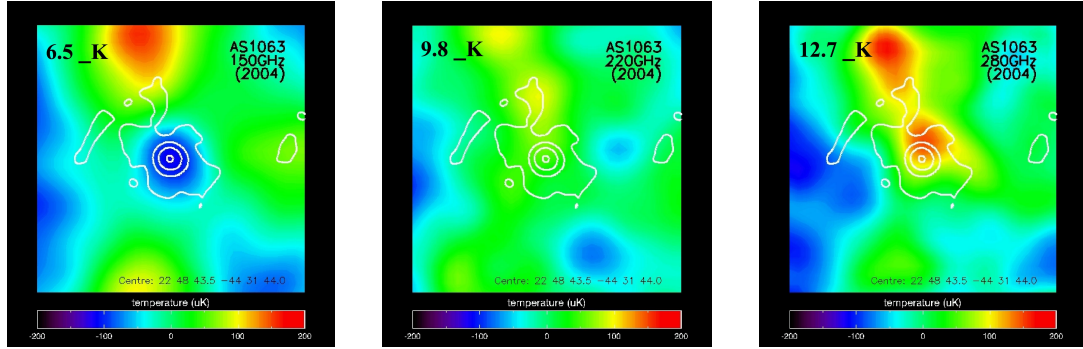
Figure 6.2: From the left to the right, maps of Abell S1063 at 150, 220 and 280 GHz made with ACBAR in 2004 (courtesy of L. Valkonen). The characteristic frequency spectrum of the SZE is clearly visible with a decrement at 150 GHz and increment at 280 GHz. The beam averaged error in μK is marked in the upper left corner of each map. The white contours mark the X-ray luminousity profile from Chandra. AS1063 is the second brightest cluster in the REFLEX sample with a X-ray luminousity of 30.79 10^{44} erg/s and is located at z=0.347.

to the ACBAR's large beam relative to a typical cluster radius (5' vs 1'), CMB confusion is a significant source of uncertainty, and only the most massive of clusters are expected to be detected ($M > 10^{15} M_{\circ}$). The observation strategy chosen for the CMB power spectrum measurement is quite similar to the optimal cluster detection observing strategy suggested by modeling of ACBAR's noise and beam size; a wide and shallow survey. The mass limit should be comparable for the new fields observed in 2004 and 2005, with considerably more sky. A cluster-searching analysis of the ACBAR data set is planned for the next year.

6.1.2 Pointed Cluster Observations

While SZE surveys have yet to bear fruit, a number experiments have detected the SZE when pointed at known clusters. The SZ effect in a galaxy cluster was first detected 1983. In addition to cosmological information, pointed SZE observations of galaxy clusters yield a unique window on the dynamics inside a galaxy cluster. ACBAR has made deep observations of 10 known X-ray clusters selected from the REFLEX cluster catalogue [4] and the Massive Cluster Survery (MACS; [19]) for the Viper Sunyaev-Zel'dovich Survey (VSZS). The VSZS is in the process of combining

Galaxy Clusters Observed by ACBAR

Name	Year Observed	RA	Dec	Detected at 150 GHz?	Redshift	X-ray Obs.
High-z Sample					$z > 0.25$	
1ES0657-56	2002	104.6296	-55.9469	Yes	0.296	XMM-Newton
AS 1063	2004	342.1812	-44.5289	Yes	0.347	Chandra
Low-z Sample					$z < 0.1$	
A3827	2002	330.4833	-59.9494	Yes		ROSAT
A3921	2005	342.4875	-62.4294	Yes		ROSAT
A3266	2004	67.8504	-61.4439	Yes		ROSAT
A3112	2004	49.4937	-44.2389	No		ROSAT
A3158	2005	55. 7246	-53.6353	No		ROSAT
A3667	2002	303.1271	-56.8319	No		ROSAT
RXJ0723	2005	110.8292	-73.4550	Yes		RASS
RXJ0549	2005	87.3329	-62.0869	Yes		RASS

Table 6.1: The ten galaxy clusters for which ACBAR measured SZE emission for part of the VSZS. Data is only available for the SZ decrement at 150 GHz for clusters observed in 2005.

weak lensing, SZE, and X-ray observations of all southern clusters. ACBAR provides millimeter maps of the SZE in these clusters below, at, and above the SZE null (at 150 GHz, 220 GHz, and 280 GHz, respectively). Weak lensing observations have been made with the 4m CTIO telescope in Chile. The galaxy clusters are tabulated in Table 6.1. Eight clusters are at low redshift ($z < 0.1$). The remainder are exceptional X-ray clusters at high redshift ($z > 0.25$): Abell S1063 is the second brightest cluster in the REFLEX catalogue and 1ES0657-56, the bullet cluster, is in the midst of a merging event. More details on these two clusters can be found in [79] and [78]. Interestingly, three of the low-z clusters do not show significant detections of the SZE at 150 GHz. The lack of signal is not due to contamination from radio point sources and CMB primary anisotropies. Further study into the causes of the reduced signal and its implications for SZ surveys is necessary.

The primary goals of the VSZS are to measure the Hubble Constant and to investigate empirically the importance of cluster physics on the SZE signal. Surveys of SZ clusters are a promising new cosmological probe, and several experiments seeking

Different Cluster Mass Derivations for 1ES0657-56

Data	Details	Mass ($\times 10^{15} M_\circ$)
X-ray M-T relation	Published	1.9
Lensing	Published	0.8
150 GHz only	Int Y, T_e from Y-T	?
150 GHz & X-ray Luminousity	Int Y, T_e from L_x-T	?
Multi-frequency ACBAR	Int Y, T_e from Y-T	?
Multi-frequency ACBAR & X-ray spectrum	Int Y, T_e from spectrum	?
	Int n_e, T_e from spectrum	?

Table 6.2: There are multiple ways to derive the mass of a galaxy cluster. A detailed comparison of each perturbation on the mass derivation can help deconstruct the causes of differences in the derived masses. This study is being conducted by L. Valkonen and will include other clusters when complete.

to exploit the SZE are either in-progress or planned for the near future (Bolocam, AMiBA, SZA, SPT, APEX, Planck). Improving our understanding of cluster physics will help reduce systematic biases in the constraints on cosmological parameters derived from the SZE. A number of paths to estimate the cluster masses will be compared as shown in Table 6.2 in order to understand the differences and biases in each method. Pointed cluster observations are needed to build a foundation of knowledge about the variability, systematics, and accuracy of mass reconstructions from the SZE. This study is being conducted by L. Valkonen, P. Gomez, and K. Romer.

6.2 Gravitational Lensing

General Relativity states that mass will deform the geometry of space and change the geodesics light follows. This was one of the first predictions of relativity to be experimentally confirmed by Eddington's starlight deflection measurements during the solar eclipse of 1919. In general, gravitational lensing occurs when a massive object bends the light from a more distant source and changes the source's apparent shape. Multiple images of the source may be seen in strong gravitional lensing. Lensing has been a rich field of study, probing mass scales from stars to galaxy clusters.

The deflection angle can be calculated from General Relativity to be the integral along the path

$$\alpha_\perp = -2 \int dx_\parallel \frac{d\Phi}{dx_\perp},$$

where $\frac{d\Phi}{dx_\perp}$ is the derivative of the gravitational potential in the deflection direction under the assumption that the potential is not varying in time. Given sufficiently precise measurements of the deflection angles, gravitational lensing can provide a robust and clean measurement of the integrated mass along a line of sight. It sidesteps the thorny and complicated problem of empirically estimating a galaxy cluster or other object's mass based on its measured optical flux.

In order to use the image shape deformations caused by gravitational lensing to reconstruct the mass distribution, it is necessary to know (at least statistically) the true shape of the lensed objects. The majority of gravitational lensing measurements to date have used lensed galaxies and stars: basically circular objects on average. The CMB temperature anisotropies will also be lensed by the large scale structure, rewriting the unlensed field as

$$T'(\widehat{n}) = T(\widehat{n} + d(\widehat{n})),$$

where T' is the lensed CMB field and d is the deflection angle. It is challenging to detect lensing of the CMB since the CMB is a gaussian random field, but the measurement is possible since lensing will change the statistical properties of the field.

The deflection power spectrum $C_\ell^{\Phi\Phi}$ describes the angular distribution of the lensing potential. The standard CMB Boltzmann codes (e.g. CMBFAST, CAMB) can provide theoretical predictions for the deflection power spectrum for a given set of cosmological parameters. Unsurprisingly, the deflection power spectrum is most sensitive to Ω_M. Gravitational lensing very slightly smoothes the acoustic peaks in the power spectrum and increases power in the damping tail. This effect is too small to be detectable in current experiments. The effects of lensing are more readily detectable in higher order statistics of the CMB field. There has been a vigorous theoretical

effort to develop optimal estimators and statistics to use to detect $C_\ell^{\Phi\Phi}$ [32, 29]. It is still a challenging measurement; these estimators require precise measurements of arcminute-scale anisotropies in order to detect degree-scale mass structures. Lensing also mixes E & B mode polarization, and several experiments should detect the lensed B-mode signal in the near future.

An possible first detection of the deflection power spectrum was reported recently by Smith et al. [71]. The authors of that work correlated the WMAP maps with radio galaxy counts from the NRAO VLA Sky Survey (NVSS) to find a 3.4 sigma detection of the deflection power spectrum. The ACBAR maps offer an independent route based only on the CMB to detect gravitational lensing at a similar significance level. The matter distribution can be probed by combining information about large-scale CMB anisotropies in the ACBAR fields from WMAP with ACBAR's measurements of small-scale anisotropies. The ACBAR side of the analysis is being driven by C. L. Kuo. While the detection is expected to be marginal ($\sim 3\sigma$ based on theoretical estimates in [32]), the ACBAR dataset will be an exciting proving ground for the algorithms being developed for next-generation experiments. A solid detection of gravitational lensing of the CMB will be a second confirmation of an important prediction of cosmology. With future survey experiments covering large swathes of sky with arcminute-scale beams, the lensing of the CMB anisotropies may open a new window on large scale structure in the universe.

6.3 Foregrounds: Radio sources, Dust and Dusty Galaxies

Foregrounds can potentially affect measurements of the CMB temperature anisotropies. There are three potential foregrounds at 150 GHz on ACBAR's angular scales: radio sources, dust, and dusty proto-galaxies. As an effectively single-frequency instrument, ACBAR depends on data from other experiments to construct foreground models. We use the methodology described in K04 to remove templates for radio sources and

dust emission from the CMB maps without making assumptions about their flux. We believe the residual foreground emission does not significantly impact the power spectrum for $\ell < 2400$.

We remove modes from the CMB maps corresponding to radio sources in the the 4.85 GHz Parkes-MIT-NRAO (PMN) survey [82]. Extra-galactic radio sources are expected to be less important at 150 GHz than at 30 GHz. The conversion factor from flux to temperature $(dB_\nu/dT_{CMB})^{-1}$ decreases as the frequency approaches the peak of the black body spectrum and is a factor of 15 smaller at 150 GHz than at 30 GHz. Of the 1601 PMN sources with a flux greater than 40 mJy in the ACBAR fields, we detected 37 sources including the guiding quasars at greater than 3σ. 2.2 false detections are expected with this detection threshold. The measurement errors are estimated from a set of 100 Monte-carlo realizations of the CMB+noise for each field. Table 6.3 lists the parameters of the detected PMN sources. Except for the detected sources, removing the PMN point sources does not significantly affect the bandpowers.

Estimating foreground contributions will be important for planning future CMB experiments. We compare the 150 GHz ACBAR point source number counts to the model in White and Majumdar [81] based on WMAP Q-band data.

$$\frac{dN}{dS_\nu} = \frac{80 \; deg^{-2}}{1 \; mJy} \left(\frac{S_\nu}{1 \; mJy} \right)^{-2.3}$$

Following the convention in that work, the spectral dependence of the fluxes is parameterized as $S_\nu \propto \nu^\beta$. The measured number counts in a logarithmic flux bin, n_B^{obs}, are compared to the predicted number counts for a given β, $n_B^{(\beta)} + n_B^{noise}$. Here, $n_B^{(\beta)}$ is the modeled number counts, and n_B^{noise} is the expected number of false detections due to ACBAR measurement error. The number counts are assumed to follow a Poissonian distribution. Sources with estimated measurement errors greater than 140 mJy are cut to reduce the n_B^{noise} term. The model number counts $n_B^{(\beta)}$ are scaled by $(N_{tot} - N_{cut})/N_{tot}$ to compensate. All other sources with measured amplitudes greater than 350 mJy are included in the calculation without consideration of the

signal-to-noise. We find $\beta = 0.16 \pm 0.16$. However, it is likely that this small sample is heavily biased towards sources with flat or rising spectra. We increase ACBAR's sensitivity to dimmer sources by binning all sources within a given PMN flux range, and look at the ratio of the average flux at 150 GHz to the average flux at 4.85 GHz within each bin. We find the ratio $(S_{150}/S_{4.85})$ increases with PMN flux from 0.07 below 400 mJy to 0.41 above 1600 mJy. This would be consistent with a two-population distribution in which the dimmer sources have a falling spectrum. We can estimate the band-power contributions from radio sources with this information. The estimate depends sensitively on the extrapolation of the 40 mJy flux cutoff in the PMN catalogue to 150 GHz. We assume a flux ratio of $S_{150}/S_{4.85} = 0.1$ for a cutoff at 4 mJy, which is conservative for the observed flux ratios of PMN sources with $S_{4.85} < 400$ mJy. Estimating the band-power contributions from radio sources with this spectral dependence results in an estimate of $\mathcal{D}_\ell \sim 2.2(\ell/2600)^2 \ \mu\text{K}^2$. At this level, the residual contribution from radio sources would be negligible in the ACBAR data.

The ACBAR fields are positioned in the "Southern Hole," a region of exceptionally low Galactic dust emission, in order to minimize the impact of dust (Figure 3.2). Finkbeiner et al. [20] (FDS99) constructed a multi-component dust model that predicts thermal emission at CMB frequencies from the combined observations of IRAS, COBE/DIRBE, and COBE/FIRAS. Taking into account the ACBAR filtering, the FDS99 model predicts an RMS dust signal at the μK level in the ACBAR fields, primarily on large angular scales. The ACBAR maps T can be decomposed as the sum of the CMB and dust signals $T_{CMB} + \xi T_{FDS}$. The parameter ξ quantifies the amplitude of the dust signal and is predicted to equal unity by the FSD99 model. The ACBAR maps are cross-correlated with the dust templates T_{FDS} to calculate the amplitude in each field. As with the radio sources, the same procedure is applied to 100 CMB+noise map realizations to estimate the scatter in the null case. The uncertainty in ξ is dominated by CMB fluctuations. The best-fit amplitude from combining all the fields is $\xi = 0.1 \pm 0.5$. The estimated amplitudes of the individual fields are shown in Figure 6.3. The χ^2 of the measured amplitudes ξ of the eight fields

Dust Amplitude in Each Field
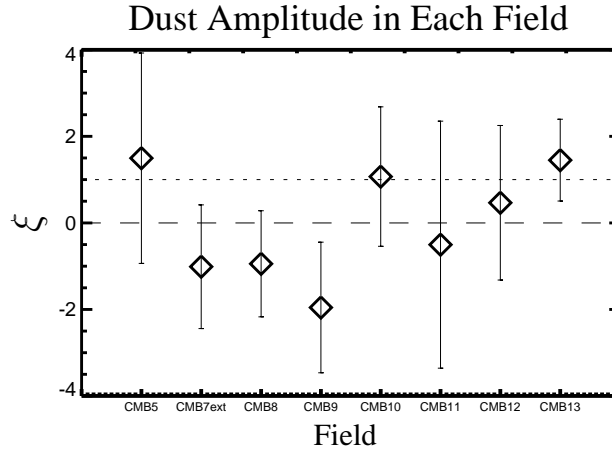
Figure 6.3: Dust emission is not detected in the ACBAR fields. Parametrizing the dust signal as $T_{CMB}+\xi T_{FDS}$, a suite of Monte-carlo realizations of maps of CMB and noise is used to estimate ξ. We find the upper limits in each field to be consistent with the FDS99 model ($\xi = 1$), but the data somewhat favor a lower dust amplitude. The reduced χ^2 of the measured amplitudes ξs is 0.75 under the assumption that $\langle\xi\rangle = 0$ (the dashed line). The reduced χ^2 for the FDS99 model with $\langle\xi\rangle = 1$ is 1.12 (the dotted line).

analyzed is 6.04 for the no-dust assumption of $\langle\xi\rangle = 0$ and increases to $\chi^2 = 8.97$ for the FDS99 model amplitude of $\langle\xi\rangle = 1$. The ACBAR data slightly favor a lower amplitude than predicted by the FDS99 model. The dust signal is not detectable in any of the ACBAR fields, and removing the dust template has a negligible impact on the measured power spectrum.

Dusty galaxies are a third and poorly constrained potential foreground in the ACBAR fields. This population of high-redshift, star-forming galaxies has been studied by several experiments at higher frequencies [16, 47, 48, 23]. However, as discussed in K07, extrapolating the expected signal to 150 GHz remains highly uncertain, and there remain significant uncertainties in the number counts $\frac{dN}{dF}$ and spatial clustering of the sources. The frequency dependence can be empirically determined by comparing the measured number counts in overlapping fields observed at different frequencies. This comparison has been done with MAMBO (1.2 mm) and SCUBA (850 μm), leading an spectral dependence of $S_\nu \propto \nu^{2.65}$ [23]. However, the Bolocam

data suggest a steeper source spectrum, as fewer sources are found at 1.1 mm [47, 48]. We estimate the spectral dependence to be $S_\nu \propto \nu^4$ from Figure 15 in Laurent et al. [47]. The uncertainty in the spectral dependence significantly affects the extrapolation of the flux of dusty galaxies to 150 GHz. We use estimates of the number counts from the SHADES survey [16] and Bolocam Lockman Hole Survery [48]. We apply the formulas in Scott and White [69] to estimate the expected power spectrum for the published number counts, ignoring the clustering terms. Scaling the results to 150 GHz with the MAMBO/SCUBA prescription of $S_\nu \propto \nu^{2.65}$ leads to an estimated contribution of $\mathcal{D}_\ell \sim 17 - 29(\ell/2600)^2 \ \mu K^2$. This level is comparable to the instrumental noise of ACBAR and might influence the interpretation of high-ℓ excess power. If we instead use the Bolocam/SCUBA scaling relationship, the estimated contribution is reduced by a factor of six to the negligible level of $\mathcal{D}_\ell \sim 2 - 6(\ell/2600)^2 \ \mu K^2$. For the results presented in this work, we tentatively assume that dusty protogalaxies do not contribute significant power at high-ℓ.

Source Name/Position	Field	$S_{4.85}$ (mJy)	S_{150} (mJy)	$\alpha_{150/4.85}$
PMN J0455-4616*°	CMB2	1653	2898 ± 60	0.16
PMN J0439-4522	CMB2	634	383 ± 73	-0.15
PMN J0451-4653	CMB2	541	360 ± 58	-0.12
PMN J0253-5441*°	CMB5	1193	1277 ± 63	0.02
PMN J0223-5347	CMB5	397	176 ± 28	-0.24
PMN J0229-5403	CMB5	242	147 ± 18	-0.14
PMN J0210-5101*°	CMB6	3198	1268 ± 86	-0.27
PMN J2207-5346°	CMB7ext	1410	381 ± 67	-0.38
PMN J2235-4835°	CMB7ext	1104	1529 ± 76	0.09
PMN J2239-5701°	CMB7ext	1063	501 ± 67	-0.22
PMN J2246-5607	CMB7ext	618	386 ± 49	-0.14
PMN J2309-5703	CMB7ext	56	257 ± 79	0.44
PMN J0519-4546a°	CMB8	15827	1393 ± 103	-0.92*
PMN J0519-4546b°	CMB8	14551	1163 ± 87	-0.92*
PMN J0538-4405*°	CMB8	4805	7209 ± 89	0.12
PMN J0515-4556°	CMB8	990	680 ± 98	-0.11
PMN J0526-4830	CMB8	425	82 ± 27	-0.48
PMN J0525-4318	CMB8	217	99 ± 27	-0.23
PMN J0531-4827	CMB8	142	96 ± 27	-0.11
PMN J2357-5311°	CMB9	1782	347 ± 50	-0.48
PMN J2336-5236	CMB9	1588	233 ± 56	-0.56
PMN J2334-5251	CMB9	557	432 ± 56	-0.07
PMN J0018-4929	CMB9	142	178 ± 56	0.07
PMN J0026-5244	CMB9	40	192 ± 63	0.46
PMN J0050-5738°	CMB10	1338	773 ± 104	-0.16
PMN J0058-5659°	CMB10	739	514 ± 60	-0.11
PMN J0133-5159°	CMB10	672	248 ± 63	-0.29
PMN J0124-5113°	CMB10	308	335 ± 49	0.02
PMN J2208-6404	CMB11	53	136 ± 44	0.27
PMN J0103-6438	CMB12	395	268 ± 63	-0.11
PMN J0144-6421	CMB12	152	184 ± 60	0.06
PMN J0303-6211°	CMB13	1862	429 ± 63	-0.43
PMN J0309-6058°	CMB13	1103	604 ± 81	-0.18
PMN J0251-6000	CMB13	433	189 ± 34	-0.24
PMN J0236-6136	CMB13	406	365 ± 35	-0.03
PMN J0257-6112	CMB13	178	104 ± 35	-0.16
PMN J0231-6036	CMB13	174	105 ± 35	-0.15

Table 6.3: These sources from the PMN 4.85 GHz catalog are detected at $> 3.0\sigma$ significance with ACBAR, corresponding to a false detection rate of 2.2. The fluxes at 4.85 GHz ($S_{4.85}$, from Wright et al. [82]) and 150 GHz (S_{150}, measured by ACBAR) are given. For ACBAR, the flux conversion factor is $1\mu K_{CMB} = 0.9 mJy$. The spectral index α is defined as $S_\nu \propto \nu^\alpha$. The uncertainties associated with S_{150} are dominated by the CMB fluctuations. The central guiding quasars (one in each of the 5 deeper fields) are marked with asterisks (*). These sources, as well as the undetected PMN sources, are projected out from the data using the methods described by K04 and do not contribute to the power spectrum measurements reported in this paper. The brightest sources are marked with circles (°) and are removed from the maps in a beam-independent method. Note that PMN J0519-4546a/b are within one beam width of each other and are not separately resolved by ACBAR. As a result, the listed α for PMN J0519-4546a/b is estimated from the sum of the fluxes at 4.85 GHz and

Chapter 7

Conclusion

We have measured the CMB angular power spectrum using the complete data set from the 2001, 2002, and 2005 ACBAR 150 GHz observations. ACBAR dedicated 85k detector-hours to CMB observations at 150 GHz and covered 1.7% of the sky. We calibrate the data by comparing the magnitude of CMB temperature anisotropies in the largest ACBAR fields with WMAP3 temperature maps. The new calibration is found to be consistent with the previous planet-based (K04) and RCW38-based (K07) calibrations, but with uncertainty reduced from 10% and 6.0% (respectively) to 2.3% in temperature.

The ACBAR band-powers span multipoles from 350 to 3000 and are currently the most precise measurement of the temperature anisotropies for $\ell > 900$. The third, fourth and fifth acoustic peaks are detected, and the damping tail of the anisotropies is mapped out. Cosmological parameter estimation using data from ACBAR and other experiments is ongoing and should be complete in the near future. The preliminary runs indicate that the ACBAR band-powers are consistent with a spatially flat, dark energy-dominated ΛCDM cosmology and favor only slight changes to the WMAP3 best-fit parameters. There is a small excess of power at small angular scales which may be due to the SZ effect, although other foregrounds can not be ruled out.

The next major stride forward in studying the CMB TT anisotropies is likely to come from Planck. Planck is the next CMB satellite experiment and is slated to launch in 2008. Extracting strong parameter constraints from the full power spectrum requires fully resolving the acoustic peaks and maintaining a stringent calibration

across all angular scales of interest. Planck should do this very well, resulting in an order of magnitude reduction in the allowed parameter space.

Many other experiments are in progress or planned to study polarization in the CMB, secondary anisotropies, the growth of structure, and the equation of state of dark energy. There is a tremendous interest in learning more about the mysterious dark energy and the driving forces of inflation. Studies of the dark constituents of the universe are likely to remain defining questions in cosmology and particle physics for decades to come.

Bibliography

[1] D. Barkats, C. Bischoff, P. Farese, L. Fitzpatrick, T. Gaier, J. O. Gundersen, M. M. Hedman, L. Hyatt, J. J. McMahon, D. Samtleben, S. T. Staggs, K. Vanderlinde, and B. Winstein. First Measurements of the Polarization of the Cosmic Microwave Background Radiation at Small Angular Scales from CAPMAP. *ApJ*, 619:L127–L130, February 2005.

[2] Jeremy Bernstein and Scott Dodelson. Aspects of the zel'dovich-sunyaev mechanism. *Phys. Rev. D*, 41(2):354–373, Jan 1990.

[3] R. S. Bhatia, S. T. Chase, S. F. Edgington, J. Glenn, W. C. Jones, A. E. Lange, B. Maffei, A. K. Mainzer, P. D. Mauskopf, B. J. Philhour, and B. K. Rownd. A three-stage helium sorption refrigerator for cooling of infrared detectors to 280 mK. *Cryogenics*, 40:685–691, 2000.

[4] H. Bohringer, L. Guzzo, C. A. Collins, D. M. Neumann, S. Schindler, P. Schuecker, R. Cruddace, G. Chincarini, S. de Grandi, A. C. Edge, H. T. MacGillivray, P. Shaver, G. Vettolani, and W. Voges. Results from the RE-FLEX Cluster Survey. In S. Colombi, Y. Mellier, and B. Raban, editors, *Wide Field Surveys in Cosmology, 14th IAP meeting held May 26-30, 1998, Paris. Publisher: Editions Frontieres. ISBN: 2-8 6332-241-9, p. 261.*, pages 261–+, 1998.

[5] J. R. Bond, C. R. Contaldi, U.-L. Pen, D. Pogosyan, S. Prunet, M. I. Ruetalo, J. W. Wadsley, B. S. Zhang, P.and Mason, S. T. Myers, T. J. Pearson, A. C. S. Readhead, J. L. Sievers, and P. S. Udomprasert. The Sunyaev-Zeldovich effect in

CMB-calibrated theories applied to the Cosmic Background Imager anisotropy power at $\ell > 2000$. *ApJ*, 626:12, 2005.

[6] J. R. Bond, A. H. Jaffe, and L. Knox. Estimating the power spectrum of the cosmic microwave background. *Phys. Rev. D*, 57:2117–2137, February 1998.

[7] J. R. Bond, A. H. Jaffe, and L. Knox. Radical Compression of Cosmic Microwave Background Data. *ApJ*, 533:19–37, April 2000.

[8] R. H. Brown and R. Q. Twiss. A Test of a New Type of Stellar Interferometer on Sirius. *Nature (London)*, 178:1046–, 1956.

[9] R. H. Brown and R. Q. Twiss. Interferometry of the Intensity Fluctuations in Light. I. Basic Theory: The Correlation Between Photons in Coherent Beams of Light. *Royal Society of London Proceedings Series A*, 242:300–, 1957.

[10] R. H. Brown and R. Q. Twiss. Interferometry of the Intensity Fluctuations in Light. II. An Experimental Test of the Theory for Partially Coherent Light. *Royal Society of London Proceedings Series A*, 243:291–, 1958.

[11] E. F. Bunn and M. White. The 4 Year COBE Normalization and Large-Scale Structure. *ApJ*, 480:6–+, May 1997.

[12] R. S. Bussmann, W. L. Holzapfel, and C. L. Kuo. Millimeter Wavelength Brightness Fluctuations of the Atmosphere above the South Pole. *ApJ*, 622:1343–1355, April 2005.

[13] C. R. Contaldi. private communication, 2007.

[14] A. Cooray, W. Hu, and M. Tegmark. Large-Scale Sunyaev-Zeldovich Effect: Measuring Statistical Properties with Multifrequency Maps. *ApJ*, 540:1–13, September 2000.

[15] A. Cooray and A. Melchiorri. Small angular scale CMB anisotropies from CBI and BIMA experiments: Early universe or local structures? *Phys. Rev. D*, 66 (8):083001–+, October 2002.

[16] K. Coppin, E. L. Chapin, A. M. J. Mortier, S. E. Scott, C. Borys, J. S. Dunlop, M. Halpern, D. H. Hughes, A. Pope, D. Scott, S. Serjeant, J. Wagg, D. M. Alexander, O. Almaini, I. Aretxaga, T. Babbedge, P. N. Best, A. Blain, S. Chapman, D. L. Clements, M. Crawford, L. Dunne, S. A. Eales, A. C. Edge, D. Farrah, E. Gaztañaga, W. K. Gear, G. L. Granato, T. R. Greve, M. Fox, R. J. Ivison, M. J. Jarvis, T. Jenness, C. Lacey, K. Lepage, R. G. Mann, G. Marsden, A. Martinez-Sansigre, S. Oliver, M. J. Page, J. A. Peacock, C. P. Pearson, W. J. Percival, R. S. Priddey, S. Rawlings, M. Rowan-Robinson, R. S. Savage, M. Seigar, K. Sekiguchi, L. Silva, C. Simpson, I. Smail, J. A. Stevens, T. Takagi, M. Vaccari, E. van Kampen, and C. J. Willott. The SCUBA Half-Degree Extragalactic Survey - II. Submillimetre maps, catalogue and number counts. *MNRAS*, 372:1621–1652, November 2006.

[17] S. Dodelson. *Modern Cosmology.* Elsevier Science (USA), 2003.

[18] J. L. Dotson, G. Novak, T. Renbarger, D. Pernic, and J. L. Sundwall. SPARO: the submillimeter polarimeter for Antarctic remote observing. In T. G. Phillips, editor, *Proc. SPIE Vol. 3357, p. 543-547, Advanced Technology MMW, Radio, and Terahertz Telescopes, Thomas G. Phillips; Ed.*, volume 3357 of *Presented at the Society of Photo-Optical Instrumentation Engineers (SPIE) Conference*, pages 543–547, July 1998.

[19] H. Ebeling, A. C. Edge, and J. P. Henry. MACS: A Quest for the Most Massive Galaxy Clusters in the Universe. *ApJ*, 553:668–676, June 2001.

[20] D.P̃. Finkbeiner, M. Davis, and D.J̃. Schlegel. Extrapolation of galactic dust emission at 100 microns to cosmic microwave background radiation frequencies using firas. *ApJ*, 524:867–886, October 1999.

[21] K. Ganga. private communication, 2007.

[22] P. Gomez, A. K. Romer, J. B. Peterson, W. Chase, M. Runyan, W. Holzapfel, C. L. Kuo, M. Newcomb, J. Ruhl, J. Goldstein, and A. Lange. Sunyaev-Zeldovich

Observations of Massive Clusters of Galaxies. In G. Bertin, D. Farina, and R. Pozzoli, editors, *Plasmas in the Laboratory and in the Universe: New Insights and New Challenges*, volume 703 of *American Institute of Physics Conference Series*, pages 361–366, April 2004.

[23] T. R. Greve, R. J. Ivison, F. Bertoldi, J. A. Stevens, J. S. Dunlop, D. Lutz, and C. L. Carilli. A 1200-μm MAMBO survey of ELAISN2 and the Lockman Hole - I. Maps, sources and number counts. *MNRAS*, 354:779–797, November 2004.

[24] M. J. Griffin and M. J. Holland. The influence of background power on the performance of an ideal bolometer. *International Journal of Infrared and Millimeter Waves*, 9(6):861–, 1988.

[25] L. M. Griffiths, M. Kunz, and J. Silk. A possible contribution to CMB anisotropies at high l from primordial voids. *MNRAS*, 339:680–684, March 2003.

[26] E. Grossman. *AT User's Manual*. Airhead Software, Boulder, CO 80302, 1989.

[27] A. J. S. Hamilton and M. Tegmark. Decorrelating the power spectrum of galaxies. *MNRAS*, 312:285–294, February 2000.

[28] G. Hinshaw, D. N. Spergel, L. Verde, R. S. Hill, S. S. Meyer, C. Barnes, C. L. Bennett, M. Halpern, N. Jarosik, A. Kogut, E. Komatsu, M. Limon, L. Page, G. S. Tucker, J. L. Weiland, E. Wollack, and E. L. Wright. Three-Year Wilkinson Microwave Anisotropy Probe (WMAP) Observations: Temperature Analysis. */apj, submitted*, 2006. "astro-ph/0603451".

[29] C. M. Hirata and U. Seljak. Analyzing weak lensing of the cosmic microwave background using the likelihood function. *Phys. Rev. D*, 67(4):043001–+, February 2003.

[30] E. Hivon, K. M. Górski, C. B. Netterfield, B. P. Crill, S. Prunet, and F. Hansen. MASTER of the Cosmic Microwave Background Anisotropy Power Spectrum: A Fast Method for Statistical Analysis of Large and Complex Cosmic Microwave Background Data Sets. *ApJ*, 567:2–17, March 2002.

[31] D. W. Hogg. Distance measures in cosmology. *ArXiv Astrophysics e-prints*, May 1999.

[32] W. Hu. Mapping the Dark Matter through the Cosmic Microwave Background Damping Tail. *ApJ*, 557:L79–L83, August 2001.

[33] W. C. Jones. *A Measurement of the temperature and polarization anisotropies of the cosmic microwave background radiation.* PhD thesis, California Institute of Technology, 2005.

[34] W. C. Jones. *A Measurement of Temperature and Polarization Anisotropies in the Cosmic Microwave Background Radiation.* PhD thesis, California Institute of Technology, 2005.

[35] L. Knox. Determination of inflationary observables by cosmic microwave background anisotropy experiments. *Phys. Rev. D*, 52:4307–4318, October 1995.

[36] L. Knox. Cosmic microwave background anisotropy window functions revisited. *Phys. Rev. D*, 60:103516, 1999. astro-ph/9902046.

[37] E. Komatsu and U. Seljak. The Sunyaev-Zel'dovich angular power spectrum as a probe of cosmological parameters. *MNRAS*, 336:1256–1270, November 2002.

[38] A. Kosowsky. The Atacama Cosmology Telescope. *New Astronomy Review*, 47: 939–943, December 2003.

[39] J. M. Kovac. private communication, 2007.

[40] J. M. Kovac, E. M. Leitch, C. Pryke, J. E. Carlstrom, N. W. Halverson, and W. L. Holzapfel. Detection of polarization in the cosmic microwave background using DASI. *Nature*, 420:772–787, December 2002.

[41] C. L. Kuo. *High Resolution Observations of the CMB Power Spectrum with ACBAR.* PhD thesis, University of California, Berkeley, 2003.

[42] C. L. Kuo, P. A. R. Ade, J. J. Bock, J. R. Bond, C. R. Contaldi, M. D. Daub, J. H. Goldstein, W. L. Holzapfel, A. E. Lange, M. Lueker, M. Newcomb, J. B. Peterson, C. Reichardt, J. Ruhl, M. C. Runyan, and Z. Staniszweski. Improved Measurements of the CMB Power Spectrum with ACBAR. *ApJ*, 664:687–701, August 2007.

[43] C. L. Kuo, P. A. R. Ade, J. J. Bock, C. Cantalupo, M. D. Daub, J. Goldstein, W. L. Holzapfel, A. E. Lange, M. Lueker, M. Newcomb, J. B. Peterson, J. E. Ruhl, M. C. Runyan, and E. Torbet. High-resolution observations of the cosmic microwave background power spectrum with acbar. *ApJ*, 600:32–51, January 2004.

[44] C. L. Kuo, J. J. Bock, M. D. Daub, J.H. Goldstein, W. L. Holzapfel, A. E. Lange, M. Newcomb, J. B. Peterson, J. Ruhl, M. C. Runyan, and E. Torbet. First CMB Power Spectrum Results from ACBAR. *In Preperation*, 2002.

[45] J. M. Lamarre. Photon noise in photometric instruments at far-infrared and submillimeter wavelengths. *Appl. Opt.*, 25:870–876, 1986.

[46] A. P. Lane. Submillimeter Transmission at South Pole. In G. Novak and R. H. Landsberg, editors, *Astrophysics from Antarctica (ASP Conf. Proc., vol. 141)*, page 289, 1998.

[47] G. T. Laurent, J. E. Aguirre, J. Glenn, P. A. R. Ade, J. J. Bock, S. F. Edgington, A. Goldin, S. R. Golwala, D. Haig, A. E. Lange, P. R. Maloney, P. D. Mauskopf, H. Nguyen, P. Rossinot, J. Sayers, and P. Stover. The Bolocam Lockman Hole Millimeter-Wave Galaxy Survey: Galaxy Candidates and Number Counts. *ApJ*, 623:742–762, April 2005.

[48] P. R. Maloney, J. Glenn, J. E. Aguirre, S. R. Golwala, G. T. Laurent, P. A. R. Ade, J. J. Bock, S. F. Edgington, A. Goldin, D. Haig, A. E. Lange, P. D. Mauskopf, H. Nguyen, P. Rossinot, J. Sayers, and P. Stover. A Fluctuation

Analysis of the Bolocam 1.1 mm Lockman Hole Survey. *ApJ*, 635:1044–1052, December 2005.

[49] S Masi, P Ade, J Bock, J Bond, J Borrill, A Boscaleri, P Cabella, C Contaldi, B Crill, P de Bernardis, G De Gasperis, A de Oliveira-Costa, G De Troia, G Di Stefano, E Hivon, A Jaffe, W. C. Jones, T Kisner, A Lange, C MacTavish, P Mauskopf, A Melchiorri, T Montroy, P Natoli, B Netterfield, E Pascale, F Piacentini, D Pogosyan, G Polenta, S Prunet, S Ricciardi, G Romeo, J Ruhl, P Santini, M Tegmark, M Veneziani, and N Vittorio. Instrument, Method, Brightness and Polarization Maps from the 2003 Flight of Boomerang. *A&A*, 458:687–716, November 2006.

[50] B. S. Mason, T. J. Pearson, A. C. S. Readhead, M. C. Shepherd, J. Sievers, P. S. Udomprasert, J. K. Cartwright, A. J. Farmer, S. Padin, S. T. Myers, J. R. Bond, C. R. Contaldi, U. Pen, S. Prunet, D. Pogosyan, J. E. Carlstrom, J. Kovac, E. M. Leitch, C. Pryke, N. W. Halverson, W. L. Holzapfel, P. Altamirano, L. Bronfman, S. Casassus, J. May, and M. Joy. The Anisotropy of the Microwave Background to l = 3500: Deep Field Observations with the Cosmic Background Imager. *ApJ*, 591:540–555, July 2003.

[51] J. C. Mather. Bolometer noise: nonequilibrium theory. *Applied optics*, 21(6): 1125–, 1982.

[52] P. D. Mauskopf, J. J. Bock, H. Del Castillo, and A. E. Holzapfel, W. l. Lange. Composite infrared bolometers with Si3N4 micromesh absorbers. *Appl. Opt.*, 36: 765–771, 1997.

[53] G. Novak, D. T. Chuss, T. Renbarger, G. S. Griffin, M. G. Newcomb, J. B. Peterson, R. F. Loewenstein, D. Pernic, and J. L. Dotson. First Results from the Submillimeter Polarimeter for Antarctic Remote Observations: Evidence of Large-Scale Toroidal Magnetic Fields in the Galactic Center. *ApJ*, 583:L83–L86, February 2003.

[54] L. Page, G. Hinshaw, E. Komatsu, M. R. Nolta, D. N. Spergel, C. L. Bennett, C. Barnes, R. Bean, O. Doré, J. Dunkley, M. Halpern, R. S. Hill, N. Jarosik, A. Kogut, M. Limon, S. S. Meyer, N. Odegard, H. V. Peiris, G. S. Tucker, L. Verde, J. L. Weiland, E. Wollack, and E. L. Wright. Three-Year Wilkinson Microwave Anisotropy Probe (WMAP) Observations: Polarization Analysis. *ApJS*, 170:335–376, June 2007.

[55] J. R. Pardo, J. Cernicharo, and E. Serabyn. Atmospheric transmission at microwaves (ATM): an improved model formillimeter/submillimeter applications. *Antennas and Propagation, IEEE Transactions on*, 49:1683–1694, December 2001.

[56] J. B. Peterson, G. S. Griffin, M. G. Newcomb, D. L. Alvarez, C. M. Cantalupo, D. Morgan, K. W. Miller, K. Ganga, D. Pernic, and M. Thoma. First Results from Viper: Detection of Small-scale Anisotropy at 40 GHZ. *ApJ*, 532:L83–L86, April 2000.

[57] F. Piacentini, P. A. R. Ade, J. J. Bock, J. R. Bond, J. Borrill, A. Boscaleri, P. Cabella, C. R. Contaldi, B. P. Crill, P. de Bernardis, G. De Gasperis, A. de Oliveira-Costa, G. De Troia, G. di Stefano, E. Hivon, A. H. Jaffe, T. S. Kisner, W. C. Jones, A. E. Lange, S. Masi, P. D. Mauskopf, C. J. MacTavish, A. Melchiorri, T. E. Montroy, P. Natoli, C. B. Netterfield, E. Pascale, D. Pogosyan, G. Polenta, S. Prunet, S. Ricciardi, G. Romeo, J. E. Ruhl, P. Santini, M. Tegmark, M. Veneziani, and N. Vittorio. A Measurement of the Polarization-Temperature Angular Cross-Power Spectrum of the Cosmic Microwave Background from the 2003 Flight of BOOMERANG. *ApJ*, 647:833–839, August 2006.

[58] S. Radford. Site Characterization for mm/submm Astronomy (Invited Speaker). In J. Vernin, Z. Benkhaldoun, and C. Muñoz-Tuñón, editors, *Astronomical Site Evaluation in the Visible and Radio Range*, volume 266 of *Astronomical Society of the Pacific Conference Series*, pages 148–+, 2002.

[59] A. C. S. Readhead, B. S. Mason, C. R. Contaldi, T. J. Pearson, J. R. Bond, S. T.

Myers, S. Padin, J. L. Sievers, J. K. Cartwright, M. C. Shepherd, D. Pogosyan, S. Prunet, P. Altamirano, R. Bustos, L. Bronfman, S. Casassus, W. L. Holzapfel, J. May, U.-L. Pen, S. Torres, and P. S. Udomprasert. Extended Mosaic Observations with the Cosmic Background Imager. *ApJ*, 609:498–512, July 2004.

[60] A. C. S. Readhead, S. T. Myers, T. J. Pearson, J. L. Sievers, B. S. Mason, C. R. Contaldi, J. R. Bond, R. Bustos, P. Altamirano, C. Achermann, L. Bronfman, J. E. Carlstrom, J. K. Cartwright, S. Casassus, C. Dickinson, W. L. Holzapfel, J. M. Kovac, E. M. Leitch, J. May, S. Padin, D. Pogosyan, M. Pospieszalski, C. Pryke, R. Reeves, M. C. Shepherd, and S. Torres. Polarization Observations with the Cosmic Background Imager. *Science*, 306:836–844, October 2004.

[61] T. Renbarger, D. T. Chuss, J. L. Dotson, G. S. Griffin, J. L. Hanna, R. F. Loewenstein, P. S. Malhotra, J. L. Marshall, G. Novak, and R. J. Pernic. Early Results from SPARO: Instrument Characterization and Polarimetry of NGC 6334. *PASP*, 116:415–424, May 2004.

[62] A. K. Romer and et al. Imaging the Sunyaev-Zel'dovich Effect using ACBAR on Viper. In J. S. Mulchaey, A. Dressler, and A. Oemler, editors, *Clusters of Galaxies: Probes of Cosmological Structure and Galaxy Evolution*, 2004.

[63] J. Ruhl, P. A. R. Ade, J. E. Carlstrom, H.-M. Cho, T. Crawford, M. Dobbs, C. H. Greer, N. w. Halverson, W. L. Holzapfel, T. M. Lanting, A. T. Lee, E. M. Leitch, J. Leong, W. Lu, M. Lueker, J. Mehl, S. S. Meyer, J. J. Mohr, S. Padin, T. Plagge, C. Pryke, M. C. Runyan, D. Schwan, M. K. Sharp, H. Spieler, Z. Staniszewski, and A. A. Stark. The South Pole Telescope. In C. M. Bradford, P. A. R. Ade, J. E. Aguirre, J. J. Bock, M. Dragovan, L. Duband, L. Earle, J. Glenn, H. Matsuhara, B. J. Naylor, H. T. Nguyen, M. Yun, and J. Zmuidzinas, editors, *Millimeter and Submillimeter Detectors for Astronomy II. Edited by Jonas Zmuidzinas, Wayne S. Holland and Stafford Withington Proceedings of the SPIE, Volume 5498, pp. 11-29 (2004).*, volume 5498 of *Presented at the Society of Photo-Optical Instrumentation Engineers (SPIE) Conference*, pages 11–29, October 2004.

[64] M. C. Runyan. *A Search for Galaxy Clusters Using the Sunyaev Zel'dovich Effect*. PhD thesis, California Institute of Technology, 2002.

[65] M. C. Runyan, P. A. R. Ade, R. S. Bhatia, J. J. Bock, M. D. Daub, J. H. Goldstein, C. V. Haynes, W. L. Holzapfel, C. L. Kuo, A. E. Lange, J. Leong, M. Lueker, M. Newcomb, J. B. Peterson, C. Reichardt, J. Ruhl, G. Sirbi, E. Torbet, C. Tucker, A. D. Turner, and D. Woolsey. ACBAR: The Arcminute Cosmology Bolometer Array Receiver. *ApJS*, 149:265–287, December 2003.

[66] M. C. Runyan, P. A. R. Ade, J. J. Bock, C. Cantalupo, M. D. Daub, J. H. Goldstein, P. Gomez, W. L. Holzapfel, C. L. Kuo, A. E. Lange, M. Lueker, M. Newcomb, J. B. Peterson, A. K. Romer, J. Ruhl, and E. Torbet. A Search for Distant SZ Galazy Clusters with ACBAR. *In Preparation*, 2003.

[67] R. H. Sanders. Observational Cosmology. In K. Tamvakis, editor, *The Physics of the Early Universe*, volume 653 of *Lecture Notes in Physics, Berlin Springer Verlag*, pages 105–+, 2005.

[68] D. J. Schlegel, D. P. Finkbeiner, and M. Davis. Maps of Dust Infrared Emission for Use in Estimation of Reddening and Cosmic Microwave Background Radiation Foregrounds. *ApJ*, 500:525–+, June 1998.

[69] D. Scott and M. White. Implications of SCUBA observations for the Planck Surveyor. *A&A*, 346:1–6, June 1999.

[70] U. Seljak, N. Sugiyama, M. White, and M. Zaldarriaga. Comparison of cosmological Boltzmann codes: Are we ready for high precision cosmology? *Phys. Rev. D*, 68(8):083507–+, October 2003.

[71] K. M. Smith, O. Zahn, and O. Doré. Detection of gravitational lensing in the cosmic microwave background. *Phys. Rev. D*, 76(4):043510–+, August 2007.

[72] K. Subramanian, T. R. Seshadri, and J. D. Barrow. Small-scale cosmic microwave background polarization anisotropies due to tangled primordial magnetic fields. *MNRAS*, 344:L31–L35, September 2003.

[73] R. V. Sudiwala, M. J. Griffin, and A. L. Woodcraft. Thermal modeling and characterization of semiconductor bolometers. *International Journal of Infrared and Millimeter Waves*, 23(4):545–573, 2002.

[74] I. Szapudi, S. Prunet, D. Pogosyan, A. S. Szalay, and J. R. Bond. Fast CMB Analyses via Correlation Functions. *ArXiv Astrophysics e-prints*, October 2000.

[75] M. Tegmark. CMB mapping experiments: A designer's guide. *Phys. Rev. D*, 56: 4514–4529, October 1997.

[76] M. Tegmark. How to measure cmb power spectra without losing information. *Phys. Rev. D*, 55:5895–5907, May 1997.

[77] M. Tristram, J. F. Macías-Pérez, C. Renault, and D. Santos. XSPECT, estimation of the angular power spectrum by computing cross-power spectra with analytical error bars. *MNRAS*, 358:833–842, April 2005.

[78] L. E. Valkonen and ACBAR collaboration. Multi-wavelength observations of the bullet cluster: A joint Sunyaev-Zel'dovich effect and x-ray analysis. *In preparation*, 2007.

[79] L. E. Valkonen, K. Sabirli, A. K. Romer, and ACBAR Collaboration. Multi-wavelength observations of the bullet cluster: A joint Sunyaev-Zel'dovich effect and x-ray analysis. *In Preparation*, 2007.

[80] M. White, L. Hernquist, and V. Springel. Simulating the Sunyaev-Zeldovich Effect(s): Including Radiative Cooling and Energy Injection by Galactic Winds. *ApJ*, 579:16–22, November 2002.

[81] M. White and S. Majumdar. Point Sources in the Context of Future SZ Surveys. *ApJ*, 602:565–570, February 2004.

[82] A.Ẽ. Wright, M.R̃. Griffith, B.F̃. Burke, and R.D̃. Ekers. The parkes-mit-nrao (pmn) surveys. 2: Source catalog for the southern survey (delta greater than -87.5 deg and less than -37 deg). *ApJS*, 91:111–308, March 1994.

[83] Y. Yamada, A. Mitsuishi, and H. Yoshinaga. Transmission filters in the far-infrared region. *J. Opt. Soc. Am.*, 52:17–19, 1962.

Appendix A

Bolometer Characterization

A number of papers have developed the physical model of bolometers [51, 24, 73]. In particular, I recommend the appendix of Jones [33] for an extremely good review of bolometer physics and the practicalities involved in determining model parameters from experimental data. Given the excellent existing sources for this material, this section includes only a short reference list of the relevant equations. A schematic view of a bolometer is shown in Figure A.
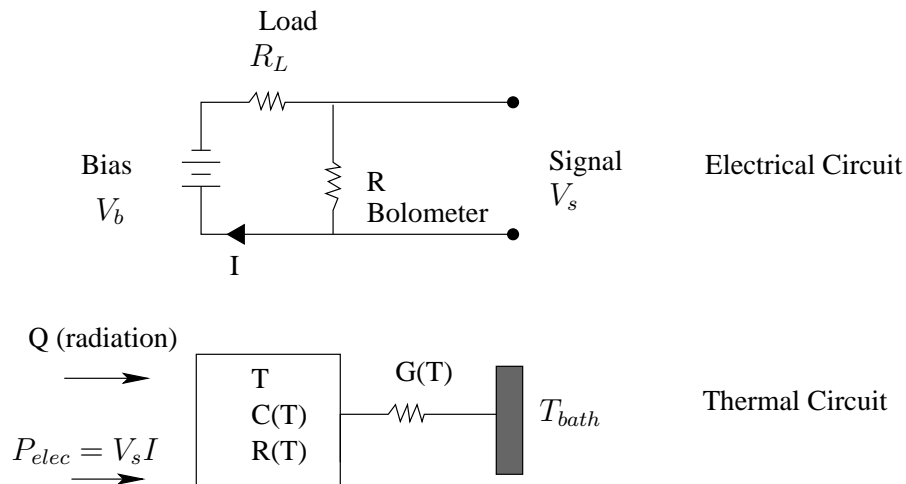
Figure A.1: A schematic view of a bolometer's thermal and electrical circuits. The bolometer voltage, V_s, is amplified and stored to disk.

Useful equations and definitions:

- R(T), or R, is the resistance of the bolometer at temperature T. The resistance is dominated by the NTD germanium thermistor. The resistance of these thermistors exponentially depends on temperature, varying as

$$R(T) = R_0 e^{-\left(\frac{\Delta}{T}\right)^\alpha - \frac{\lambda(T)}{L}\frac{eV}{kT}} = R_0 e^{-\sqrt{\frac{41.8K}{T}}}$$

  where $\Delta = 41.8$ and $\alpha = 0.5$ are the values for the ACBAR thermistors. The second term in the exponent related to the electric field effect is generally negligible for NTD thermistors at 300 mK at the operating voltages. R_0 must be experimentally determined for each chip.

- R_L is the load resistance in series with the bolometer. As $R_L \gg R(T)$, the bolometer is quasi-current biased. $R_L = 60 \ M\Omega$ for ACBAR.

- V_b is the applied bias voltage and should be chosen to maximize the bolometer's sensitivity. $I = V_b/(R_L + R)$ is the bias current.

- V_s is the measured signal voltage across the bolometer. $V_s = IR = V_b \frac{R}{R_L+R}$.

- T is the bolometer temperature. The unit-less equivalent is $\phi = (T/T_0)$. $T_0 = 0.3$ K in this work.

- Q is the absorbed optical power.

- $P_{elec} = IV_s$ is the electrical power.

- C(T) is the heat capacity of the bolometer at operating temperature.

- G(T) is the dynamic thermal conductance to the bolometer. Its temperature dependence can be parametrized as

$$G(T) = G_0(\phi)^\beta$$

. Other authors [73] instead parametrize the thermal conductivity, k, of the link as a power law, arguing that this is more physically motivated. Both models fit the bolometer lab data well, but the first expression is used in this work.

- Power Balance in equilibrium: $Q + P_{elec} = \int G(T) dT$

- The effective thermal conductance combines the dynamic thermal conductance with the results of electro-thermal feedback.

$$G_{eff} = G(T) + I^2 \left| \frac{\partial R}{\partial T} \right| \left(1 - \frac{2R}{(R_L + R)} \right)$$

- The dynamic impedance of the bolometer will be:

$$z = R \frac{\left(G(T) + I^2 \frac{dR}{dT} \right)}{\left(G(T) - I^2 \frac{dR}{dT} \right)}$$

- The responsivity $S(\omega) \equiv \left\langle \frac{\delta V_s}{\delta Q} \right\rangle$ is the frequency-dependent voltage response to a small optical signal and can be written as

$$S(\omega) = -\frac{1}{\sqrt{1 + (\omega\tau)^2}} \frac{1}{G_{eff}} \frac{R}{2T} \sqrt{\frac{\Delta}{T}} \frac{V_b}{(R_L + R)} \left(1 - \frac{R}{(R_L + R)} \right)$$

For the simple thermal model in this Appendix, a bolometer will behave like a single-pole filter with $\tau \equiv \frac{C(t)}{G_{eff}}$. The single-pole model has been incorporated into the above equation. For some bolometers, the actual frequency response will be more complex and include second or third time constants.

Appendix B

The ACBAR CMB Fields

These are the CMB maps of the ACBAR fields derived from the 2001, 2002 and 2005 observing seasons that went into the band-powers reported in §5. These maps are the high S/N maps discussed in §4. The foreground templates have been projected out. The blank squares in some fields mark the quasar masking. The anisotropic filtering and weighting contributes to the visible directionality of structures. Each map is shown in μK in ACBAR temperature units. The overall calibration factor to go to an absolute temperature scale has not been applied. The absolute correction factor would multiply the maps by -1.060 ± 1.024.

Each map is plotted in flat-sky coordinates. The left and bottom axes are marked with the flat-sky coordinates in degrees. The top and right axes are labeled with the RA and declination respectively in degrees.
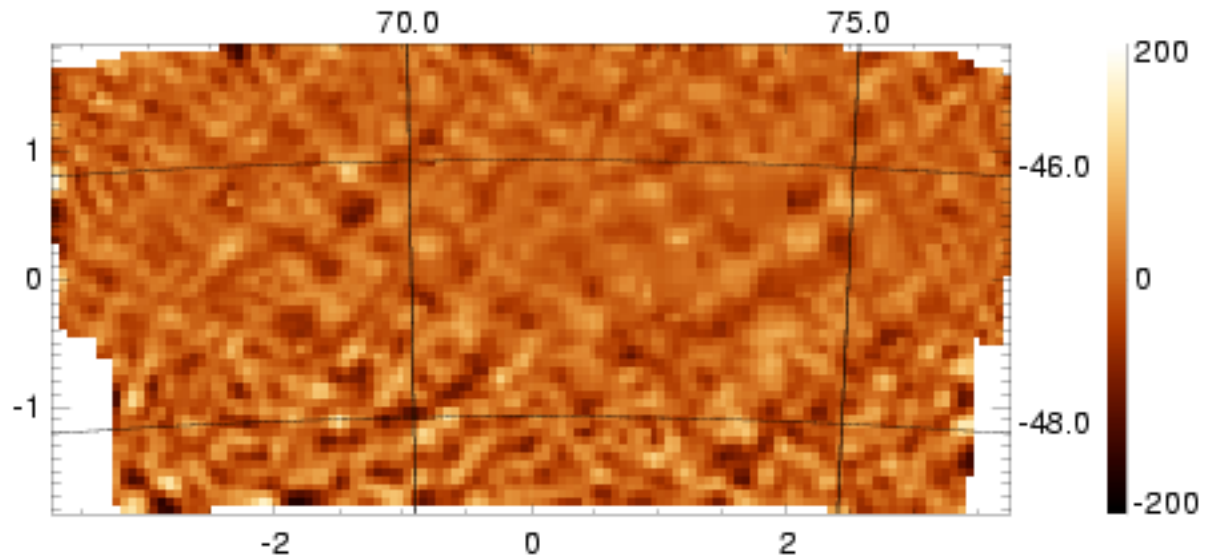
Figure B.1: Map of CMB2(CMB4), a shallow field observed in 2001 and 2002. Excess optical loading reduced the detector sensitivities in 2001 and the portion of the map observed in 2001 only is noticeably more noisy. We initially tried to calibrate the second ACBAR release by comparing this field to B98 and B03 maps. It is not in the B03 deep region so the depth is similar between the two BOOMERANG flights.
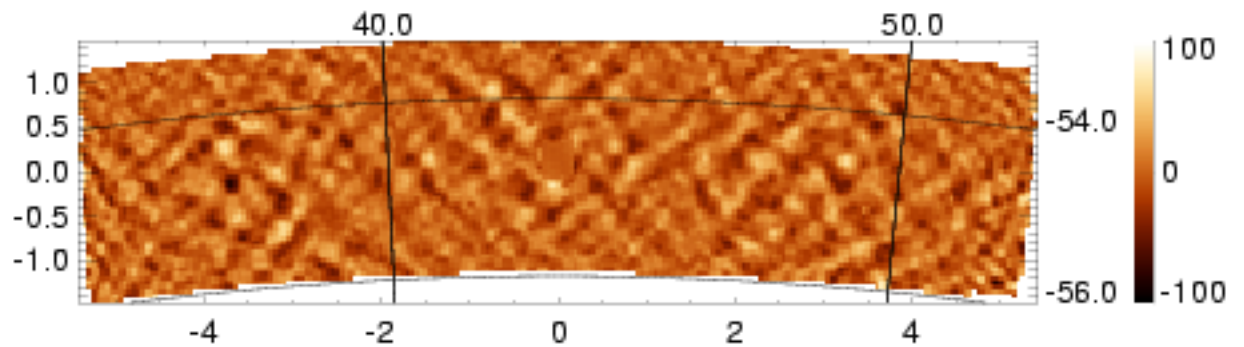
Figure B.2: Map of CMB5. This is the deepest ACBAR field, observed in 2002, 2004, and 2005.
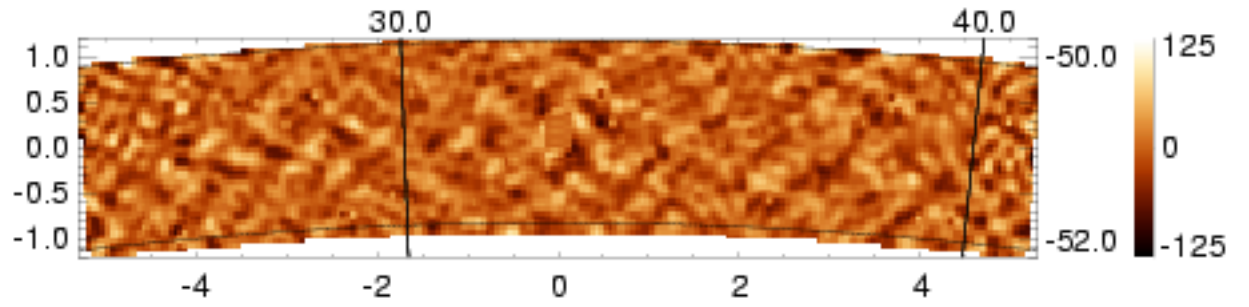
Figure B.3: Map of CMB6, observed in 2002.
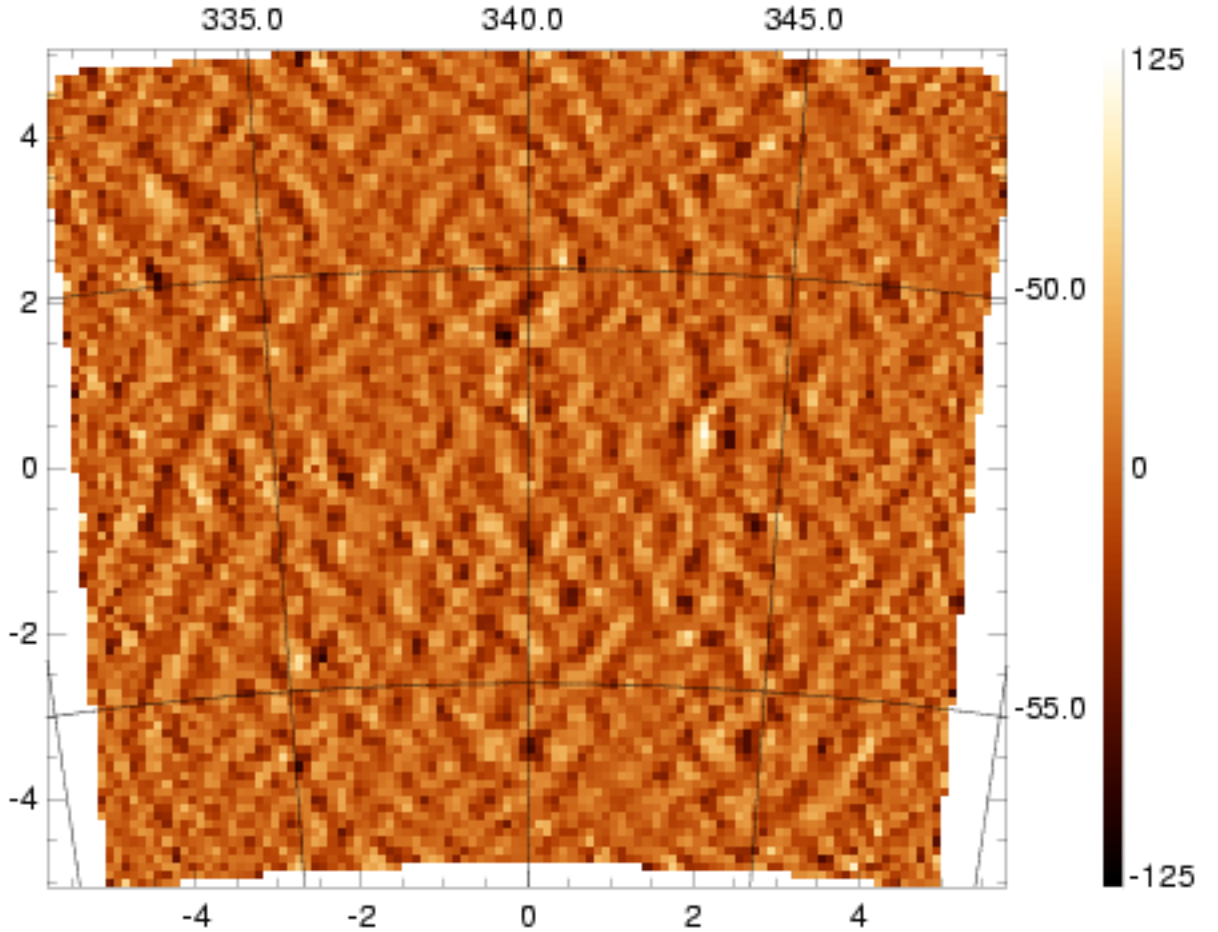
Figure B.4: A combined map of CMB7 observed in 2002 and CMB7ext observed in 2005. CMB7ext was used for the calibration to WMAP3.
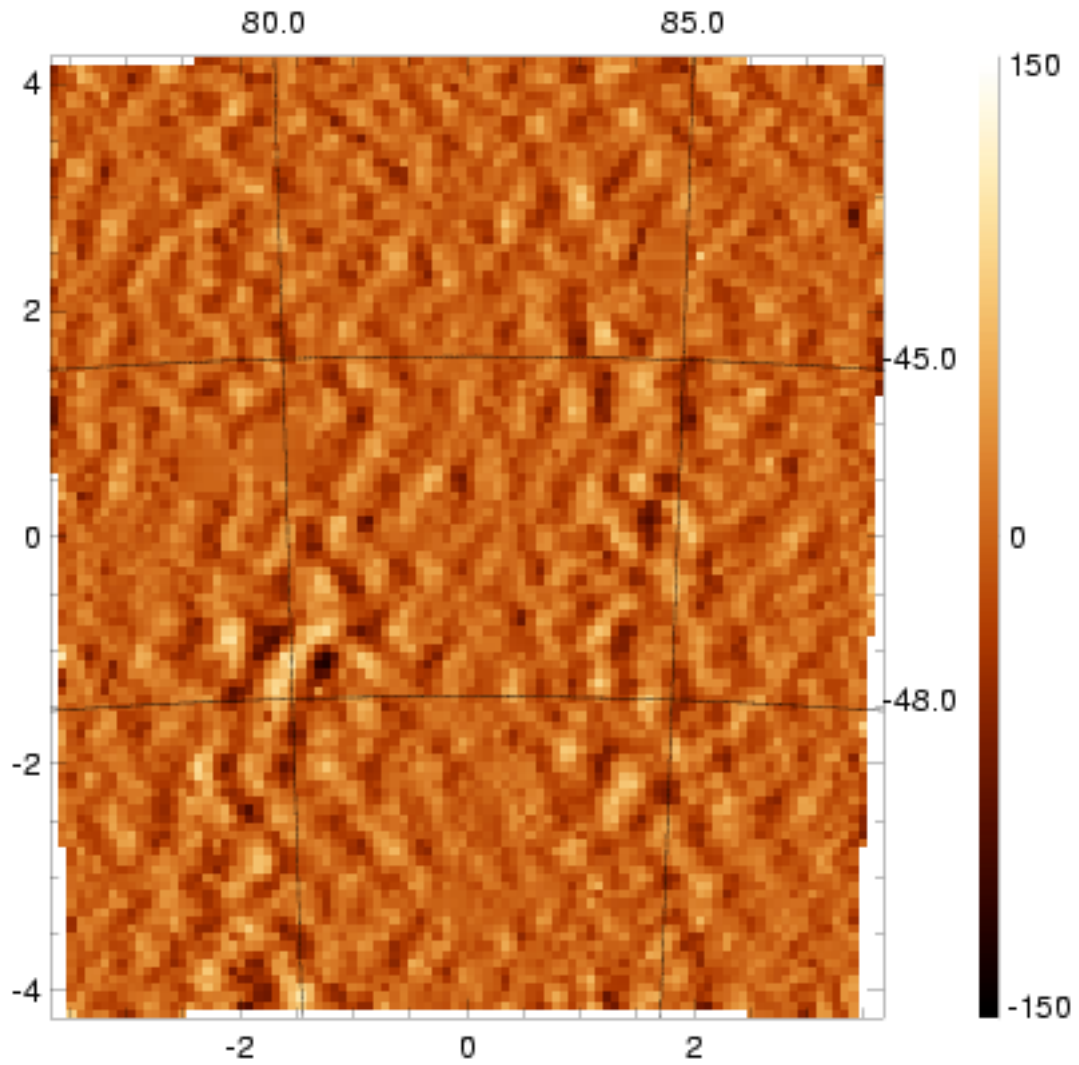
Figure B.5: Map of CMB8 observed in 2004 and 2005. This field was targeted at the deep portion of the B03 map as a possible calibration route. It is the second deepest ACBAR field.
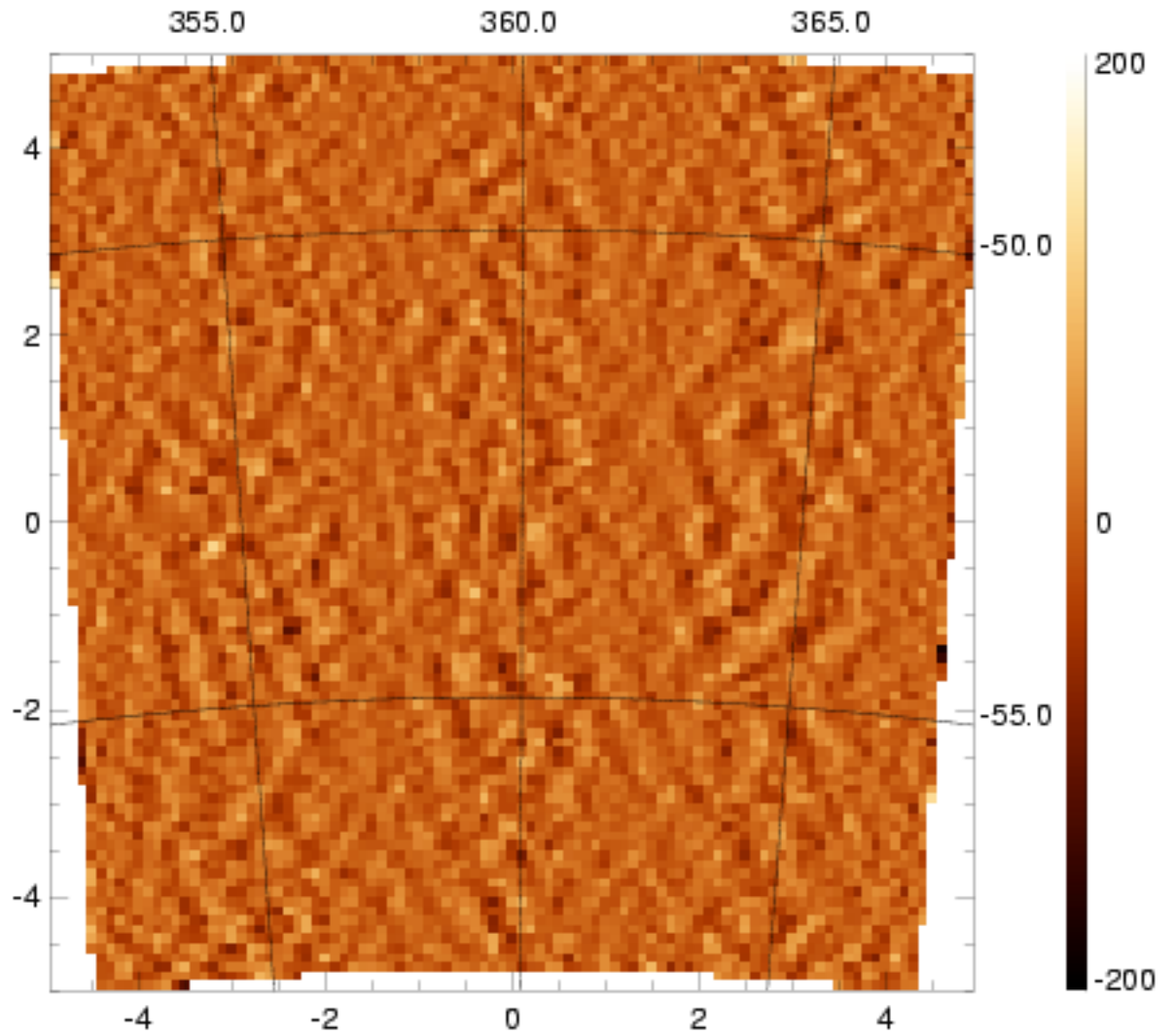
Figure B.6: Map of CMB9, observed in 2005. CMB9 was one of the six, large fields used for the calibration to WMAP3.
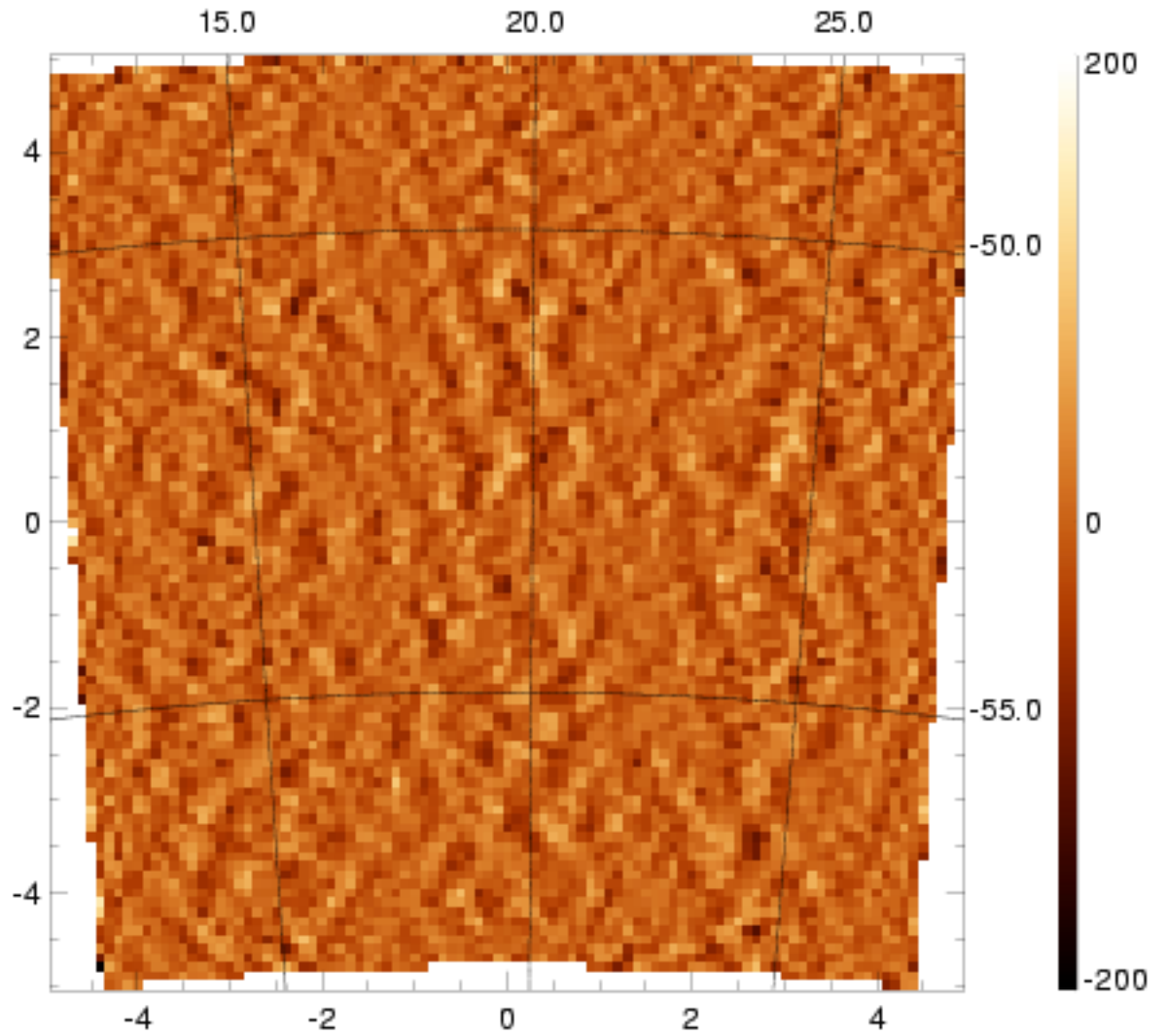
Figure B.7: Map of CMB10, observed in 2005. CMB10 was one of the six, large fields used for the calibration to WMAP3.
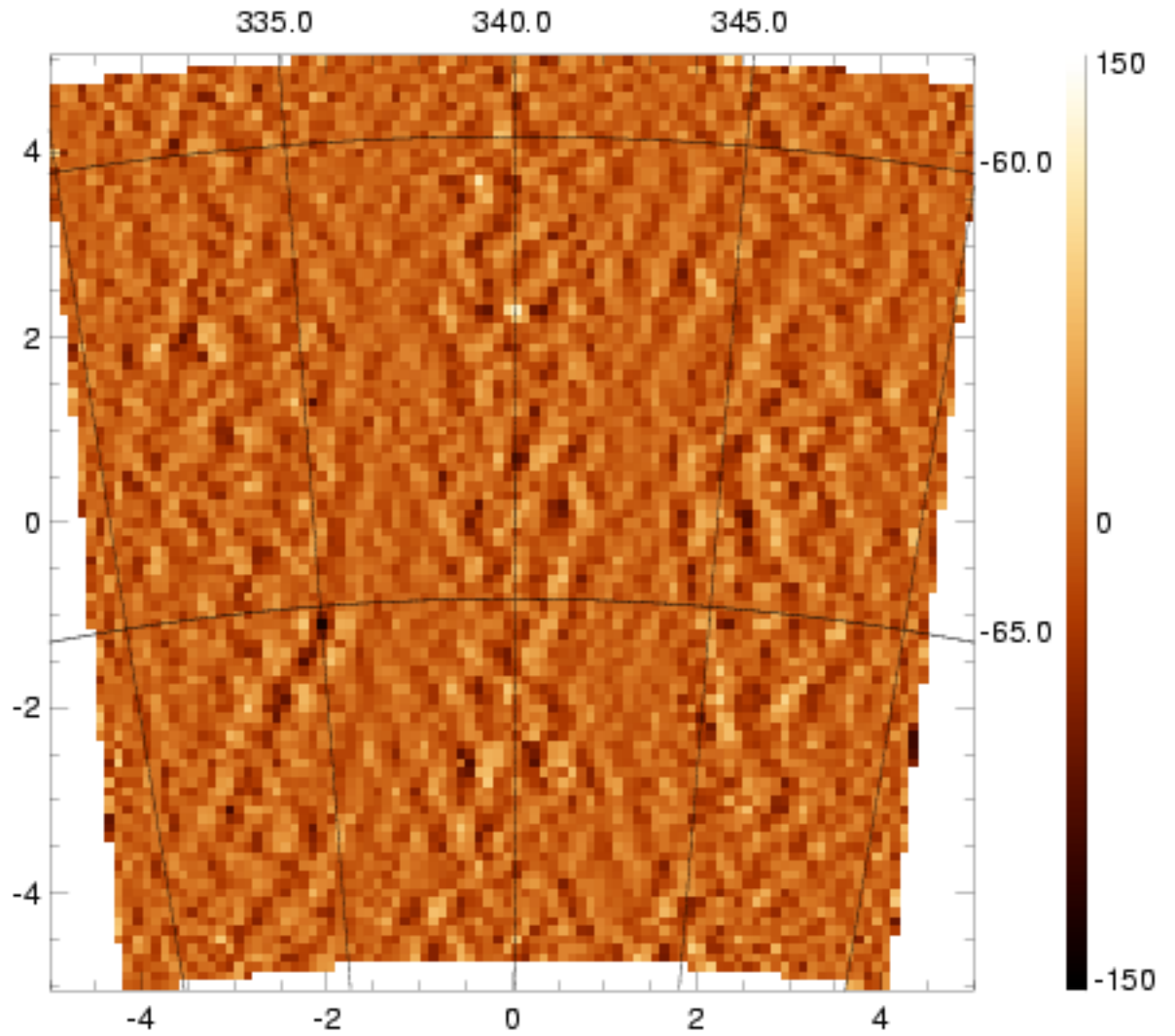
Figure B.8: Map of CMB11, observed in 2005. CMB11 was one of the six, large fields used for the calibration to WMAP3.
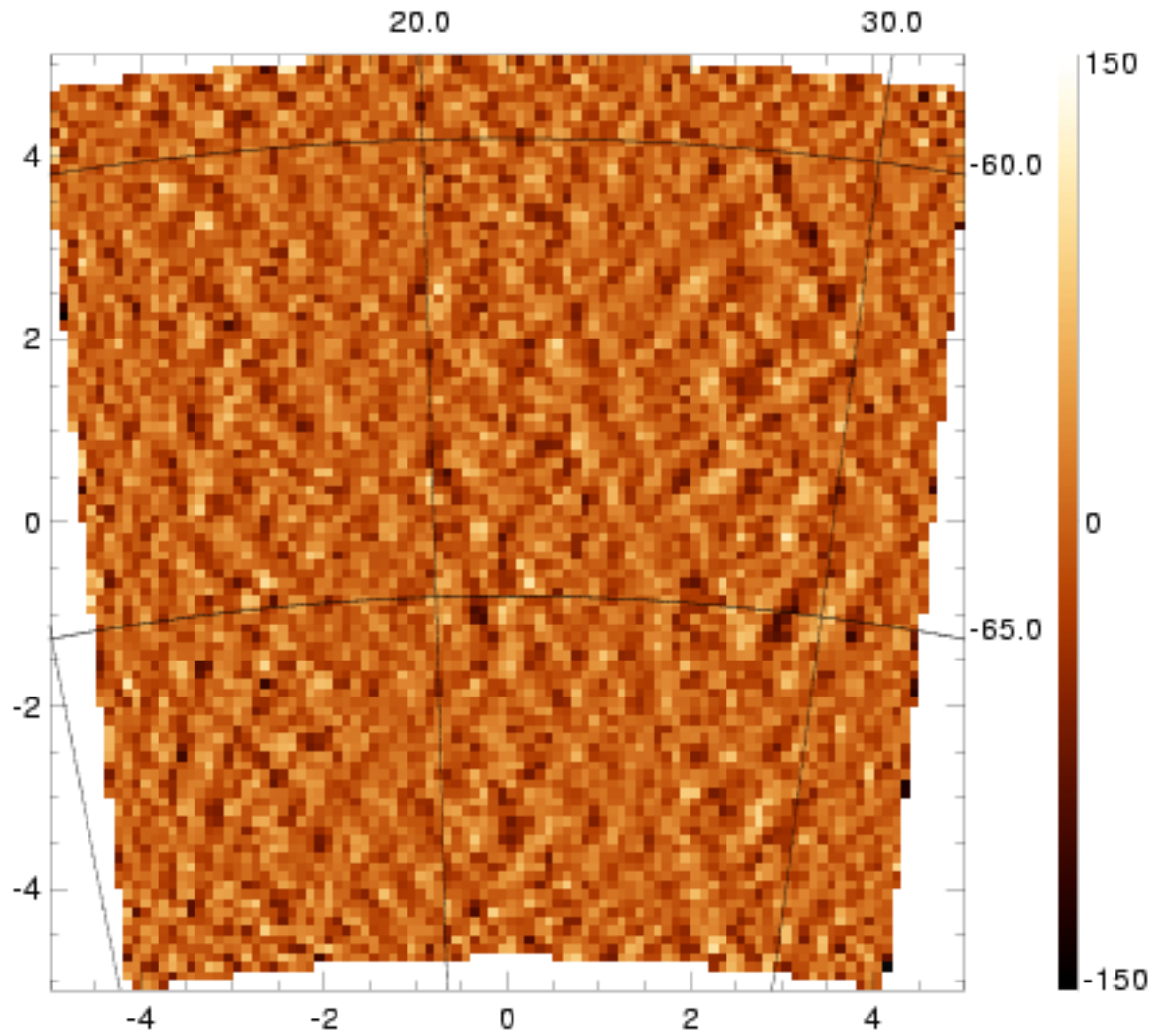
Figure B.9: Map of CMB12, observed in 2005. CMB12 was one of the six, large fields used for the calibration to WMAP3.
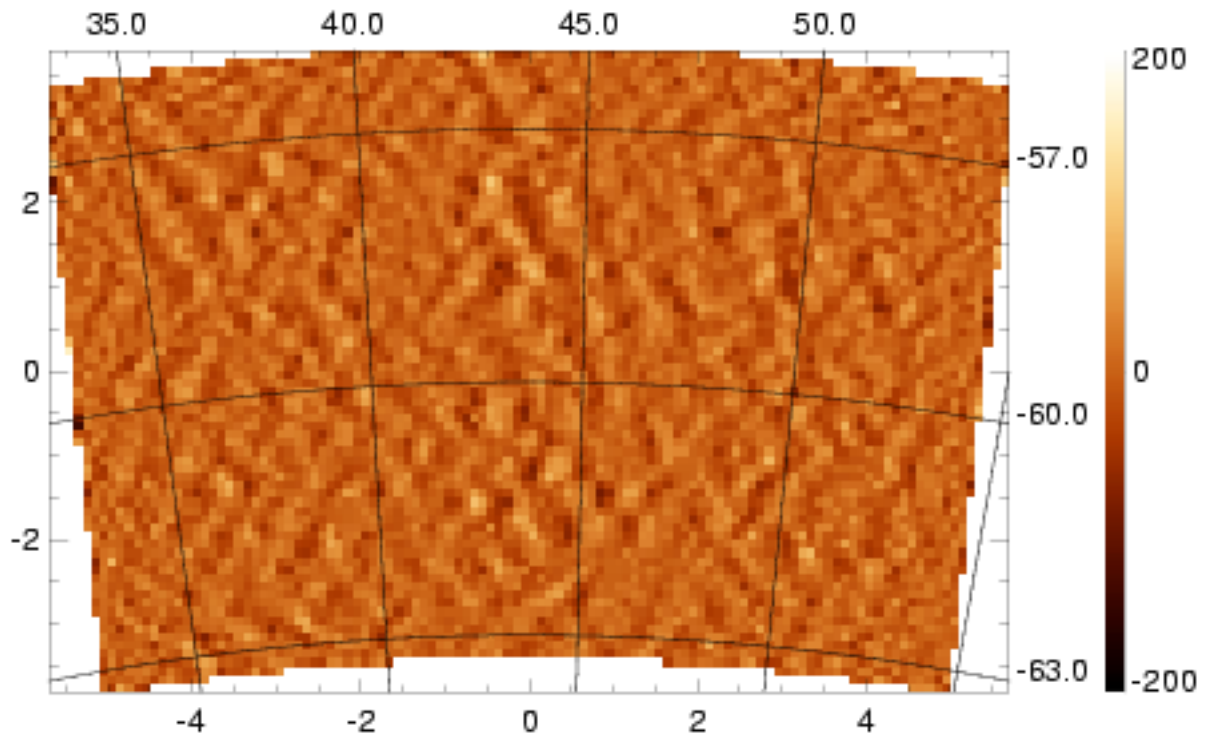
Figure B.10: Map of CMB13, observed in 2005. CMB13 was one of the six, large fields used for the calibration to WMAP3.